Electromagnetic wave propagation in gradient index metamaterials, plasmonic systems and optical fiber networks

Ph.D. Thesis
of
Marios Mattheakis

Advisor: Prof. Giorgos Tsironis
University of Crete
Physics Department

2014

Dedicated to Eleftheria
for her support and
inspiration...

It's worth it, my friend, to
live for a dream
even if its fire is going to
burn you...

UNIVERSITY OF CRETE

DEPARTMENT OF PHYSICS

Ph.D. THESIS

Doctor of Philosophy

by

Marios Mattheakis

COMMITTEE MEMBERS

Prof.	Giorgos Tsironis	-	University of Crete (supervisor)
Prof.	Stelios Tzortzakis	-	University of Crete
Prof.	Maria Kafesaki	-	University of Crete
Prof.	Xenofon Zotos	-	University of Crete
Prof.	Ilias Perakis	-	University of Crete
Prof.	Ioannis Kominis	-	University of Crete
Prof.	Eleftherios Iliopoulos	-	University of Crete

Date of presentation:
31/10/2014

Acknowledgements

I would like to deeply thank my supervisor and mentor Prof. Giorgos Tsironis for his guidance and support during my graduate studies years. I would also like to thank Prof. S. Tzortzakis for his collaboration and inspiring talks as well as Dr. J. Metzger and Dr. R. Fleischmann for their collaboration and knowledge obtained through our interaction. I am also grateful to Dr. Giorgos Neofotistos for his help in the preparation of the thesis and for helpful discussions. I am also indebted to the members of the Crete Center for the Quantum Complexity and Nanotechnology, namely Dr. N. Lazarides, Dr. T. Oikonomou and Dr. P. Navez for many helpful discussions. I would also like to thank my companion in life Eleftheria Koliaraki as well as my family for their support and inspiration.

This work was funded partially by the THALES projects "ANEMOS" and "MACOMSYS" (co-financed by the European Union and Greek National Funds). I also acknowledge partial support through the EC's project FP7-REGPOT-2012-2013-1 under grant agreement 316165.

Abstract

Metamaterials constitute a relatively new field which is very promising because it exhibits properties that may not be readily found in nature. One of promising lines of research is the study of novel characteristics of the propagation of electromagnetic (EM) waves in gradient refractive index (GRIN) lenses. In this Thesis, three geometrical optics methods as well as a wave numerical method have been developed for the investigation of EM waves propagation through media with certain refractive indices. Furthermore, we study the propagation of EM waves through specific geometrical configurations as well as through complex random networks of GRIN lenses, such as Luneburg (LL) and Luneburg Hole (LH) lenses. We show that waveguides, which are formed by LLs, offer the capability of better controlling the propagation characteristics of EM waves. In addition, we show that branched flows and extreme events can arise in such complex photonic systems.

In addition to GRIN lenses networks, we use the discrete nonlinear Schrödinger equation to investigate the propagation of an EM wavepacket through certain configurations of optical fiber lattices and investigate the effects of randomness and nonlinearity in the diffusion exponent.

Finally, we study surface plasmon polaritons (SPPs). We investigate how the presence of active (gain) dielectrics change the dispersion relation and enhance the propagation length of SPPs. We show that the use of an active dielectric with gain, which compensates for metal absorption losses, enhances substantially the plasmon propagation.

Περίληψη

Τα μεταϋλικά αποτελούν ένα σχετικά νέο πεδίο έρευνας το οποίο είναι πολλά υποσχόμενο καθώς παρουσιάζει ιδιότητες οι οποίες δεν έχουν βρεθεί έως τώρα στη φύση. Μία από τις σημαντικε΄ς κατευθύνσεις ερευνητικής δραστηριότητας στο πεδίο αυτό είναι η μελέτη καινοτόμων χαρακτηριστικών στη διάδοση ηλεκτρομαγνητικών (ΗΜ) κυμάτων σε φακούς με μεταβαλλόμενο δείκτη διάθλασης. Στη Διατριβή αυτή, τρεις μέθοδοι γεωμετρικής οπτικής και μία κυματική μέθοδος έχουν αναπτυχθεί για τη διερεύνηση της διάδοσης ΗΜ κυμάτων μέσα από υλικά συγκεκριμένων δεικτών διάθλασης. Επιπλέον μελετάται η διάδοση ΗΜ κυμάτων μέσα από οργανωμένες δομές καθώς και μέσα από τυχαία δίκτυα φακών μεταβαλλόμενου δείκτη διάθλασης, όπως οι φακοί και οι οπές Luneburg. Δείχνουμε ότι κυματοδηγοί, οι οποίοι αποτελούνται από φακούς Luneburg, προσφέρουν τη δυνατότητα καλύτερου ελέγχου στη διάδοση των ΗΜ κυμάτων. Επίσης δείχνουμε ότι διακλαδισμένη διάδοση καθώς και ακραία φαινόμενα μπορούν να αναδειχθούν σε τέτοια πολύπλοκα φωτονικά δίκτυα.

Επί πρόσθετα, χρησιμοποιούμε την διακριτή μη γραμμική εξίσωση Schrödinger για να διερευνήσουμε τη διάδοση ενός ΗΜ κυματοπακέτου μέσα από δομές οπτικών ινών και μελετάμε πως επηρεάζουν η τυχαιότητα και η μη γραμμικότητα τον εκθέτη διάχυσης.

Τέλος, μελετάμε τα επιφανειακά πλασμόνια. Διερευνούμε πως η παρουσία ενός ενεργού διηλεκτρικού αλλάζει την σχέση διασποράς και βελτιώνει το μήκος διάδοσης των πλασμονίων. Δείχνουμε ότι η χρήση ενός ενεργού διηλεκτρικού, το οποίο αντισταθμίζει τις ωμικές απώλειες του μετάλλου, βελτιώνει σημαντικά την διάδοση των πλασμονίων.

Contents

Introduction

Since the beginning of science (or *Natural Philosophy*) the understanding of the nature of light -as well as the manipulation of it- has attracted the attention of scientists. The ancient Greeks believed that light -as well as heat- was composed of minute atoms and they studied the motion of light in geometrical terms. Furthermore, ancient Greeks exhibited the first successful attempts to manipulate the light propagation; a historic example is the use of the famous mirrors of Archimedes, which were used for burning the enemy's ships. Newton also believed in atomic theory and he wrote, at the beginning of the 18^{th} century, his classical opus *"Optics"*, in which he presented his theory about the particle nature of light. In the same century, Huygens conducted many experiments concluding that light behaves as a wave instead of a bunch of particles. His beliefs were adopted by Young in the 19^{th} century who also conducted many experiments for studying light interference and thus, proving the wave nature of light. The 19^{th} century was one of the most important periods for the understanding of the nature of light; Fresnel showed that light is a transverse wave; Maxwell derived his famous equations and showed that the light comprises a new kind of wave, namely the *Electromegnetic wave* (EM). This idea was proved experimentally and was applied by Hertz some years later by constructing instruments to transmit and receive radio pulses. In the beginning of the 20^{th} century Einstein reintroduced the particle properties of light in explaining the *photoelectric effect*, revealing that scientists had not fully understood yet the real nature of light. The idea of the "double" nature of light, that is that light is both wave and particle, born by the photoelectric effect, planted the seeds for the quantum mechanics revolution resulting in a more complete understanding of the nature of light and offering opportunities for manipulation of it.

Nowadays another breakthrough has been started regarding the manipulation of light. A new kind of materials, called *Metamaterials* (MMs), which can fabricated readily in labs, give us much more control toward light manipulation. MMs are artificial materials engineered to have properties not

found in nature, such as negative refractive index, cloaking, perfect imaging, flat slab imaging and gradient refractive index (GRIN) lenses. MMs are engineered by means of the composition of one or several different materials on subwavelength structures. The macroscopic properties of MMs are derived by means of the microscopic properties of the compositional properties as well as from certain structures of the compositional materials.

In this Thesis, GRIN metamaterials are investigated and studied. GRIN metamaterials are formed via the spatial variation of the index of refraction and lead to enhanced light manipulation in a variety of circumstances. These metamaterials provide means for constructing various types of waveguides and other optical configurations that guide and focus light in specific desired paths. Different configurations have been tested experimentally while the typical theoretical approach uses transformation optics (TO) methods to cast the original inhomogeneous index problem to an equivalent one in a deformed space. While this approach is mathematically elegant, it occasionally hides the intuition obtained through more direct means.

For the most part of this Thesis we are dealing with GRIN lenses. At first we develop three geometrical optics methods, which provide ray-tracing solutions for the description of light paths. We apply the geometric optics methods on a well known GRIN lens system, namely the *Luneburg Lens* (LL) and calculate analytically one dimension (1D) and two dimensions (2D) ray tracing solutions for the light propagation through an LL. We also develop a numerical wave method, the *Finite Difference Time Domain* (FDTD), and compare the findings obtained by geometrical optics methods to those obtained by the FDTD method.

Having developed the mathematical tools for the study of EM waves propagation through GRIN lenses, we proceed with the investigation of light propagation through networks of GRIN lenses. First, we make certain configurations of LLs showing that EM waveguides can be formed by such GRIN lenses. Light propagation through random networks is also investigated; as a result we show that extreme events, such as branched flows and rogue waves, can arise in such complex photonic GRIN systems.

In addition to GRIN lenses, we have investigated light propagation through disordered optical coupled fiber lattices. We have developed a simple model, based on the *Discrete Nonlinear Schrödinger Equation* (DNLS), for the study of EM wavepacket propagation, investigating how the fiber network topology (namely, the randomness of the arrangement of fibers), influences the diffusion exponent of light propagation. Furthermore, we study how this diffusion exponent is affected by the presence of nonlinearity (Kerr effect).

Finally, we investigate a well known light-matter interaction effect, called the *Surface Plasmon Polaritons* (SPPs). SPPs are quasi particles which are

created by the coupling of EM waves with the electron oscillations field. We develop and discuss the background theory of SPPs based on Maxwell equations and we describe a method for SPPs excitation based on the *attenuated total reflectance* (ATR) method. We introduce active (or gain) dielectrics and study how these active materials affect the properties of SPPs such as the SPPs dispersion relation and the propagation length.

Chapter 1

Methods for light propagation

In the beginning of this Thesis, fundamental concepts and methods which will be used throughout in this Thesis will be introduced. We begin by describing methods that have been used in order to determine the characteristics of light propagation via an inhomogeneous isotropic medium with refractive index $n(r) = \sqrt{\varepsilon}$, where r is the radial coordinate of a given structure embedded in the medium. In the first part of this Thesis we focus our investigation on the electromagnetic field associated with propagation near the visible spectrum; in this regime, light oscillates very rapidly (with frequencies of the order of $10^{14} Hz$) resulting in very large magnitudes of the wavevector (i.e. $k \to \infty$) and very small magnitudes of wavelength ($\lambda \to 0$). In this limit, the wave behavior of the light can be neglected and the optical laws can be formulated in geometrical terms, that is, the electromagnetic (EM) waves are treated as rays. This approximation is well known in the literature as geometrical optics and holds as the size of lenses (or obstacles), in the propagation media, are much larger than the wavelength of the propagated EM wave. The geometrical optics is a very convenient method, compared with wave optics, because so the analytical as the numerical calculation are much easier and faster than those in the wave optics. On the other hand, the main advantage of wave optics is that it holds for any case of light propagation whereas for the geometrical optics the wavelength has to be much more smaller than the characteristics length of the geometry of the propagation media [1–5].

In this Chapter, three methods of geometrical optics propagation together with a numerical wave optics method are developed and applied in a specific medium comprised by Luneburg Lens (LL) [4, 6], which is used as a toy model. The LL belongs to the gradient refractive index (GRIN) lenses and it is a spherical construction where the index of refraction varies from the value 1, at its outer boundary, to $\sqrt{2}$ in its center through a specific functional

dependence on lens radius, as it is described by the equation (1.1)

$$n(r) = \sqrt{2 - \left(\frac{r}{R}\right)^2} \tag{1.1}$$

where R is the radius of the LL. Its basic property, in the geometrical optics limit, is to focus parallel rays that impinge on the spherical surface on the opposite side of the lens. This feature makes LLs quite interesting for applications since the focal surface is predefined for parallel rays of any initial angle. The LLs can be used to form GRIN optical metamaterials (MMs); the latter use spatial variation of the index of refraction and lead to enhanced light manipulation in a variety of circumstances [6].

In this Chapter, we develop and apply the following three geometrical optics methods: (a) Fermat's principle of the optical path optimization deriving to an exact ray tracing equation for a single LL (detailed presentation in subsection 1.1); this is a quasi two dimensional (2D) approximation, (b) a parametric two dimensional method based also on Fermat's principle, where the infinitesimal arc length is used as a free parameter (subsection 1.2), and (c) a geometrical optics approach based on the Helmholtz wave equation (subsection 1.3). Finally, (in subsection 1.4) a numerical method for solving time-dependent Maxwell equation, known as Finite Difference in Time Domain (FDTD), is presented, and the obtained results are compared with the ray-tracing findings.

1.1 Quasi two dimensional (2D) ray tracing

The total time $\mathcal{T}$ that light takes to traverse a path between points A and B is given by the integral [1, 5]

$$\mathcal{T} = \int_A^B dt = \frac{1}{c}\int_A^B n ds \tag{1.2}$$

where the infinitesimal time dt has been written in arc length terms as $dt = ds/v$ and v is the velocity of light in a medium with refractive index n ($v = c/n$), where c the velocity of light in the bulk medium.

The optical path length $\mathcal{S}$ of a ray transversing from a point A to a point B via a medium with radially depended refractive index $n(r)$ is related to the travel time by $\mathcal{S} = c\mathcal{T}$ and is given by [1–6]

$$\mathcal{S} = \int_A^B n(r) ds \tag{1.3}$$

Since the optical path length $\mathcal{S}$ is independent of the time, it is a purely geometrical quantity. According now the variational theory and the Fermat's statement, the light follows the path where it needs the minimum time travel, viz. an extremum in the travel time $\mathcal{T}$ of equation (1.2), as a result the optical length of the path followed by light between two fixed points, A and B, is also an extremum of equation (1.3), subsequently, in the context of calculus of variations, this can be written as

$$\delta\mathcal{S} = \delta \int_A^B n(r)ds = 0 \tag{1.4}$$

For historical reasons we note that the two integral equations (1.2) and (1.3) is proposed by the famous French mathematician Pierre de Fermat, however, the complete modern statement of the variational Fermat principle was developed after the generation of the variational theory.

In polar coordinates the arc length is $ds = \sqrt{dr^2 + r^2 d\phi^2}$, where r, ϕ are the radial and angular polar coordinates respectively. In the quasi 2D approximation the coordinate r can be considered as the independent variable of the problem or as the generalized time and therefore the arc length can be written as $ds = \sqrt{1 + r^2\dot{\phi}^2}dr$, with $\dot{\phi} \equiv d\phi/dr$. As a result, the Fermat's variational integral of equations (1.3) and (1.4) becomes

$$S = \int_A^B n(r)\sqrt{1 + r^2\dot{\phi}^2}dr \tag{1.5}$$

yielding the optical Lagrangian [3–6]

$$\mathcal{L}(\phi, \dot{\phi}, r) = n(r)\sqrt{1 + r^2\dot{\phi}^2} \tag{1.6}$$

Since we know the Lagrangian of the problem (equation (1.6)), we can calculate the optical Hamiltonian by using Legendre transformation [7, 8]. Afterwards, we can proceed by solving Hamilton equations yielding to a ray tracing solution. However, in this part of Thesis, we are working with Lagrange formalism instead of Hamiltonian, in the Appendix A there are the calculations for the Hamiltonian derivation as well as for the ray tracing solution.

The shortest optical path is obtained via the minimization of the integral of equation (1.5) and can be calculated by solving the Euler-Lagrange equations for the Lagrangian of equation (1.6), viz.

$$\frac{d}{dr}\frac{\partial\mathcal{L}}{\partial\dot{\phi}} = \frac{\partial\mathcal{L}}{\partial\phi} \tag{1.7}$$

Since the Lagrangian of equation (1.6) is cyclic in ϕ, $\partial L/\partial\phi = 0$ and, thus, $\partial\mathcal{L}/\partial\dot{\phi} = C$ where C is a constant, the Lagrangian of equation (1.6) [3, 5, 6] therefore becomes

$$\frac{n(r)r^2}{\sqrt{1+r^2\dot{\phi}^2}}\dot{\phi} = C \tag{1.8}$$

This is a nonlinear differential equation describing the trajectory $r(\phi)$ of a ray in an isotropic medium with refractive index $n(r)$. Replacing the term $\dot{\phi} \equiv d\phi/dr$ and solving for $d\phi$, we obtain a first integral of motion [1, 3, 6], that is

$$\int d\phi = \int \frac{C}{r\sqrt{n^2r^2 - C^2}}dr \tag{1.9}$$

The equation (1.9) holds for arbitrary index of refraction $n(r)$. The differential equation (1.8) and the integral (1.9) are the most important results of this Section; they provide, for a specific refractive index profile, the ray tracing equation for $r(\phi)$.

We have done so for the specific LL refractive index function of equation (1.1), obtaining the ray tracing equation in the interior of a single LL

$$r(\phi) = \frac{C'R}{\sqrt{1 - \sqrt{1-C'^2}\ \sin\left(2(\phi+\beta)\right)}} \tag{1.10}$$

where C' and β are constants [6]. This analytical expression may be cast in a direct Cartesian form for the (x, y) coordinates of the ray; after some algebra we obtain

$$\left(1 - T\sin(2\beta)\right)x^2 + \left(1 + T\sin(2\beta)\right)y^2 - 2T\cos(2\beta)xy + \left(T^2 - 1\right)R^2 = 0 \tag{1.11}$$

where T and β are constants. We note that equation (1.11) is the equation of an ellipse. This result agrees with the Luneburg theory and states that inside a LL light follows elliptic orbits [4, 6].

The constants T and β of equation (1.11) are determined by the ray boundary (or the "initial" conditions) and depend on the initial propagation angle θ of a ray that enters the lens at the point (x_0, y_0) located on the circle at the lens radius R [3, 6]. In the most general case, the entry point of the ray is at $(x, y) = -R(\cos\theta, \sin\theta)$. Substituting these expressions in equation (1.11) we obtain after some algebra the relation

$$T = \sin\left(2\beta + 2\theta\right) \tag{1.12}$$

In order to determine the constants T and β, we need an additional relation connecting them. We take the derivative of the equation (1.11) with respect

to x and utilize the relation $dy/dx = \tan(\theta)$, where θ the initial propagation angle. In addition, using (x_0, y_0) for the initial ray point on the LL surface, we set $x = x_0$ and $y = y_0$ in equation (1.11) and solve for T, getting

$$T = \frac{x_0 + y_0 \tan(\theta)}{\tan(\theta)\left[x_0 \cos(2\beta) - y_0 \sin(2\beta)\right] + \left[x_0 \sin(2\beta) + y_0 \cos(2\beta)\right]} \tag{1.13}$$

The equations (1.12) and (1.13) comprise an algebraic nonlinear system expressing the constants T and β as a function of the initial ray entry point in the LL at (x_0, y_0) with initial propagation angle θ. Combining equations (1.12) and (1.13) we obtain

$$\beta = \frac{1}{2}\left(\tan^{-1}(x_0/y_0) - \theta\right) \tag{1.14}$$

therefore, according to the equation (1.12)

$$T = \sin\left(\tan^{-1}(x_0/y_0) + \theta\right) \tag{1.15}$$

Substituting now the equations (1.14) and (1.15) to the equation (1.11) and solving for y, we obtain the ray tracing equation for an LL [6], that is

$$\begin{aligned} y(x) = & \frac{(2x_0y_0 + R^2\sin(2\theta))}{2x_0^2 + (1+\cos(2\theta))\,R^2}\; x \\ & + \frac{\sqrt{2}Ry_0\cos(\theta)\sqrt{(1+\cos(2\theta))\,R^2 + 2x_0^2 - 2x^2}}{2x_0^2 + (1+\cos(2\theta))\,R^2} \\ & - \frac{x_0\sin(\theta)\sqrt{(1+\cos(2\theta))\,R^2 + 2x_0^2 - 2x^2}}{2x_0^2 + (1+\cos(2\theta))\,R^2} \end{aligned} \tag{1.16}$$

The equation (1.16) describes the complete solution of the ray trajectory through an LL. In the simple case where all the rays are parallel to the x axis and thus the initial angle is $\theta = 0$, the equation (1.16) simplifies to the equation [6]

$$y(x) = \frac{y_0}{x_0^2 + R^2}\left(x_0 x + R\sqrt{R^2 + x_0^2 - x^2}\right) \tag{1.17}$$

We note that in order to determine the exit angle θ', i.e. the angle with which each ray exits the lens, we take the arc tangent of the derivative of equation (1.16) with respect to x, at the focal point on the surface of lens, i.e. at $x = R\cos(\theta)$. The solution of equation (1.16) can be used to study several configurations of LLs; this topic will be discussed later in Chapter 2.

We present, in Fig.1.1, the ray tracing propagation based on the equation (1.16), through a single LL for initial propagation angle $\theta = 0$ (Fig.1.1a)

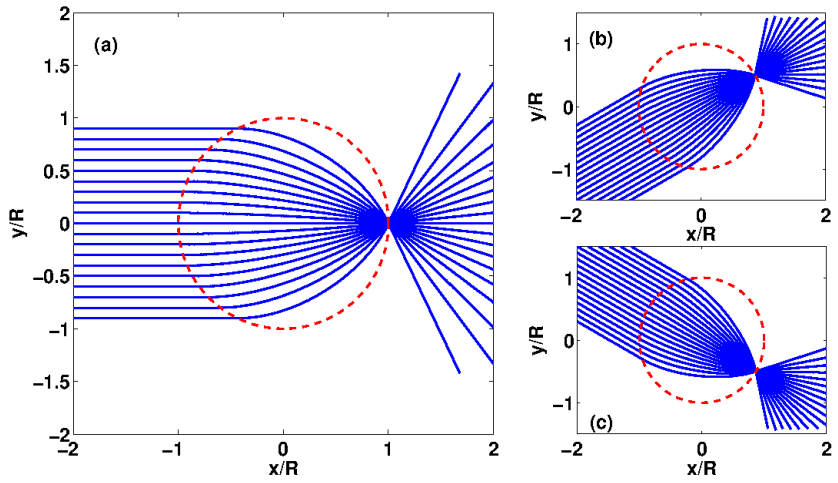

Figure 1.1: The red dashed lines denote the the Luneburg lenses (LL) whereas the blue lines represent light rays. Ray tracing through a single LL for initial propagation angle (a) $\theta = 0$ (b) $\theta = \pi/6$ (c) $\theta = -\pi/6$; all rays are focused on a single point on the opposite side that they entered in the LL.

and for $\theta = \pm\pi/6$ (Fig.1.1(b - c)) [6]; in all cases the bulk media is air with refraction index $n_{air} = 1$.

When the rays are scattered backwards, i.e. the propagation angle $|\theta_p| > \pi/2$, the quasi 2D approximation breaks down and the equation (1.16) gives complex solutions. This failure is due to the assumption that the radial coordinate plays the role of time, viz. a monotonically increasing parameter similar to the physical time; in the Fig.1.2 this failure in ray-tracing is demonstrated. In these cases it is more practical to use parametric solutions where the ray coordinates x, y are both dependent variables. This approach is explained in Sections 1.2 and 1.3 where the parametric solution is derived.

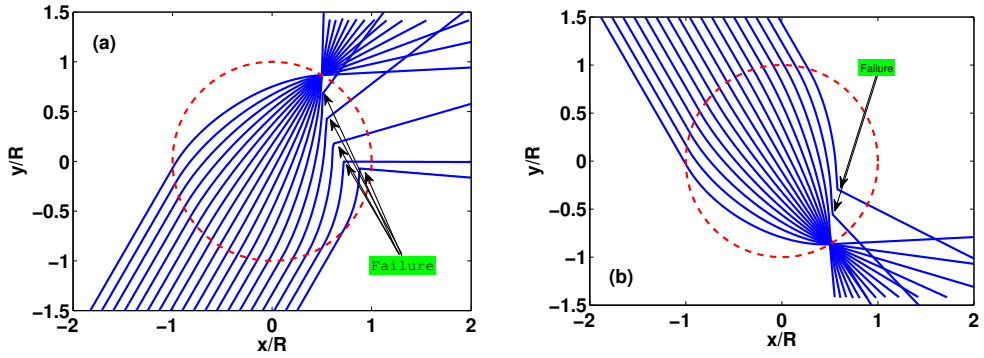

Figure 1.2: The red dashed lines denote the the Luneburg lenses (LL) whereas the blue lines represent light rays. In both pictures the black arrows indicate the failure of quasi 2D approximation, viz. when the rays are scattered backwards, that is, the propagation angle $|\theta_p| > \pi/2$. Ray tracing through a single LL is plotted for initial propagation angles (a) $\theta = \pi/3$ and (b) $\theta = -\pi/3$.

1.2 Parametric two dimensional (2D) ray tracing

Since the quasi 2D approximation fails for backscattered rays, we need to develop a real two dimensional parametric ray tracing equation. This is done by using Fermat's principle and assuming that both ray coordinates are dependent variables.

We use the infinitesimal arc length $ds = \sqrt{dx^2 + dy^2}$ in Cartesian coordinates and further introduce the parameter τ as generalized time i.e. $ds = \sqrt{\dot{x}^2 + \dot{y}^2}\, d\tau$, where the dot indicates differentiation with respect to parameter τ, ($\dot{\alpha} \equiv d\alpha/d\tau$) and $x \equiv x(\tau)$, $y \equiv y(\tau)$ [2, 4–6]. The Fermat integral of equation (1.3) becomes

$$\mathcal{S} = \int_A^B n(x,y)\sqrt{\dot{x}^2 + \dot{y}^2} d\tau \tag{1.18}$$

where $n(x, y)$ is the refractive index in Cartesian coordinates; Minimization of the travel path $\mathcal{S}$ leads to the optical Lagrangian

$$\mathcal{L}(x, y, \dot{x}, \dot{y}, \tau) = n(x, y)\sqrt{\dot{x}^2 + \dot{y}^2} \tag{1.19}$$

In this method we are going to work with Hamilton formalism, therefore we introduce the generalized optical momenta k_x, k_y that are conjugate to x, y as

$$k_x = \frac{\partial \mathcal{L}}{\partial \dot{x}} = \frac{n\dot{x}}{\sqrt{\dot{x}^2 + \dot{y}^2}} \tag{1.20}$$

$$k_y = \frac{\partial \mathcal{L}}{\partial \dot{y}} = \frac{n\dot{y}}{\sqrt{\dot{x}^2 + \dot{y}^2}} \tag{1.21}$$

The equations (1.20) and (1.21) comprise of an algebraic nonlinear system, which has the solution

$$k_x^2 + k_y^2 - n(x, y)^2 = 0 \tag{1.22}$$

We can rewrite the equation (1.22) in vector form using $\vec{r} \equiv (x, y)$ and $\vec{k} \equiv (k_x, k_y)$, that is

$$\vec{k}^2 - n(\vec{r})^2 = 0 \tag{1.23}$$

Multiplying equation (1.23) with the factor $1/2$ reveals the direct analogy to the equations of classical mechanics. The first term is the kinetic energy of the rays

$$T = \frac{\vec{k}^2}{2} \tag{1.24}$$

whereas, the second term is the potential energy given by

$$V = -\frac{n(\vec{r})^2}{2} \tag{1.25}$$

while the total energy is

$$\mathcal{H}(\vec{r}, \vec{k}) = \frac{\vec{k}^2}{2} - \frac{n(\vec{r})^2}{2} \tag{1.26}$$

which is equal to zero $\mathcal{H} = 0$ regarding the equation (1.23). The equations (1.24)-(1.26) can be interpreted as representing the motion of a classical particle, of unit mass, moving in a potential, while the total energy of the system is zero [1, 2, 4, 6].

We can obtain a Hamiltonian ray tracing system by solving Hamilton's equations for the Hamiltonian of equation (1.26) [5, 6, 9]; we get

$$\frac{d\vec{r}}{d\tau} = \frac{\partial \mathcal{H}}{\partial \vec{k}} = \vec{k} \tag{1.27}$$

and

$$\frac{d\vec{k}}{d\tau} = -\frac{\partial \mathcal{H}}{\partial \vec{r}} = \frac{1}{2}\nabla n(\vec{r})^2 \tag{1.28}$$

where $\nabla \equiv \left(\frac{\partial}{\partial x}, \frac{\partial}{\partial y}\right)$, τ is an effective time related to real travel time t through $d\tau = c\ dt$, where c is the velocity of rays in the bulk medium with refractive index n_0 ($c = c_0/n_0$). Combining equations (1.27) and (1.28) we obtain the differential equation (1.29) [1, 2, 4–6, 9]

$$\ddot{\vec{r}} = \frac{1}{2}\nabla n(\vec{r})^2 \tag{1.29}$$

and restoring the real travel time t instead of the effective time τ, we get

$$\ddot{\vec{r}} = \frac{c^2}{2}\nabla n(\vec{r})^2 \tag{1.30}$$

where derivatives are taken with respect to travel time t, that is, $\dot{q} = dq/dt$ for arbitrary $q(t)$. In conclusion, the equation (1.30) is a general equation of motion for ray paths in a medium with an arbitrary refractive index function $n(\vec{r})$. The explicit solution for Luneburg lens will be given in the following Section (Section 1.3), since the equation (1.30) is also derived with different method.

1.3 Helmholtz wave equation approach

In this Section, we present a geometrical optics approach based on the Helmholtz wave equation. We obtain once again the ray tracing equation (1.28) and find an explicit ray solution for light propagation through an LL with refractive index given by the equation (1.1).

The stationary states for a monochromatic EM wave are given by the solutions of the Helmholtz equation (1.31) [2, 5, 9].

$$\left[\vec{\nabla}^2 + (nk_0)^2\right] u(x, y) = 0 \tag{1.31}$$

where $\nabla^2 = \frac{\partial^2}{\partial x^2} + \frac{\partial^2}{\partial y^2}$ is the Laplacian in two dimensional space and $u(x, y)$ is a scalar function representing any component of the electric or magnetic field; n is the refractive index that generally depends on position ($n \equiv n(\vec{r})$), $k_0 \equiv \omega/c = 2\pi/\lambda_0$ is the wave vector in the bulk media where ω and λ_0 are the angular frequency and wavelength of the EM wave respectively and finally c is the velocity of the light [2, 5, 6, 9]. Although equation (1.31) is time-independent and therefore we cannot investigate dynamical phenomena, we can determine the stationary paths followed by the light rays; this is a ray tracing approximation.

Assuming that the scalar field u can be determined by an amplitude real function $A(x, y)$ and a phase real function $\phi(x, y)$ (Sommerfeld-Runge

assumption), where ϕ is known as the eikonal function [1–5, 9]; we proceed with the well known transformation

$$u(x,y) = A(x,y)e^{i\phi(x,y)} \tag{1.32}$$

Substituting equation (1.32) into wave equation (1.31) and separating the real from the imaginary parts, we obtain the following system of differential equations [6, 9]

$$(\nabla\phi)^2 - (nk_0)^2 = \frac{\nabla^2 A}{A} \tag{1.33}$$

$$\nabla \cdot \left(A^2 \nabla A\right) = 0 \tag{1.34}$$

The equation (1.34) expresses the constancy of the flux of the vector $A^2\nabla\phi$ along any tube formed by the field lines of the wavevector [9], defined through $\vec{k} = \vec{\nabla}\phi$, which transforms the equation (1.33) into

$$\vec{k}^2 - (nk_0)^2 = \frac{\nabla^2 A}{A} \tag{1.35}$$

The last term in the equation (1.33), viz. $\frac{\nabla^2 A}{A}$, is called Helmholtz potential [6, 9]; it preserves the wave behaviour, like diffusion, in the ray tracing equation. In the geometrical optics limit (where the space variation L of the beam amplitude A satisfies the condition $k_0 L >> 1$ i.e. $\lambda << L$) the Helmholtz potential vanishes; in this case the equation (1.35) gives the well known eikonal equation, (equation (1.36)) which is the basic equation in the geometrical optics approach [1–5, 9], namely

$$(\nabla\phi)^2 = (nk_0)^2 \tag{1.36}$$

The most important result of this approach is that the rays are not coupled any more and they propagate independently one from the other, viz. the movement of rays looks like more with particles movement than with wave propagation.

We introduce the optical Hamiltonian by multiplying equation (1.35) with the factor $c/(2k_0)$ and by using the relation (1.36), yielding to

$$\mathcal{H}(\vec{r},\vec{k}) = \frac{c}{2k_0}\vec{k}^2 - \frac{ck_0}{2}n^2(\vec{r}) \tag{1.37}$$

In addition, according the equation (1.35) and the assumption that $\frac{\nabla^2 A}{A} = 0$, the Hamiltonian of equation (1.37) describes the motion of a classical particle in a potential, while the total energy of the system is zero, as the Hamiltonian (1.26) of Section 1.2 represents.

Finally, the system of equation of motion can be written as a second order ordinary differential equation (ODE) by solving the Hamilton's equation described by equations (1.27),(1.28) and yields to the same equation of motion which is found earlier and given by the equation (1.30), viz. the equation

$$\ddot{\vec{r}} = \frac{c^2}{2}\nabla n^2 \tag{1.38}$$

Substituting the LL refractive index equation (1.1) in the differential equation (1.30), or equation (1.38), we obtain an equation of motion which describes the ray paths inside an LL, that is

$$\ddot{\vec{r}} + \frac{c^2}{R^2}\vec{r} = 0 \tag{1.39}$$

Now, we proceed to the solution of the equation (1.39). Using the boundary conditions $\vec{r}(0) = \vec{r}_0 = (x_0, y_0)$ and $\dot{\vec{r}_0} = \vec{k}_0 = (k_{0x}, k_{0y})$ we obtain

$$\vec{r}(t) = \vec{r}_0 \cos\left(\frac{c}{R}t\right) + \vec{k}_0 \frac{R}{c} \sin\left(\frac{c}{R}t\right) \tag{1.40}$$

or in Cartesian coordinates

$$\begin{pmatrix} x(t) \\ y(t) \end{pmatrix} = \begin{pmatrix} x_0 \\ y_0 \end{pmatrix} \cos\left(\frac{c}{R}t\right) + \begin{pmatrix} k_{0x} \\ k_{0y} \end{pmatrix} \frac{R}{c} \sin\left(\frac{c}{R}t\right) \tag{1.41}$$

The solution (1.41) describes elliptical orbits in the two dimensional surface formed by (x, y) coordinates, in agreement with Luneburg's theory [4] as well as with ray equations (1.16) and (1.17) [6].

In Fig.1.3, we present results based on the explicit ray solutions of the equations (1.40) and (1.41). The ray tracing propagation through a single LL with initial propagation angle $\theta = 0$, is indicated in Fig.1.3a; this is in agreement with the results obtained by the quasi 2D ray solution as they are shown in Fig.1.1a. In the Figs1.3(b - c) the propagation with $\theta = \pm\pi/3$ are indicated, showing that the methods that are developed in Sections 1.2 and 1.3 holds for backscattered rays unlike with quasi 2D approach which fails to describe the backscattering propagation (Fig.1.2).

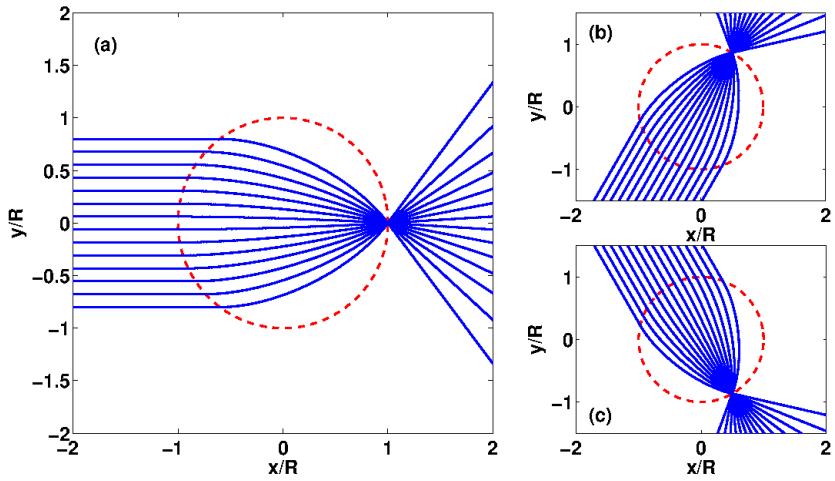

Figure 1.3: The red dashed lines denote Luneburg lenses (LL) whereas the blue lines show the ray tracing performed through the analytical parametric solution of equations (1.40) and (1.41). Ray tracing through a single LL is plotted for initial propagation angle (a) $\theta = 0$, (b) $\theta = \pi/3$ and (c) $\theta = -\pi/3$.

1.4 Numerical solution of Maxwell equations

The EM waves propagation as well as the interaction between light and matter are fully described by Maxwell's field equations. Since we cannot find analytical solutions of Maxwell equation for the most problems in nature, due to the anisotropic materials, nonlinearity, complex geometries etc, we have to resort to numerical methods for solving Maxwell equations, such as Green functions, finite elements, finite volumes, Fourier expansions, asymptotic, pseudospectral, integration and finite difference methods. In this Thesis, we are going to develop and use a finite difference method.

The Finite Difference in Time Domain (FDTD) method is a well known numerical approach used for modelling computational electrodynamics; while most numerical methods are applied in the frequency domain, FDTD solves the time dependent Maxwell equations in the time domain, viz. the calculation of the EM field progresses at discrete steps both in time and space. Since it is a time domain method, FDTD solutions can cover a wide frequency range with a single simulation. Furthremore, FDTD is applied in several scientific and technology areas dealing with EM wave propagation such as antennas, radiation and microwave applications, as well as the inter-

action between EM waves with material structures such as plasmonics and photonic crystals.

The FDTD was firstly introduced by Yee, presented in his seminal paper [10], where he applied centered finite difference operators in both space and time for each electric and magnetic vector field component in Maxwell's curl equations. Finally, the descriptor *Finite Difference in Time Domain* as well as the acronym of the FDTD method was given by Taflove almost fifteen years later than Yee, in his article [11].

The initial point of the FDTD method is the Maxwell equations in matter (equations (1.42) and (1.43)); assuming no free charges or currents, the Maxwell curl equations can be written as

$$\nabla \times \vec{E} = -\frac{\partial \vec{B}}{\partial t} \tag{1.42}$$

$$\nabla \times \vec{H} = \frac{\partial \vec{D}}{\partial t} \tag{1.43}$$

Where $\vec{E}$ is the electric field intensity, $\vec{D}$ the electric flux density, $\vec{B}$ is the magnetic flux density and $\vec{H}$ the magnetic field intensity, where all of them are in general time depended.

In addition we have also the constitutive relations, which reveal how fields interact with the mater, that is

$$\vec{B} = \mu \vec{H} \tag{1.44}$$

$$\vec{D} = \varepsilon \vec{E} \tag{1.45}$$

where ε and μ are permittivity and permeability respectively, which are in general depended on spatial location within the medium that is studied, i.e. $\varepsilon \equiv \varepsilon(\vec{r})$ and $\mu \equiv \mu(\vec{r})$.

Gathering the Maxwell equations (1.42)(1.43) together with constitutive relations (1.45)(1.44) we obtain

$$\frac{\partial \vec{H}}{\partial t} = -\frac{1}{\mu} \nabla \times \vec{E} \tag{1.46}$$

$$\frac{\partial \vec{E}}{\partial t} = \frac{1}{\varepsilon} \nabla \times \vec{H} \tag{1.47}$$

In this Thesis, we are interested in two dimensional (2D) transverse magnetic polarization (TM) EM waves, that is, $\vec{E} = (0, 0, E_z)$ and $\vec{H} = (H_x, H_y, 0)$, where z is the propagation axis, E_z the z component of the electric field and H_x, H_y the transverse components of the magnetic field.

Subsequently, the differential system of vector equations (1.47) (1.46) becomes to a system of three scalar partial differential equations (PDE), that is

$$\frac{\partial H_x}{\partial t} = -\frac{1}{\mu}\frac{\partial E_z}{\partial y} \tag{1.48}$$

$$\frac{\partial H_y}{\partial t} = \frac{1}{\mu}\frac{\partial E_z}{\partial x} \tag{1.49}$$

$$\frac{\partial E_z}{\partial t} = \frac{1}{\varepsilon}\left(\frac{\partial H_y}{\partial x} - \frac{\partial H_x}{\partial y}\right) \tag{1.50}$$

The FDTD method employs the second order accurate central-difference approximations both to the space and time partial derivatives, in order to discretize and solve the PDE system of equations (1.48) (1.49) and (1.50) [10,11]. Consider a second order Taylor expansion of an arbitrary one dimensional function $f(x)$ expanded around the point x_0 with an offset of $\frac{\Delta x}{2}$, that is

$$f\left(x_0 + \frac{\Delta x}{2}\right) = f\left(x_0\right) + \frac{\Delta x}{2}\left.\frac{\partial f}{\partial x}\right|_{x_0} + \frac{1}{2!}\left(\frac{\Delta x}{2}\right)^2\left.\frac{\partial^2 f}{\partial x^2}\right|_{x_0} \tag{1.51}$$

$$f\left(x_0 - \frac{\Delta x}{2}\right) = f\left(x_0\right) - \frac{\Delta x}{2}\left.\frac{\partial f}{\partial x}\right|_{x_0} + \frac{1}{2!}\left(\frac{\Delta x}{2}\right)^2\left.\frac{\partial^2 f}{\partial x^2}\right|_{x_0} \tag{1.52}$$

Subtracting the equation (1.52) from the equation (1.51) and dividing by Δx yields to the central-difference approximation

$$\left.\frac{\partial f}{\partial x}\right|_{x_0} = \frac{f\left(x_0 + \frac{\Delta x}{2}\right) - f\left(x_0 - \frac{\Delta x}{2}\right)}{\Delta x} \tag{1.53}$$

Having now an expression to calculate first derivatives, we proceed to central ideas of FDTD method. First of all, FDTD replaces all the derivatives in Maxwell equations (1.48) (1.49) (1.50) with finite differences; discretizes space and time so that the electric and magnetic fields are staggered in both space and time. Moreover, FDTD solves the resulting difference equations obtaining the "update equations" that express the unknown future fields in terms of the past fields. Therefore the magnetic fields are evaluated at one time step and they are used for evaluating of the electric field in the same time step. The last step is repeated until the fields reach to the steady state. A schematic algorithm of an FDTD code and the discretized equations are given in the Appendix B.

Since we are working on two dimensional EM wave propagation, we need two space grid size, i.e. Δx and Δy and one for the time, i.e. Δt. The size

of these steps have to satisfy two stability conditions. Firstly, the smaller of the spatial grid sizes, say Δx, has to be much smaller than the wavelength which corresponds to higher frequency of the problem, i.e. $\Delta x << \lambda_{min}$. For the most problems the choice $\Delta x = \lambda_{min}/10$ gives very good accurate, but there are several problems, where smaller grid size is necessary; in our case we use smaller grid space, viz. $\Delta x = \lambda_{min}/20$. Secondly, there is a condition between time increment and the space increments, called Courant limit. This stability criterion states that the time grid size Δt must be small enough compared to the longest wavelength (which correspond to the highest wave propagation velocity c_{max}), in order to not outrun the spacial grid size $\Delta s = \sqrt{(\Delta x)^2 + (\Delta y)^2}$, subsequently

$$\Delta t < \frac{\sqrt{(\Delta x)^2 + (\Delta y)^2}}{c_{max}} \tag{1.54}$$

where the c_{max} is related with dielectric constants and consequently with refractive index n, as $c_{max} = c_0/\sqrt{\varepsilon\mu} = c_0/n$, where c_0 the velocity of light in the vacuum. As a result, the EM characteristics of the materials, which are used in the problem, rule the size of time and space grid size.

FDTD method supports all kinds of the EM wave sources for a single or a range of frequencies, such as plane waves, point sources, Gaussian pulses, square waves etc. In this Thesis we are working with monochromatic plane wave sources.

Finally, as it has been already mentioned, FDTD method calculates , and gives as output, the components of the electric and magnetic fields, i.e. for TM mode the E_z, H_x and H_y components; we obtain either a snapshot of these components, for a specific time or the intensity of fields under steady state conditions. Furthermore, for the intensity calculation, the FDTD simulation is running until the steady state of fields achieved and afterwards we integrate the square of the absolute value of the electric and magnetic components, over a single or more periods. In this Thesis, we are working with the intensities of the EM fields.

We apply the FDTD method for a monochromatic EM plane wave source with wavelength λ, with vacuum as the bulk material, with permittivity $\varepsilon = 1$. We use an LL with radius $R = 10\lambda$ and permittivity based on the equation (1.1) i.e. $\varepsilon = n^2 = 2 - (r/R)^2$. We compute an FDTD simulation for EM propagation via a single LL; we present in Fig.1.4 the steady state intensity of the electric field as it is computed by FDTD simulations, verifying the analytical results that are indicated in Figs.1.1a and 1.3a.

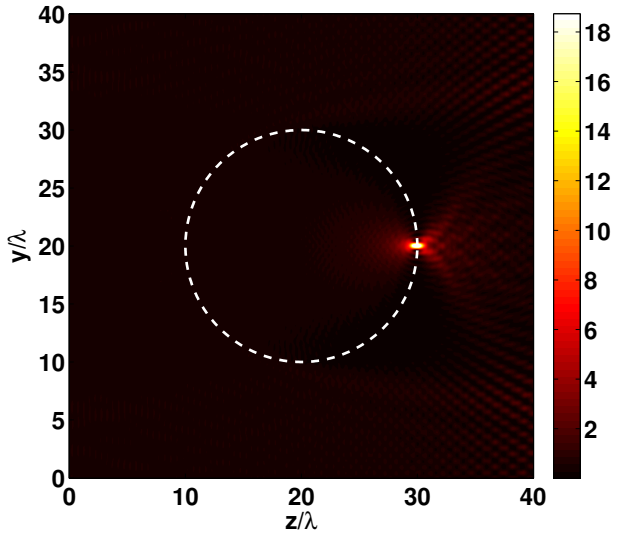

Figure 1.4: FDTD simulation. The white dashed line denotes a Luneburg Lens (LL). We present the intensity I of a monochromatic EM wave which is propagating through a single LL.

Chapter 2

Networks of lenses

In the previous Chapter, we developed four methods in order to investigate the light propagation through a given function of refractive index $n(r)$ (or permittivity $\varepsilon(r)$), which has in general space dependence. In this Chapter these methods are applied to investigate the EM wave propagation through certain configurations of Luneburg Lenses (LLs). The main point of this Chapter is the formation of LL waveguides (LLW) through the arrangement of multiple LLs in geometrically linear or bent configurations [6]. Afterwards, we proceed with a beam splitter device based on LL arrangement as an example for LLW application. We present EM wave propagation results obtained by the LL parametric ray tracing solution of equation (1.41) as well as by FDTD simulations.

2.1 Waveguides formed by Luneburg lens networks

A general continuous GRIN waveguide may be hard to analyze in more elemental units and relate its global features to these units. In this Section, we adopt precisely this latter avenue, viz. attempt to construct waveguide structures that are seen as lattices, or networks, of units with specific features. This is a "metamaterials approach", where specific properties of the "atomistic" units are inherited as well as expanded in the network. The "atomic" unit of the networks that we are going to discuss is an LL and the important property of this "atomistic" unit is that the focal point is predefined for parallel rays that enter in an LL (for any initial angle) [4, 6].

We proceed with Fig.2.1 and Fig.2.2 where LLW formation through the arrangement of multiple LLs [6] are shown. Firstly, we design two linear LLW formed by five and six LLs respectively. Afterwards we make an 180^o

reversed bend waveguide formed by seventeen LLs and finally we make a full circle LLW formed also by seventeen LLs. Fig.2.1 represents ray tracing propagation found by the analytical ray solution that is given by the equation (1.41), whereas in Fig.2.2 we present FDTD simulations for the same structures as in Fig.2.1. In all cases studied, the numerical solution of Maxwell's equations is compatible with the findings obtained through the ray tracing map.

Two geometrically linear arrangements of touching LLs on a straight line are shown in Figs. 2.1(a,b) and Figs.2.2(a,b). Depending on the number of lenses, odd or even number, the EM wave focus in the last LL surface or exit as it entered (as a plane wave in the present case) respectively. In both cases we sent a beam parallel to the axis of symmetry of the LL network, i.e. parallel to x axis for the ray tracing and z axis for the FDTD simulations. In Figs.2.1(c,d) and in Figs.2.2(c,d), we form an 180^o reversed bend waveguide and a full circle bend waveguide through a sequence of seventeen LLs and we proceed with light propagation in the geometric optics limit. We show that light can propagate efficiently through a loop, signifying that arbitrary waveguide formation and guiding is possible.

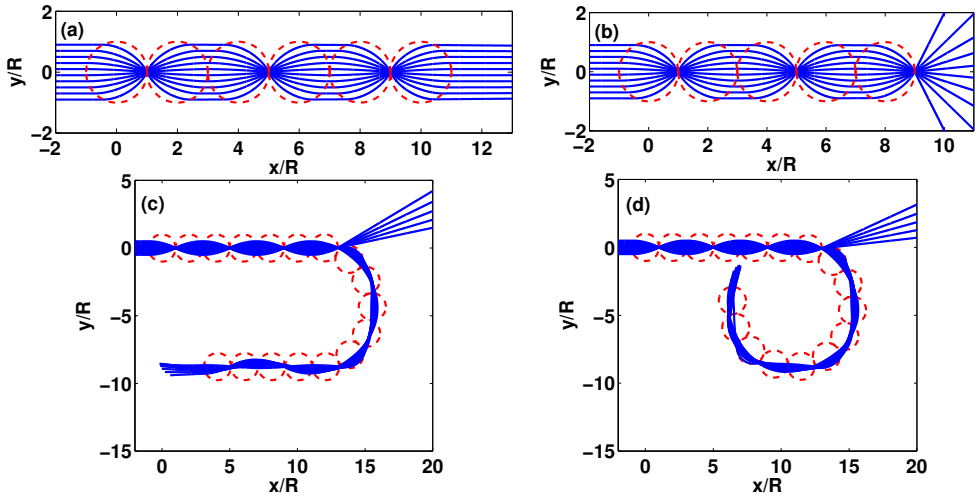

Figure 2.1: The red dashed lines denote the arrangement of LLs. The blue lines show the ray tracing performed through the analytical parametric ray solution of the equation (1.41). Light is guided by LLs across the linear network constituted of six LLs in (a) and of five LLs in (b). In (c) seventeen LL form an 180^o reversed bend waveguide and a full circle bend waveguide in illustrated in (d).

The LL network cases presented (linear, reversed bend and full circle

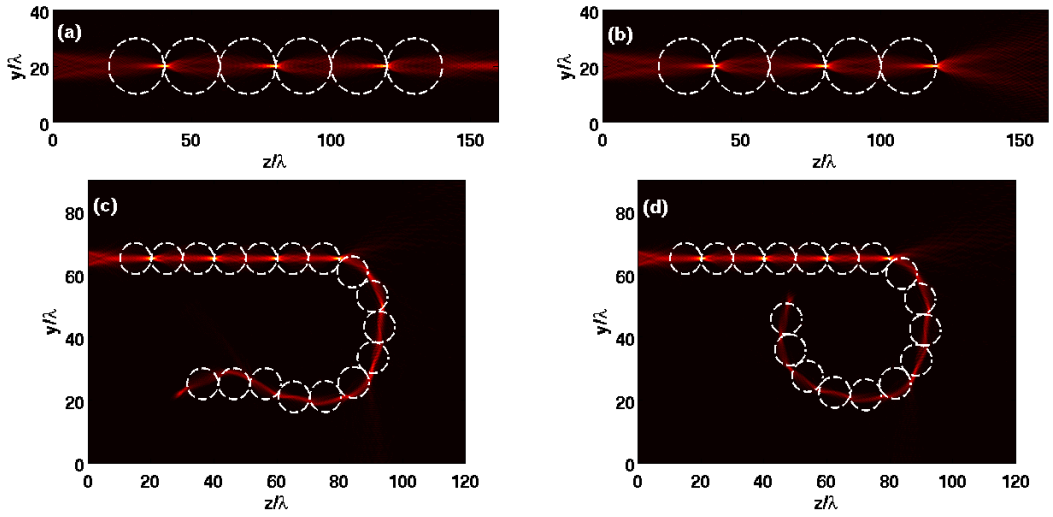

Figure 2.2: FDTD simulation. The white dashed lines denote the arrangement of LLs. We present the intensity I of an EM wave which is propagating through (a) a linear LL waveguige formed by six LLs (b) a linear LL waveguide formed by five LLs (c) through an 180^o reversed bend waveguide formed by seventeen LLs (d) and through a full circle bend waveguide formed also by seventeen LLs.

curved) signify that LLs may be used as efficient waveguides. Their advantage over the usual dielectric guides is that light bending occurs naturally through the LL properties while the outgoing light may be also focused, if so desired. In bends, there are naturally some losses that, in the geometric optics limit, may be estimated by comparing the number of the incoming to the outgoing rays, namely N_{IN} versus N_{OUT} respectively; in the EM wave propagation we can measure the incoming electric field intensity I_{IN} and compare it with the outgoing I_{OUT}. In the linear arrangement of LLWs, as in Figs.2.1 (a,b) and Figs.2.2 (a,b), the performance is perfect. In the bend cases, such as in the 180^o reversed bend arrangement of Fig.2.1c and Fig. 2.2c as well as in the full circle bend waveguide of Fig.2.1c and Fig.2.21c, the losses are measured about 40% [6]. We note that the aforementioned losses depend also on the ray coverage of the initial lens as well as the sharpness of the bend; the losses can be reduced by manipulating appropriately these two factors.

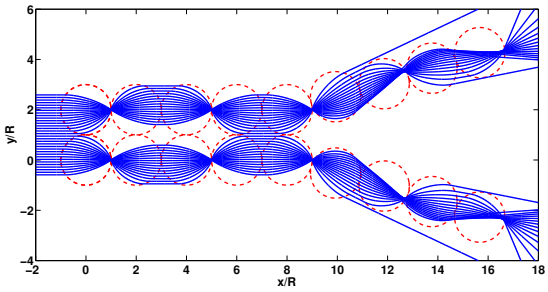

Figure 2.3: A beam splitter device formed by twenty LLs. The red dashed lines denote the LL network whereas the blue solid lines show the ray tracing performed through the analytical parametric solution of equation (1.41).

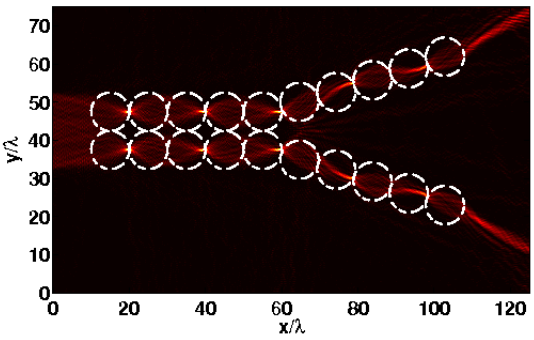

Figure 2.4: FDTD simulation. A beam splitter device formed by LLW. The white dashed lines denote the LL network. We show the intensity I of the electric field of an EM plane wave which is propagating through a beam splitter device formed by twenty LLs.

2.2 Beam splitter

A simple but useful application of the LLWs may be a beam splitter, viz. a device which splits and guides EM waves. LLWs as well as beam splitters may be used to enhanced light manipulation in a variety circumstances, for instance they can be used in fabrication of integrated photonic circuits.

In Fig.2.3 and Fig.2.4 a beam splitter device is represented. Twenty LLs have been arranged in order to split a bundle of rays and afterwards to guide in different directions. The losses are measured as the 10%, subsequently the 90% of the incoming rays are split and guided through LLs configuration of Fig.2.3 and Fig.2.4.

Chapter 3

Branching flow

When waves propagate through random media many, interesting phenomena occur, such as the branching onset of caustic areas, Anderson localization and rogue wave formation. Recently, these phenomena have received considerable attention by theoretical physicists and engineers. Typical cases include electron flow in a two dimensional electron gas (2DEG) [12–14], transport properties of semiconductors [12–14], ocean waves [15], linear and nonlinear light propagation in random fibers [16–18], sound wave propagation [19–21], microwave devices [22, 23], resonance in nonlinear optical cavities [24] and light propagation through random refractive index media [5, 25–29].

In this Chapter, we focus on branching effects that occur in two dimensional conservative particle flow as well as in EM wave propagation through a weak random potential. Even if the random potential is very weak, the flow can be strongly affected resulting in caustics branches [12, 13, 30]. We present the theoretical framework that has been developed for the quantification of branching effects in a two-dimensional particle or/and EM waves flow. Specifically, we show that caustics can take place in the propagation of light via a disordered network of lenses and we highlight the similarities between light propagation and particle flow.

3.1 Statistics of caustics

We present the theoretical framework for caustics, based in the Lagrangian manifold (LM) approach, in order to obtain analytical results for the statistics of caustics. The LM approach offers the opportunity to adequately understand the phase space geometry of caustics. The obtained analytical results are general and hold for a variety of problems, since the initial point of this analysis is an ordinary Hamiltonian of equation (3.1). An appropriate way

to study the branched flow is to analyse the statistics of caustics, because each caustic is followed by a branched flow.

We begin with an ordinary Hamiltonian of the form

$$H = \frac{\vec{p}^2}{2m} + V(t, \vec{x}) \tag{3.1}$$

where $\vec{x}$ is the position vector, $\vec{p}$ the conjugate momenta and t the time. The Hamiltonian of the equation (3.1) yields to a Hamilton-Jakobi-Equation (HJE) [7,8], where the last equation is a first order non-linear partial differential equation given by

$$\frac{\partial}{\partial t} S(t, \vec{x}) + H = 0 \tag{3.2}$$

where $S(t, \vec{x})$ is the classical action which is associated with the conjugate momenta vector as

$$\vec{p}(\vec{x}) = \frac{\partial S(\vec{x})}{\partial \vec{x}} \tag{3.3}$$

Equation (3.2) thus becomes (by substituting equation (3.3) and equation (3.1) in equation (3.2) and assuming particles with unit mass $m = 1$)

$$\frac{\partial}{\partial t} S(t, \vec{x}) + \frac{1}{2} \left(\frac{\partial S}{\partial \vec{x}} \right)^2 + V(t, \vec{x}) = 0 \tag{3.4}$$

For "weak" potentials, we can use the quasi two dimensional (quasi 2D) or the paraxial approximation, where we have only one spatial coordinate, viz. $\vec{x}(t) \equiv y(t)$, with time t playing the role of the propagation axis, as it is discussed in Section 1.1. From the mathematical view, we deal with an one dimensional (1D) HJE with a time dependent potential, viz. $V(t, y(t))$.

The curvature u of the action S is defined as the partial derivative of conjugate momenta p with respect to position y, namely

$$u \equiv \frac{\partial p}{\partial y} = \frac{\partial^2 S}{\partial y^2} \tag{3.5}$$

In order to obtain a differential equation for the curvature u, we differentiate twice the equation (3.4) with respect to the position y and use the definitions of the equations (3.3)(3.5) [13, 25, 26], we have

$$\begin{aligned} &\frac{\partial}{\partial t} u + \frac{\partial S}{\partial y} \frac{\partial}{\partial y} u + u^2 + \frac{\partial^2}{\partial y^2} V(t, y) = 0 \\ &\left[\frac{\partial}{\partial t} + p \frac{\partial}{\partial y} \right] u + u^2 + \frac{\partial^2}{\partial y^2} V(t, y) = 0 \end{aligned} \tag{3.6}$$

The operator in the brackets of the equation (3.6) is known as the convective or material derivative [13, 31], turning the differential equation from partial differential equation (PDE) into an ordinary differential equation (ODE) and, thus, the Eulerian into a Lagrangian framework.

Subsequently, we obtain the ODE

$$\frac{d}{dt}u + u^2 + \frac{\partial^2}{\partial y^2}V(t,y) = 0 \tag{3.7}$$

The next step is to introduce a random white noise. Since we are interested in particle flow or wave propagation via a random weak potential, we assume that the potential acts as a white noise $\Gamma(t)$ with delta correlation function, that is $c(t-t') = \langle \Gamma(t)\Gamma(t') \rangle = 2\delta(t-t')$, only in the propagation direction t, because of the paraxial approximation [12, 13, 22, 25, 26]. The correlation function $c(t,y)$ of the stochastic term $\partial_{yy}V(t,y)$ of the equation (3.7) is

$$c(t-t', y-y') = \langle \partial_{yy}V(t,y)\ \partial_{y'y'}V(t',y') \rangle = \partial_{yy}\partial_{y'y'}\ c(t-t', y-y')$$

$$c(t-t', y-y') = 2\delta(t-t')\partial_{yy}\partial_{y'y'}c(y-y') \tag{3.8}$$

Although we assume that the random noise $\Gamma(t)$ acts only in the propagation direction t, we have to retain the characteristics of the random potential in the transverse axis y as well. This can be achieved by keeping constant the integral over the derivatives of the correlation function $c(y-y')$ as [12, 13, 25, 26]

$$\sigma^2 = \frac{1}{2}\int_{-\infty}^{\infty} \frac{\partial^4}{\partial y^4}c(t,y)\bigg|_{y=0} dt \tag{3.9}$$

where σ is the standard deviation of the potential and thus σ^2 is the variance. The constant coefficient D will be identified later as the diffusion coefficient and related with standard deviation σ as

$$D = 2\sigma^2 \tag{3.10}$$

Finally, the ODE (3.7) becomes an ordinary stochastic differential equation (OSDE) viz.

$$\frac{du(t)}{dt} = -u^2(t) - \sigma\ \Gamma(t) \tag{3.11}$$

In the following, we use the Fokker Plank Equation (FPE), which is a partial differential equation describing the time evolution of the probability density function derived from an ordinary stochastic differential equation (OSDE) [13, 32, 33] of the form (in one-dimensional case)

$$\dot{y}(t) = f(y) + g(y)\Gamma(t) \tag{3.12}$$

where f and g are arbitrary functions of y and Γ is a Gaussian delta-correlated white noise. The corresponding FPE for the density function $P(y,t)$ reads [32, 33]

$$\frac{\partial}{\partial t}P(y,t) = \left[-\frac{\partial}{\partial y}D^{(1)}(y,t) + \frac{\partial^2}{\partial y^2}D^{(2)}(y,t)\right]P(y,t) \tag{3.13}$$

with drift and diffusion coefficients $D^{(1)}$ and $D^{(2)}$ respectively, calculated by equation (3.12) according to the relations [32, 33]

$$D^{(1)}(y,t) = f(y) + g(y)\frac{\partial}{\partial y}g(y) \tag{3.14}$$

$$D^{(2)}(y,t) = g^2(y) \tag{3.15}$$

In addition to FPE, there is an equivalent backward Fokker Plank Equation (BPFE) (equation (3.16), presented below), in which the space independent variable is a function of the initial position y_0. The main difference between the forward FPE and the backward FPE is the fact that in the former (forward FPE) the initial value for the probability density P is given, i.e. $P(y_0, t_0)$ and, therefore, FPE describes the time evolution of this density $P(y,t)$ for time $t > t_0$. On the other hand, in the BFPE the final condition $P(y_f, t_f)$ is given, where y_f, t_f are the final values of variables y and t, while the initial conditions are unspecified. The BFPE is very useful for the solution of the problems where we know the final state of process but we are not interested in (or we do not know) the initial conditions. For convenience, we use the notation P for the probability density of the forward FPE and p_f for the backward FPE [32, 33].

$$\frac{\partial}{\partial t_0}p_f(y,t) = \left[-D^{(1)}(y_0,t_0)\frac{\partial}{\partial y_0} + D^{(2)}(y_0,t_0)\frac{\partial^2}{\partial y_0^2}\right]p_f(y,t) \tag{3.16}$$

Now we proceed to derive the drift and the diffusion coefficients, based on equations (3.12, 3.14, 3.15) for the OSDE of equation (3.11), that is

$$D^{(1)} = -u^2 \tag{3.17}$$

$$D^{(2)} = \sigma^2 = \frac{D}{2} \tag{3.18}$$

Subsequently, the FPE of our problem, viz. for the OSDE 3.11 , is given by the equations (3.13, 3.17, 3.18), namely

$$\frac{\partial}{\partial t}P(u,t) = \left[\frac{\partial}{\partial u}u^2 + \frac{\partial^2}{\partial u^2}\frac{D}{2}\right]P(u,t) \tag{3.19}$$

In order to find how long it is needed to reach a caustic for the first time, viz. when the solution of FPE becomes infinity for the first time ($u(t_c) \to \infty$, where t_c is the mean time of this process), we ask the inverse question, that is, what is the probability that no singularity appears until time t, (meaning that when a singularity appears, the process is terminated). This analysis can be performed by means of the BFPE [13, 25, 26]. Using the form of equation (3.16) with coefficients given by equations (3.17) and (3.18), we obtain the BFPE

$$\frac{\partial}{\partial t} p_f(u,t) = \left[-u_0^2 \frac{\partial}{\partial u_0} + \frac{D}{2} \frac{\partial^2}{\partial u_0^2} \right] p_f(u,t) \tag{3.20}$$

where u_0 the initial curvature.

We proceed with the calculation of the mean time $\langle t_c(u_0) \rangle$ which an initial curvature u_0 needs to go to infinity, resulting in a caustic. According to basic probability theory, the mean time $\langle t_c(u_0) \rangle$ is given by means of the probability density p_f by the relation

$$\langle t_c(u_0) \rangle = \int_0^\infty t p_f \, dt \tag{3.21}$$

In order to calculate $\langle t_c(u_0) \rangle$, we multiply the BFPE of equation (3.20) and integrate over time t. The left hand side can be evaluated by means of the integration by parts method, resulting in

$$\int_0^\infty t \frac{\partial}{\partial t} \, p_f \, dt = t p_f |_0^\infty - \int_0^\infty p_f \, dt = 0 - 1 = -1 \tag{3.22}$$

In which we have assumed that the probability density p_f is normalized to unity, i.e. $\int_0^\infty p_f = 1$, and furthermore, it vanishes as time approaches infinity resulting in $p_f(t \to \infty) = 0$. The left hand side does not include derivatives with respect to t and, therefore, the integration is trivial; the equation thus becomes

$$-1 = -u_0^2 \frac{d}{du_0} \langle t_c(u_0) \rangle + \frac{D}{2} \frac{d^2}{du_0^2} \langle t_c(u_0) \rangle \tag{3.23}$$

where we have used the definition of equation (3.21) and transformed the partial derivatives (with respect to u_0) to full derivatives, since the time derivatives vanish. Equation (3.23) is a second order inhomogeneous differential equation of the form

$$y''(x) + f(x) \, y'(x) = g(x)$$

with exact solution given by [34]

$$y(x) = C_1 + \int e^{-F} \left(C_2 + \int e^F g dx \right) dx \quad \text{where} \quad F = \int f dx \tag{3.24}$$

Using equation (3.24) along with the boundary conditions

$$\lim_{u_0\to-\infty}\langle t_c(u_0)\rangle = 0 \quad \text{and} \quad \lim_{u_0\to\infty}\langle t_c(u_0)\rangle = \text{finite} \tag{3.25}$$

we obtain the final solution for the mean time $\langle t_c(u_0)\rangle$ in terms of a double integral form [13, 25, 26], thus

$$\langle t_c(u_0)\rangle = \frac{2}{D}\int_{-\infty}^{u_0} e^{2\xi^3/3D}\int_{\xi}^{\infty} e^{-2\eta^3/3D}d\eta d\xi \tag{3.26}$$

Since we are interested only for a scaling law of the first caustic location (or time), we may find analytically the behaviour of the solution of the integral of equation (3.26). That is, we introduce two new variables μ and ν and therefore we make the notations $\xi = \frac{3}{2}D^{1/3}\mu$ and $\eta = \frac{3}{2}D^{1/3}\nu$, subsequently the double integral solution (3.26) becomes

$$\langle t_c(u_0)\rangle = \frac{9}{2}D^{-1/3}\int_{-\infty}^{\left(\frac{2u_0^3}{3D}\right)^{1/3}} e^{\mu^3}\int_{\left(\frac{2\mu^3}{3D}\right)^{1/3}}^{\infty} e^{-\nu^3}d\nu d\mu \tag{3.27}$$

The double integral with the prefactor 9/2 of the equation (3.27) can be defined as a constant unknown function $g(u_0, D)$ reveals the scaling behaviour $\langle t_c(u_0)\rangle \sim D^{-1/3}$, that is

$$\langle t_c(u_0)\rangle = g(u_0, D)D^{-1/3} \tag{3.28}$$

or in terms of standard deviation (regarding to the relation (3.10))

$$\langle t_c(u_0)\rangle = g(u_0, D)\sigma^{-2/3} \tag{3.29}$$

In addition, the integral in equation (3.26) can be evaluated numerically for a plane wave or point source condition, i.e. $u_0 = 0$ or $u_0 = \infty$ respectively, giving a numerical value for the characteristic mean time (or, equivalently, the distance from the source in the quasi 2D approximation) from a plane or from a point source respectively, where the first caustic appears [13, 25, 26], that is

$$\langle t_c(0)\rangle = 4.18D^{-1/3} \quad \text{and} \quad \langle t_c(\infty)\rangle = 6.27D^{-1/3}$$

Employing equation (3.10) we can rewrite the results in terms of standard deviation σ as

$$\langle t_c(0)\rangle = 3.32\sigma^{-2/3} \quad \text{and} \quad \langle t_c(\infty)\rangle = 4.98\sigma^{-2/3} \tag{3.30}$$

The quantity $\langle t_c(0)\rangle$ describes the mean distance of the appearance of the focus for an initial plane wave, whereas the quantity $\langle t_c(\infty)\rangle$ describes the

mean distance between two subsequent caustics, since any caustic can be assumed as a point source.

At this point, we would like to point out that we can derive to same results if we start from the parabolic equation (or Schrödinger like equation)

$$2ik\frac{\partial}{\partial t}\psi + \nabla^2\psi + k^2\varepsilon(t,\vec{r})\psi = 0 \tag{3.31}$$

which is also well known approximation for wave fields, in addition to the Hamiltonian of equation (3.1) which describes the light propagation as it was shown in Sections 1.2 and 1.3 (see the Hamiltonians of the equations (1.26) and (1.37)) [2, 5, 25, 26]. Here, the time t is also the propagation axis (as the paraxial approximation states), $\psi = \psi(t, \vec{r})$ is any component of electric or magnetic field, k is the wavevector and ε is the fluctuation part of the dielectric permittivity (or refractive index). In this case, the classical action S, which is defined by equation (3.3), is the phase front of the EM wave, and the curvature u denotes the curvature of the phase front; ε is a random potential [25,26]. More details about the derivation of equation (3.31), as well as how this equation yields to the same FPE (3.19) are given in Appendix C.

These results prove that caustic formation is a general phenomenon, which takes place in conservative particle flows as well as in wave propagation via a weak delta-correlated random potential. We have shown that the characteristic mean distance from the source, where the first caustic occurs, is universal for all such systems and it is given in terms of standard deviation of the random potential according to the relations (3.30).

In the following Sections we present numerical results obtained by running simulations of particle flows and wave propagation systems; the numerical results are in agreement (and, thus, verify) the analytical results presented in this Section (3.1).

3.2 Branching flow in physical systems

Numerical simulations and experiments have revealed that branching flows can arise in a variety of physical systems. Topinka *et al.* [14] have shown experimentally that branching flow takes place in electron flow through a two dimensional electron gas (2DEG). Kaplan [30] and Metzger [13] have studied both analytically and numerically the branching flow in electron propagation and have found that the scaling law, which is governing the scaling behavior of the first caustic position, is the one described in Section 3.1 (equation (3.30)). In addition, Metzger *et al.*, in [12], have found an analytical expression for the number of branches that occur at all distances from the

source. Moreover Barkhofen *et al.* [22] have found, both experimentally and numerically, branching effects in microwave flow through disordered media fabricated by randomly distributed scatterers; additionally, they have shown that the statics of the first caustic position, in such process, satisfies the scaling rule described by equation (3.30). Another microwave study, which has been performed by Hohmann *et al.* [23], found by means of the ray dynamics method and by wave propagation simulations, that branching flow can emerge in two dimensional microwave propagation through media which comprises by random metallic scatterers. Furthermore, Ni *et al.* [28] have studied the EM wave propagation in an optical system comprising random scatterers with continuous refractive index, and have proposed that branched waves can emerge as a general phenomenon between the weak scattering limit and the Anderson localization. In addition, they have found that high intensities (i.e. caustics or other extreme events) are distributed following an algebraic law. Finally, a numerical investigation on sound waves has been performed by Blanc-Benon *et al.* [19] showing that branching flow can arise from high frequency sound wave propagation through a turbulent field; experiments performed by Wolfson in [21] confirms the numerical findings.

In order to check the validity of the theoretical methods presented in Section 3.1, we introduce a method and a toy model with a single LL in order to investigate the location of the first caustic and then, we proceed to show that the numerical results agree with the theoretical prediction of equation (3.30). As it has already been mentioned, caustics are high intensity areas, as a result high deviation of the mean value of the intensity I is expected to appear in the intensity statistics of the wave flow, resulting in a maximum of the standard deviation of the intensity of flow. As a result, a simple measure to investigate the caustics is given by the scintillation index [22, 35] of equation (3.32), as a function of the propagation distance, viz. x, where I is the wave intensity and the average is taken over many realizations of the random potential. The maximum of the scintillation index, (a pick in the curve of σ_I), denotes the onset of a caustic; subsequently, peaks for different values of standard deviation σ (of the random potential) are expected to be scaled as the equation (3.30) predicts.

$$\sigma_I^2 = \frac{\langle I(x)^2 \rangle}{\langle I(x) \rangle^2} - 1 \tag{3.32}$$

An alternative measure to the scintillation index σ_I^2 is to average over the transverse direction, namely y, as it is given by equation (3.33). This is a

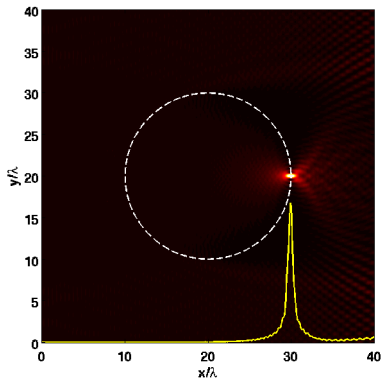

Figure 3.1: FDTD simulation for EM wave propagation through a single LL is illustrated; LL is shown by the dashed white line, the lighter color denotes high intensity and the darker one is for lower intensity. The yellow solid line is the scintillation index, σ_I^2, given by equation (3.32). As can been seen, σ_I^2 takes its maximum value in the focus point, as it is expected.

more appropriate method when the average is taken over a few realizations.

$$s_I^2 = \frac{\langle I(x)^2 \rangle_y}{\langle I(x) \rangle_y^2} - 1 \tag{3.33}$$

Fig. 3.1 shows that the peak of scintillation index σ_I^2 (yellow curve) appears in the same position where the EM wave is focused by an LL, proving that σ_I is an efficient way to investigate caustics. The Fig. 3.2 represents numerical results obtained by Ref. [22], for the scintillation index curve $\sigma_I^2(x)$ for several values of potential strength ε, where ε is proportional to standard deviation σ of the random potential; the scaling law of equation (3.30) is revealed and confirmed.

3.3 Caustic formation in optics

In this Section, we present results from the numerical simulations of EM plane waves through a random transparent medium consisting of randomly located LLs, each with refractive index profile given by equation (1.1). The simulations are performed by the FDTD method, as described in Section 1.4.

In order to investigate the branching flow for several values of standard deviation σ of the random potential, we introduce a strength parameter α in the LL refraction index function (1.1); this control parameter α is proportional to the standard deviation, i.e. $\sigma \sim \alpha$; the analytical calculations for the standard deviation of the generalized LL potential are given in Appendix D. The generalized LL refractive index function is then given by the equation

$$n(r) = \sqrt{\alpha \left(n_L^2 - 1\right) + 1} \tag{3.34}$$

where n_L denotes the original LL refraction index, given by equation (1.1).

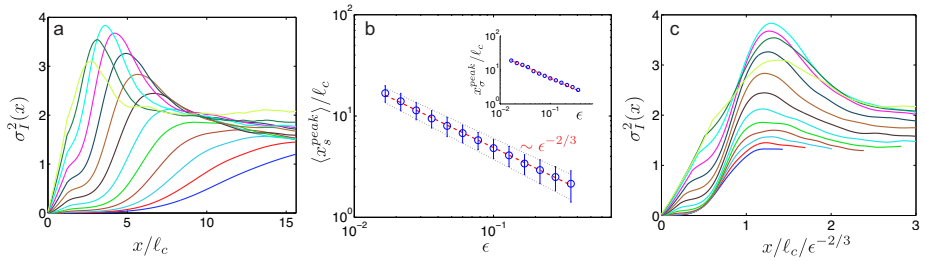

Figure 3.2: Scaling of the branching length with the strength of the random potential ϵ. (a) Scintillation index $\sigma_I^2(x)$ as a function of the distance from the source for different values of ϵ. (b) Peak positions of the scintillation curves obtained from $s_I^2(x)$ and $\sigma_I^2(x)$ (inset). Both curves show a scaling of $\epsilon^{-2/3}$ (red dashed lines). The black dotted lines indicate the standard deviation of the individual peak positions around their mean value. The scaling is confirmed in panel (c), where the curves from the left panel are shown with a rescaled x axis, on which all peaks occur at approximately the same distance. The peaks of the two curves for the strongest potential, i.e., the two leftmost curves of panel (a), start to decrease in amplitude with growing ϵ, which we attribute to the onset of a significant amount of backscattering. This figure has been taken by Ref. [22]

For $\alpha = 1$ we obtain the original LL index, while for $\alpha = 0$ we have a flat refractive index $n = 1$.

For the simulations, we use a random network consisting of 150 randomly located LLs each with radius $R = 10\lambda$; λ is the wavelength of the EM wave, used as normalized unit of length. The size of the disordered rectangular lattice is $460\lambda \times 360\lambda$ with constant filling factor $f = 0.28$. Furthermore, we use periodic boundary conditions at the up and down edges and absorbing boundary condition at the end.

The intensity of the electric field component of the EM wave simulations through the random LLs networks for two different values of strength parameter α is presented in Fig.3.3. The randomly located LLs are illustrated by means of white lines; the lighter color denotes high intensity areas whereas the darker denotes lower values of intensity. Fig.3.3a shows the propagation for $\alpha = 0.07$ whereas Fig.3.3b indicates the propagation for $\alpha = 0.1$. Fig.3.4 shows the scintillation index σ_I^2, as it is given by equation (3.32), for several values of α (viz. several values of the potential standard deviation σ). In Fig.3.4 a we plot the σ_I^2 as a function of the propagation coordinate x, whereas in Fig.3.4c the same curves are illustrated in a rescaled x axis, i.e. $x \to x/\sigma^{-2/3}$. The maximum of σ_I^2 curves are plotted in the Fig.3.4b revealing that the theoretical finding of equation (3.30) holds as well for the propagation of EM waves through a random and weak scattering medium.

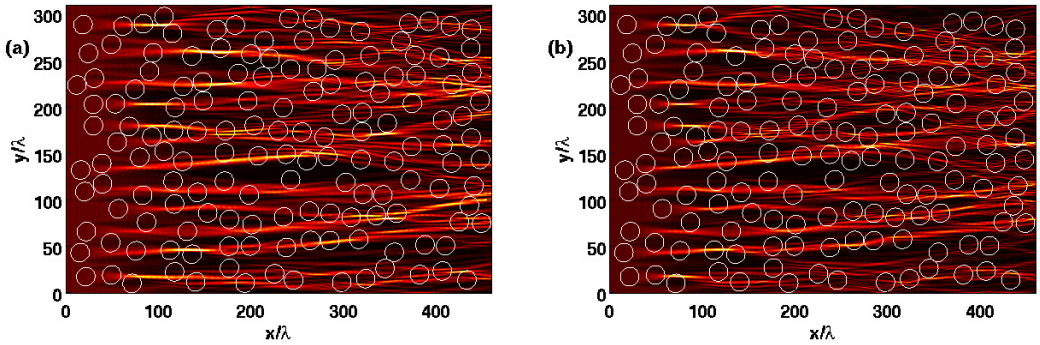

Figure 3.3: White lines denote the arrangement of Luneburg lenses. Monochromatic EM plane waves propagate through a disordered transparent media consists of generalized LLs with index of refraction given by (3.34).The intensity of electric field is denoted by lighter color for high intensity and by darker color for lower intensity. In (a), the strength parameter is $\alpha = 0.07$ while in (b) $\alpha = 0.1$. In both images the branching flow is evident.

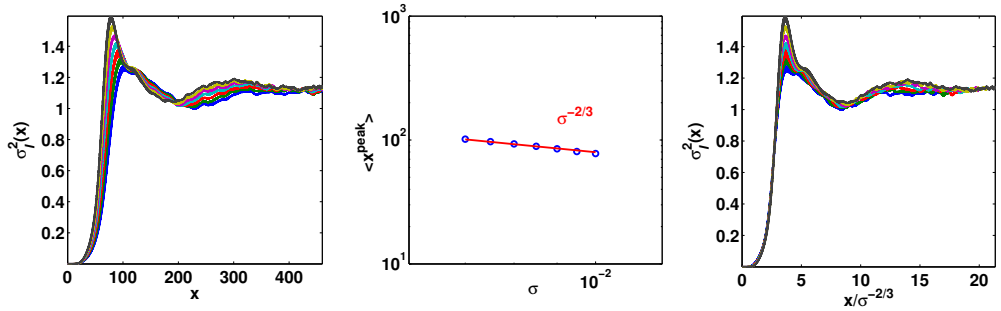

Figure 3.4: Scaling of the branching length with respect to the standard deviation of the random potential σ. (a) Scintillation index $\sigma_I^2(x)$ as function of the distance from the source, for different values of σ (b) maximum position of the scintillation curves obtained from σ_I^2; the curve shows a scaling of $\sigma^{-2/3}$ (red solid line) The scaling is confirmed in panel (c), where the curves from the left panel (Fig. a) are shown with a rescaled x axis, in which all peaks occur at approximately the same distance.

Chapter 4

Rogue wave formation through strong scattering random media

Rogue waves (RWs) or freak waves, have for long triggered the interest of scientists because of their intriguing properties. They are extreme coherent waves with huge magnitude which appear suddenly from nowhere and disappear equally fast. RWs were first documented in relatively calm water in the open seas [15, 36] but recent works have demonstrated that rogue wave-type extreme events may appear in various physical systems such as microwaves, nonlinear crystals, cold atoms and Bose-Einstein condensates, as well as in non-physical systems such as financial systems [22–24, 27, 29, 37–40].

RW pattern formation emerges in a complex environment but it still unclear if their appearance is due to linear or nonlinear processes. Intuitively, one may link the onset of RW pattern formation to a resonant interaction of two or more solitary waves that may appear in the medium; subsequently it has been tacitly assumed that extreme waves are due to nonlinearity [24, 29, 38, 40–42]. However, large amplitude events may also appear in a purely linear regime [15, 22, 23, 27, 36]; a typical example is the generation of caustic surfaces in the linear wave propagation as it was discussed in Chapter 3.

In this Chapter we investigate optical wave propagation in a strongly scattering optical media that comprising Luneburg-type lenses, randomly embedded in the bulk of transparent glasses. In particular, we use a type of lenses, namely Luneburg Holes (LH) (or anti-Luneburg lenses) instead of the original LLs, with refractive index profile given by equation (4.1) [27] and with ray tracing solution of equation (4.2), which is obtained by solving the ray differential equation (1.38) for LH refractive index function (4.1). In contrast to an LL, LH has a purely defocussing property as it is illustrated in Fig.4.1. The maximum difference of the refractive index for LL as well as for LH, compared to the background, is very large, viz. of the order of 40% and

thus a medium with a random distribution of LHs can be characterized as a strongly scattering random media. We are using this kind of lenses instead of original LLs, because they are easier to be fabricated in the bulk of a dielectric, such as a glass [27].

$$n(r) = \sqrt{1 + \left(\frac{r}{R}\right)^2} \tag{4.1}$$

$$\vec{r}(t) = \vec{r}_0 \cosh\left(\frac{c}{R}t\right) + \vec{k}_0 \frac{R}{c} \sinh\left(\frac{c}{R}t\right) \tag{4.2}$$

where $\vec{r} = (x, y)$ and $\vec{k} = (k_x, k_y)$.

By analysing the EM wave propagation in the linear regime we observe the appearance of RWs that depend solely on the scattering properties of the medium. Interestingly, the addition of weak nonlinearity does not modify neither the RW statistics nor the position where a linear RW appears [27]. Numerical simulations have been performed using the FDTD method, as it was discussed in Section 1.4, proving that optical rogue waves are generated through linear strong scattering complex environments. Finally we give some experimental results which confirm the validity of our theoretical predictions.

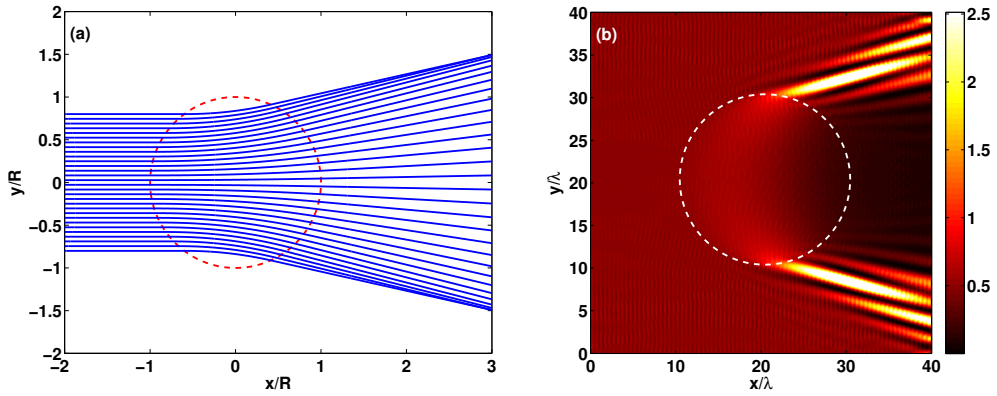

Figure 4.1: The red dashed line in (a) and the white line in (b) denote a Luneburg hole (LH) lens with refractive index profile given by equation (4.1). In (a) an exact solution is represented, based on equation (4.2), for ray tracing propagation with plane wave initial conditions, while in (b) we present FDTD simulation results of monochromatic EM plane wave propagation through a single LH. Both of images reveal the purely defocussing properties of LH.

4.1 Rogue waves in optics

As it has been already mentioned, RWs are extreme coherent waves with huge magnitude; a more precise definition of RWs specifies that the height or the intensity of a RW has to be at least two times larger than the significant wave height (SWH) H_s, where the latter is defined as the mean wave height of the highest (statistical) third of the waves [15, 27, 36].

Another way to investigate RWs is by means of the distribution of wave heights or intensities. According to the central limit theorem and the simple random wave prediction for the probability distribution of wave intensities I, the intensities have to follow the Rayleigh law, obeying a distribution of $P(I) = e^{-I}$, where $I = |E|^2$ (E is the electric field), normalized to one. However, when extreme events appear, the intensities distribution deviates from the simple exponential resulting to long tails appearance, due to the presence of very high intensities [15, 23, 27, 36].

In the following, we present FDTD numerical simulations for EM wave propagation through a media which consists of random located LHs. Each LH lens, with refractive index given by equation (4.1), has radius $R = 3.5\lambda$, where λ is the wavelength of the EM wave. The bulk medium has dimensions (175.0×528.5) in (λ^2 units) and refractive index $n = \sqrt{2}$; 400 LH lenses are placed randomly in the dielectric (bulk medium) with fixed filling factor $f = 0.17$; absorbing boundary conditions have been applied.

In Fig.4.2 we present the numerical results based on the FDTD method for the linear medium. In Fig.4.2a and in Fig.4.2b, we present the propagation of a monochromatic EM plane wave through the random LH network. We observe that the presence of scatterers with strong defocussing properties, forces light to form propagation channels (Fig.4.2a) that can lead to the generation of very large amplitude rogue type waves (Fig.4.2b). In Fig.4.2c, the random LH network which is used for FDTD simulation of Figs.4.2a and 4.2b, is represented. Fig.4.2d shows the intensity profile where a linear RW occurs; as can been noticed, the highest pick is larger than twice the SWH resulting in a RW. Fig.4.2e presents, in semilog axis, the distribution of electric intensities (blue dots) and the Rayleigh distribution (dashed black line). As we can see, the distribution of intensities deviates from the Rayleigh curve resulting in an extreme event signature.

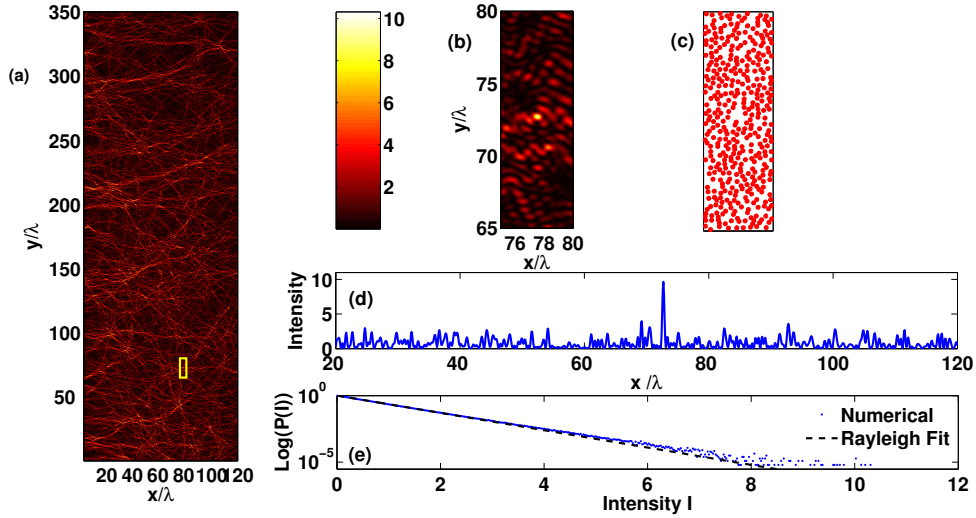

Figure 4.2: (a) A monochromatic plane wave beam propagates, from left to right, through the LH lattice. (b) A detail of the propagation (yellow box in (a)) showing an optical RW. (c) A 2D random LHs network used in the simulations; each red circle represents a LH. (d) Intensity profile in the RW region as a function of x. (e) Intensities distribution (in semilog scaling) for the entire lattice.

Further up, we introduce a focusing nonlinearity (Kerr effect) in the dielectric function reading $\varepsilon = n^2 = \varepsilon_L + \chi|E|^2$, where E is the electric field, ε_L the linear part pf the permittivity and χ the nonlinear parameter varying from 10^{-7} to 10^{-6} (depending on the strength of the nonlinearity; in normalized values). As it has mentioned, we can see that the linear observed RW statistics of Figs.4.3(a,c) are not affected in the presence of a relatively small nonlinearity (Figs.4.3(b,d)). In this case most waves are simply amplified without destroying the RW statistics but slightly increasing the queue of the intensity distribution Fig.4.3d as expected from the higher amplitudes.

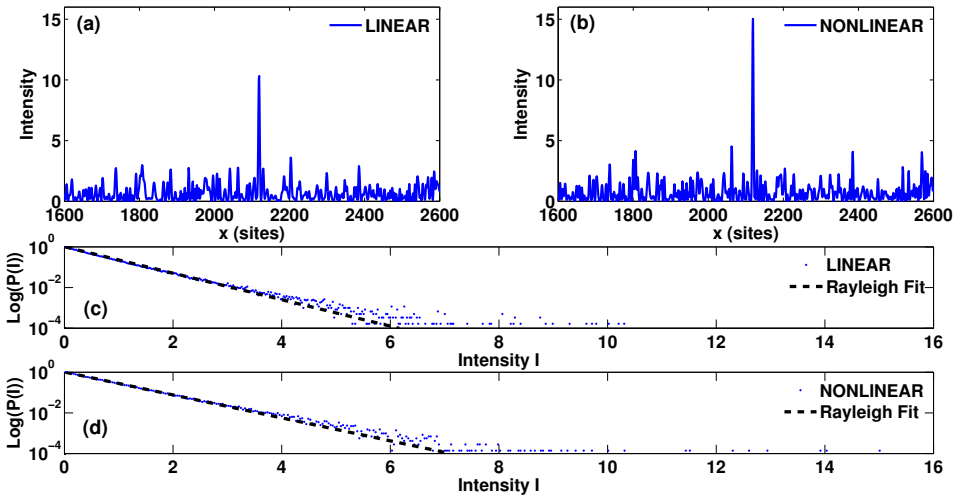

Figure 4.3: Simulations on the role of the nonlinearity. (a) An intensity profile in the linear regime of a region presenting a RW surrounded by low amplitude waves, (b) the same region in the nonlinear regime (at the limit of the critical power) showing an increase of the amplitude of the related waves maintaining though a clear RW picture. (c-d) Intensity distributions in the linear and nonlinear cases respectively, showing similar RW statistics with a slight change of the slope in the nonlinear case as expected by the higher wave amplitudes.

4.2 Experimental results

In this Section, we present experimental results which have performed by collaborators Tzortzakis and Pitsios and are taken by Ref. [27].

Focusing tightly a femtosecond IR beam into the bulk of fused silica substrates induces nonlinear absorption allowing the selective modification of the material [43]. Under appropriate irradiation conditions one may create LH-type structures and by placing those in a controlled way in space to create three dimensional LH lattices like the ones shown in Fig.4.4a.

The investigation for the presence of a rogue wave is performed by probing a laser beam through the volume of the lattice and imaging the output. This approach is advantageous because it allows the study of both linear and non-linear phenomena, depending only on the probe beam intensity.

For the linear observations a low power continuous wave 633 nm laser beam was used as probe. A large number of different lattices were studied until "rogue" events were observed as seen in Fig.4.4b. The corresponding "rogue" event intensities profile is shown in Fig.4.4c and the distribution of

the intensities, in semilog scaling, in Fig.4.4d and permit to conclude that this signal cannot be anything else than an optical rogue wave, contiguous to the definition of the phenomenon [15, 23, 27, 36].

An obvious question arises as of the role of nonlinearity in the same processes. For answering this question experimentally we increased the intensity of the probing radiation (using high power femtosecond pulses) exciting thus nonlinear modes through Kerr nonlinearity. In Fig.4.5 one can observe the total beam, Kerr-induced, self-focusing in the bulk of a glass without any lattice inscribed in it as the input beam power is increased from (a) to (d). On the contrary when the same intense beam goes through a glass with a lattice inscribed in it things are considerably different. At the limit of small nonlinearity, around the critical power, although an amplification of the waves already existing in the linear regime is observed, the linear RW statistics are not modified. This is shown in Fig.4.6(a) where linear RWs are further amplified maintaining though their intensity aspect ratio compared to the neighboring lower level waves. As the input power is increased gradually also the low level waves are amplified as well resulting to a small amplitude multi-filamentation image, Fig.4.6(b). Further increase in the input beam power, and thus higher nonlinearity, results to the saturation of the intensity of all modes, starting from the higher to the lower ones, since higher order -defocusing- nonlinearities lead to intensity clamping [44]. This is shown in Fig.4.6(c) where a higher input laser power pushes many small waves up to the clamping intensity. From the above it is clear that the generation of RWs in the strongly scattering system is a result of linear interference mechanisms while nonlinearity will either accentuate the phenomenon, when it is relatively small, or completely destroy the RW statistics when it is high. An interesting report at the filamentation and intensity clamping regime discussing filamentation merging and RW events has appeared recently [45].

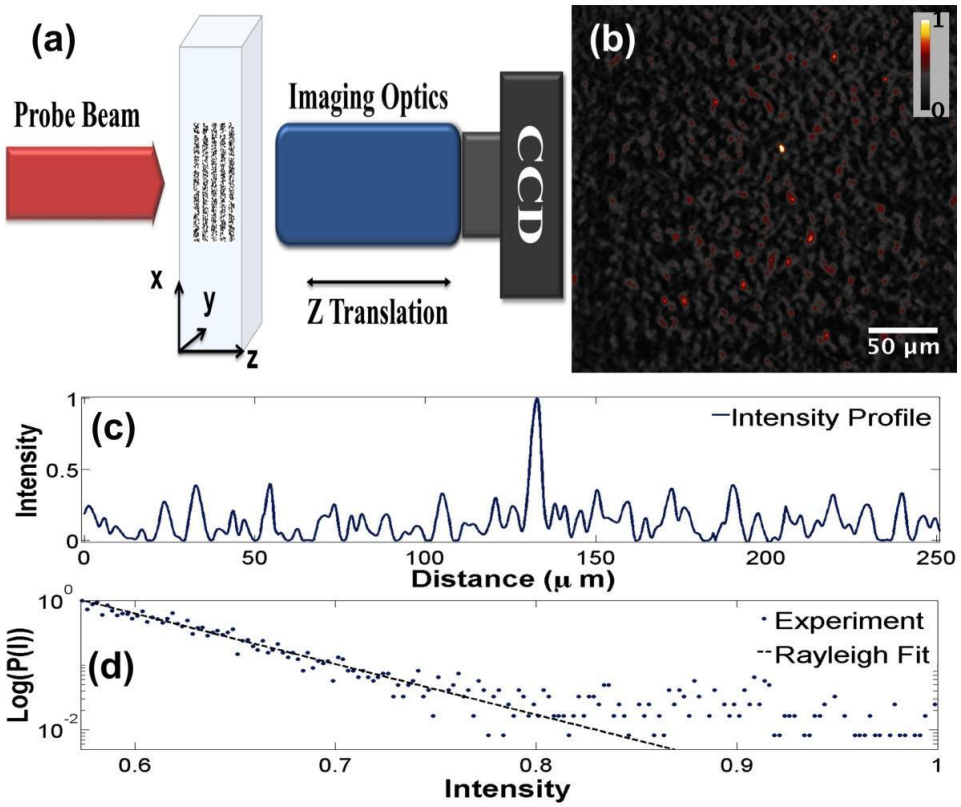

Figure 4.4: Experiments: (a) Schematic representation of the experimental setup. A monochromatic coherent plane wave laser beam propagates from the left to right (red arrow) in the glass sample where a five layer random LHs lattice is inscribed. An imaging system allows recording the beam profile at various propagation planes. (b) Experimental observation of an optical rogue wave as it is formed within the LHs lattice (appearing at the 4^{th} layer; almost at the center of the image). The RW is clearly distinct as its intensity is significantly greater from every other wave in the surrounding area in the lattice as seen also at the corresponding intensity profile (c). (d) Intensities distribution (in semilog scaling); rogue waves presence introduces a substantial deviation from the exponential distribution (Rayleigh law) appearing as a tail at high intensities.

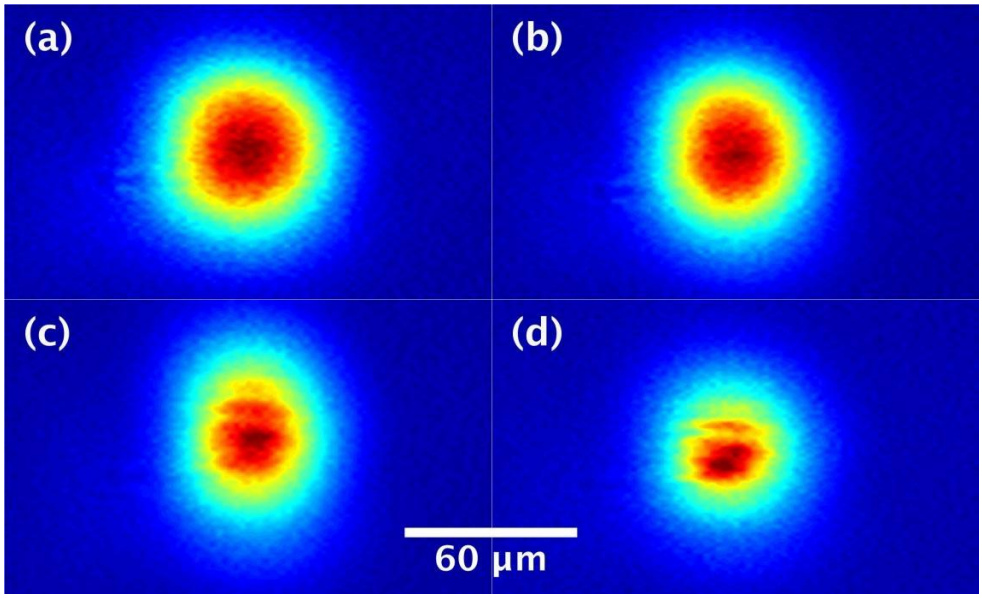

Figure 4.5: Experimental results on the nonlinear propagation of an intense femtosecond probe beam in the bulk of a glass without any lattice. The total beam Kerr self-focusing can be clearly seen as the input laser power is increased from (a) to (d).

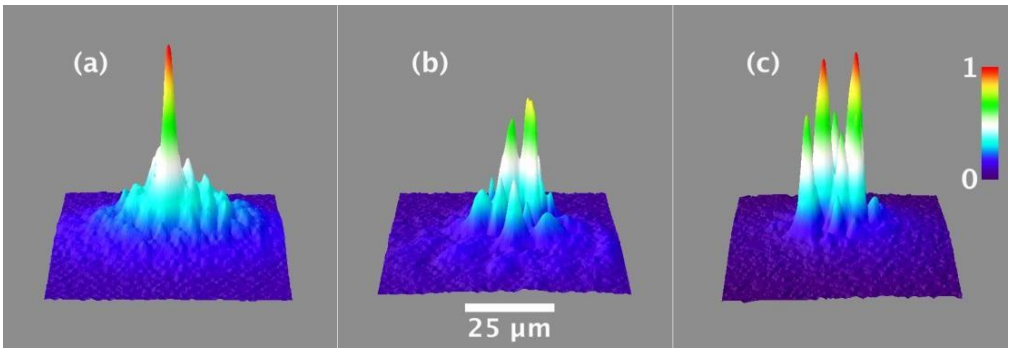

Figure 4.6: Experimental results on the nonlinear propagation of an intense femtosecond probe beam in the bulk of a glass with a LHs lattice inscribed in it. (a) Under the effect of Kerr self-focusing at the limit of the critical power a linear RW is further amplified maintaining its contrast from the surrounding waves. (b) As the input power and nonlinearities are increased one can observe the appearance of small scale multifilaments. (c) At even higher input powers the multifilaments shown in (b) reach the clamping intensity (red peaks) and thus the RW statistics are destroyed.

Chapter 5

Optical fiber lattices

Small world networks have attracted great interest in the last decades due to the very broad applicability to real-life problems ranging from social networks, to physics, chemistry and biology [46–51]. Some of the unique properties that arise in the small-world regime are robustness (high clustering coefficient), combined with efficient transport properties (low average path length) [52–54]. Quantum dynamics simulations on scale free networks indicate a phase transition in the transport properties as one approaches the thermodynamic limit [54–56]. Even though small-world networks have been extensively studied focusing on diffusive properties and using a classical statistical description, wave-like propagation properties have not attracted considerable attention yet. In this Chapter, the small-world concept is applied to an optical or equivalently to a quantum mechanical system. In particular we model an optical fiber lattice that exhibits small-world network topology. The transport properties of this network are investigated and compared with those of an ordered as well as a uniformly random network. The dynamics of the system are governed by the amount of structural disorder present in the network [18].

Experimental investigations of disordered optical lattices indicate that a small amount of disorder is sufficient to lead to Anderson localization [16, 17, 57–59]. In this case the excited wavepacket does not disperse but instead remains partially localized due to the dielectric index disorder in the medium. A different source for localization is nonlinearity: when the interaction of the wavepacket with the medium is highly non-linear it can lead to self-trapping [60, 61]. For example, when a laser pulse interacts with a highly responsive medium, it can lead to self focusing and soliton formation [6, 62, 63]. Self-trapping is known to occur abruptly at a threshold which depends on the system properties such as size and geometry [64–68].

In the present Chapter of this Thesis we investigate primarily the impact

of structural disorder on the wavepacket dynamics on a 2D lattice. The specific form of disorder used leads to the formation of a small world network lattice that is parametrized through a randomness parameter. Additionally, we observe the effects that nonlinearity may induce, viz. that nonlinearity rapidly leads to self-trapping, while structural disorder acts like a barrier creating channels in which transport is favoured, leading to anomalous diffusion [18]. Previous investigations on optical random media indicate that nonlinearity can emerge from structural disorder in the form of branched wave patterns [69]. In the current investigation we essentially disentangle these two parameters and explore the possibility of tuning independently localization due to structural disorder and due to self-trapping [18].

5.1 The small-world lattice

The physical system we are addressing consists of a lattice or network of optical fibers that permits light propagation along the fibers plus some interfiber interaction due to evanescent coupling. In Fig.5.1, we show an ordered square lattice, where the points correspond to the optical fibers position on the x-y plane. The fibers extend along the z direction, which in a paraxial approximation corresponds to time [70]. Initially, one of the fibers is excited and by measuring the intensity profile of the lattice for different cuts along the z-axis, one acquires the dynamics of the excited wavepacket on the lattice.

Starting from an ordered lattice, structural disorder is inserted to the system by applying a Monte-Carlo criterion. A disorder parameter ρ is introduced, which is the probability of moving a single point of the lattice to a new position. Sampling the whole lattice, the points are repositioned by decision (whether a random check between 0 and 1 is larger that ρ) to a new random position in the plane. The case $\rho = 0$ is the fully ordered case, while for $\rho = 1$ all the points have been repositioned at arbitrary positions yielding a uniform random network. In the intermediate regime $0 < \rho < 1$ the lattice is partially disordered; we will show that a small amount of structural disorder is sufficient for the emergence of the small-world properties.

We can construct a network out of a 2D lattice by assigning the fibers as the network nodes while the interaction between the optical fibers are the edges. This treatment yields a weighted network [71], where the weight of the edges depends on the distance between the points on the 2D plane in the following way:

$$w_{ij} = A \cdot e^{-(r_{ij} - r_0)} \tag{5.1}$$

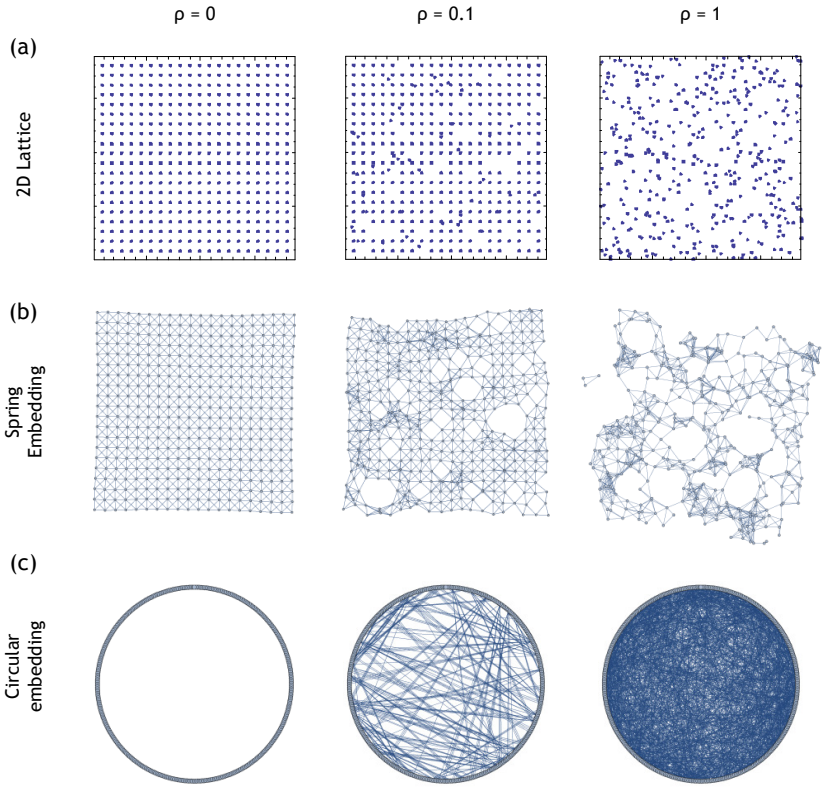

Figure 5.1: (a)The 2D lattice of the optical fiber position for different values of the structural disorder parameter ρ. The corresponding network configurations in the (b)spring and (c)circular embedding.

where w_{ij} is the weigth that links any two fibers labeled i and j respectively, r_{ij} is the distance between these fibers, r_0 a characteristic lenght scale and A is weight amplitude [18]. This form of edges models reasonably well the fiber crosstalk, i.e. the tunneling probability between fibers. In Fig.5.1b we show the networks that arise from the 2D lattices for the cases where $\rho = 0$, $\rho = 0.1$ and $\rho = 1$. To facilitate comparison between the three networks the edges are shown only above a certain weight (0.01%). The algorithm used to optimize the network topology is the spring embedding, which assumes a ball-string relationship between the nodes of the system.

In the ordered case ($\rho = 0$) the network is a 2D manifold corresponding precisely to the 2D lattice. For a small amount of structural disorder ($\rho = 0.1$) a few nodes have been repositioned, creating holes on the one hand

and patches of increased density on the other. This treatment leads to the formation of local clusters, making some of the nodes of the network highly connected and others more disconnected. This is the key feature of the network, which as we will see has an significant impact on the dynamics. In the fully random case ($\rho = 1$) the network has been essentially fractured to smaller fractions, which are very weakly connected among them. The exact value that the network passes to the fractured regime relates to the site and bond percolation threshold of the network [72, 73].

A more common network graphical representation is the circular embedding, shown in Fig.5.1c. The nodes are placed on a circle and the corresponding edges are drawn between them. Then instead of repositioning the nodes like in the real 2D lattice and in the spring embedding, they are kept in fixed positions and instead the edges are redirected. From this point of view ρ can also be understood as the network rewiring probability. It has been shown that by following this procedure small-world properties arise at very small ρ's [52]. Using this approach we can analyse the disordered 2D lattice as a weighted network. This method allows us to make a direct connection between the lattice transport properties and the network topology and simplify the simulations by mapping the 2D lattice plane to a reduced adjacency matrix.

To quantify the structural local change of the lattice as a function of increasing structural disorder, we calculate the correlation length for different ρ's. This can be achieved by calculating the standard deviation of the correlation function of the disordered network, which is normalized with respect to the ordered lattice. In order to have a statistically good ensemble, we make 50 realizations for 500 different steps of the disorder parameter ρ. The resulting correlation length decays rapidly as a function of the disorder parameter, as can be seen in Fig.5.2. To extract consistently a single value for the correlation length decay, we fit with a single exponential function (red curve) yielding $\rho_l = 0.28$. As we discuss also below this value signals the regime between ordered and random network [18]; this feature emerges in both the structural and dynamical aspects of the system. The corresponding offset of 0.26, observed for larger values of the disorder parameter is due to the finite system size (400 points).

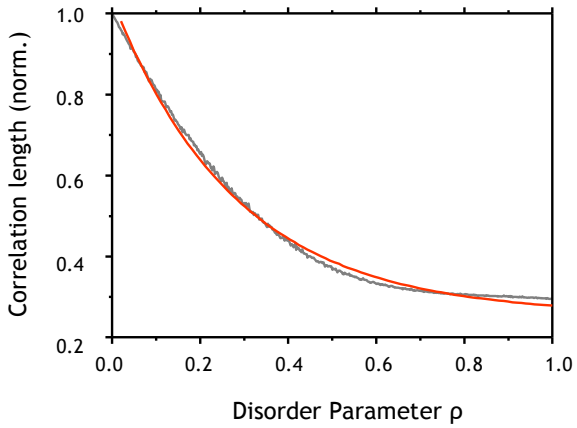

Figure 5.2: The correlation length of the network as a function of the disorder parameter ρ. A exponential fit (red line) yields a characteristic $\rho_l = 0.28$.

5.2 Dynamics of electromagnetic wavepacket propagation

To simulate the dynamics of the excited wavepacket on the 2D lattice use the discrete nonlinear Schrödinger equation (DNLS) [64, 66, 67, 74]:

$$i\frac{d\psi_n}{dt} = \sum_m V_{n,m}\psi_m - \chi|\psi_n|^2\psi_n \tag{5.2}$$

where V is the network adjacency matrix, which contains the weights between the vertices. The second term introduces anharmonicity with the nonlinearity parameter χ. The DNLS equation is an ideal choise to depict the evolution, because it can describe realistically the tunneling of a wavepacket through optic fibers and allows one to explore the influence of nonlinearity on the dynamics. The resulting dynamics are displayed on Fig.5.4, where the color values indicate the amplitude of wavepacket between 0 (blue) and 1 (white) [18]. Initially the wavepacket is placed in the central lattice site; in an experiment, this initial condition corresponds to the excitation of a single fiber. In the vertical sections we show selections of snapshots from the evolution of the wavepacket, while on the right hand side we portray the wavepacket mean square displacement (MSD) as a function of time. In the ordered lattice with no nonlinearity (Fig.5.4a), where $\rho = 0$ and $\chi = 0$ the wavepacket spreads ballistically. This is quantified through the function

$f(t) = Dt^{\alpha}$ where D is the diffusion coefficient and α the diffusion exponent. In the ballistic case, the fit yields $\alpha = 2$ (blue line). We note that these results correspond to finite system behaviour that stop every time light reached the edge fibers due to diffraction.

We also examine the influence of nonlinearity in the ordered lattice (Fig.5.4b). As expected from previous investigations [64, 66–68], self-trapping of the wavepacket occurs abruptly above a certain value of the nonlinearity parameter χ. This is characteristically depicted on the dynamics, as can be seen from the snapshots for $\chi = 10$. Even though the wavepacket initially spreads (t=1), due to the intense self-interaction introduced by the nonlinear term it is then trapped to the initial site (t=3). Additionally, a small fraction of the wavepacket spreads through the rest of the lattice. The MSD of the wavepacket is shown for different values of the nonlinear parameter ($\chi = 0, .., 10$) on the right hand panel [18].

One can see that the wavepacket exhibits ballistic behaviour for smaller values of the nonlinearity parameter, whereas a rapid change of behaviour occurs for greater χ's. This feature becomes clear when plotting the fitted diffusion coefficients α as a function of the nonlinearity parameter (Fig.5.3). When increasing nonlinearity, the system changes from ballistic behaviour to partial delocalization and finally to self trapping. A sigmoidal function fit (stretched exponential - red line) yields the characteristic value of $\chi_c = 7.5$, which signifies the passing to the self-trapped regime. This feature has been studied extensively in previous investigations, where it was shown that the value χ critically depends on the system size and geometry [64–68]. Here, we see that this property also holds for the 2D lattice and additionally discover that a small fraction of the wavepacket is not trapped. In the simulations we use open boundary conditions; we verified that implementing periodic boundary conditions does not significantly alter our results and simply shifts the critical nonlinearity value χ_c as shown in 1D networks [64], since we essentially limit our studies on the early wavepacket dynamics, where the probability amplitude is nearly zero near the boundaries. Furthermore, similar effects are observed for the system size: self-trapping is known to depend critically on system size [64], which again can shift in our system the critical nonlinearity χ_c in an analogous way to the 1D system.

An alternative way to localize the excitation is by incorporating disorder, which has been previously observed theoretically and experimentally in optical lattices [16, 17, 57–59]. Using the procedure described in Fig.5.1, structural disorder is introduced to the system and the dynamics is examined in the regime in between an ordered lattice and a completely random one. In Fig.5.4c we show snapshots from the dynamics in a lattice with disorder parameter $\rho = 0.3$. Naturally, structural disorder acts like a barrier, slowing

down dramatically all dynamics while creating new channels of transport as can be seen clearly in the latter snapshots ($t = 10^5$). As a result the diffusion coefficient decreases, in this case to $\alpha = 1.14$ (the traces shown in the disordered cases are averaged over 50 different lattices). For a completely random lattice (Fig.5.4d - $\rho = 1$) we observe that the wavepacket remains localized within the observed timescales and exhibits sub-diffusion with corresponding diffusion coefficient $\alpha = 0.29$. This behaviour is quantified in Fig.5.5, where is shown the diffusion coefficient α as a function of the disorder parameter ρ. We consider this as the main result of the paper: the system passes from normal diffusion to sub-diffusion with increasing structural disorder, even though nonlinearity is absent. A characteristic value of $\rho_c = 0.22$ is extracted from the fit (stretched exponential - red line), which signifies the passage to sub-diffusive behaviour [18]. The residual offset ($\alpha_0 = 0.23$) is due to trapping of the wavepacket in the initial position, which exhibits Anderson-like localization. The transition to sub-diffusion signifies the passage from an ordered network to a small-world regime. Finally including a combination of both nonlinearity and structural disorder leads to very strong localization ($\alpha = 0.18$) as shown in Fig.4e for the corresponding critical values ρ_c and γ_c [18].

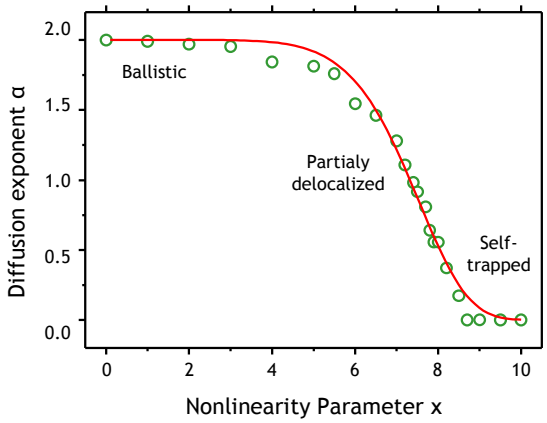

Figure 5.3: The diffusion coefficient α as a function of the nonlinearity parameter χ. For small χ's the system exhibits ballistic behaviour, whereas for larger ones ($\chi_c = 7.5$) the wavepacket remains partially localized and finally becomes self-trapped.

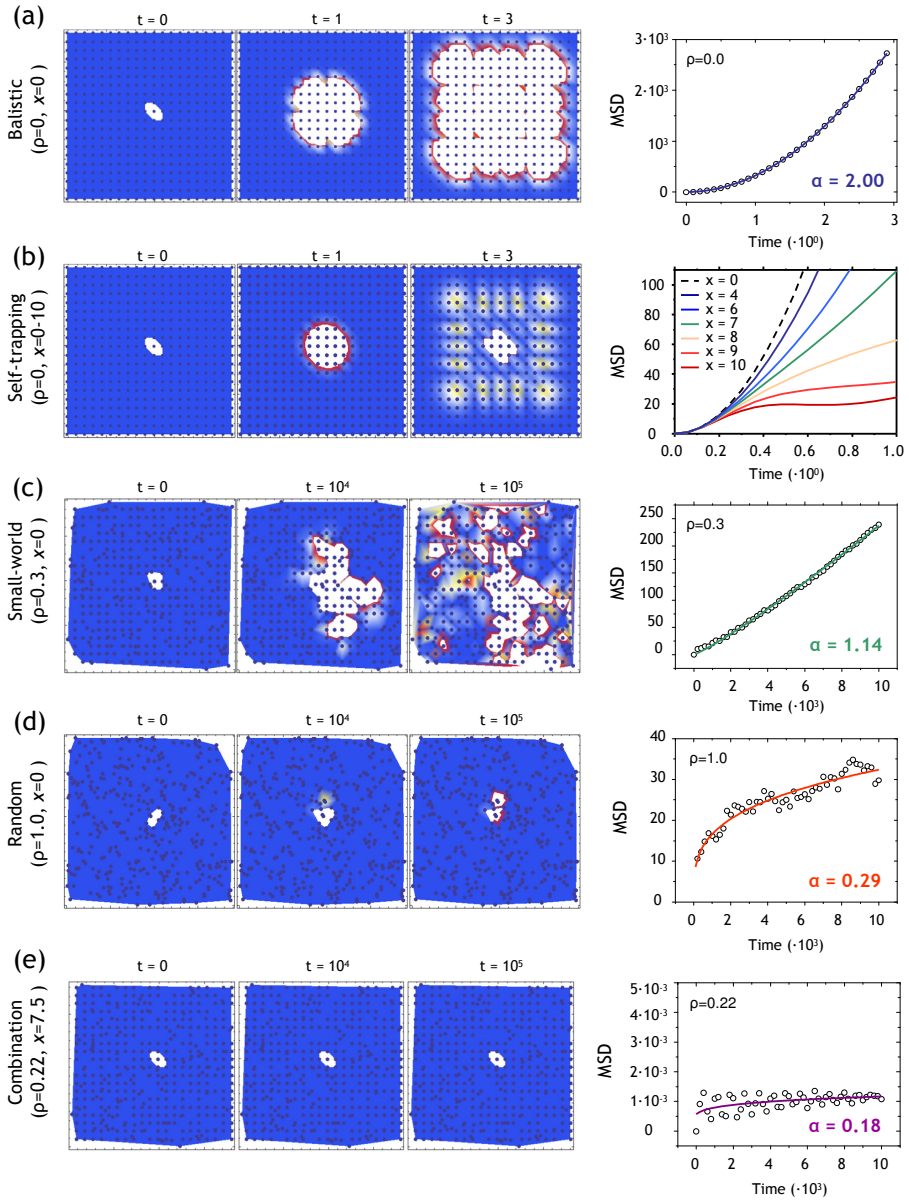

Figure 5.4: The dynamics of the wavepacket and the corresponding mean–square–displacement (MSD) as a function of time. (a) The linear case in the ordered lattice. (b) Nonlinearity induces self–trapping in the ordered lattice. In presence of structural disorder, the system passes from normal diffusion (c) to sub–diffusion (d). Finally the combination of nonlinearity and disorder leads to strong localization (e).

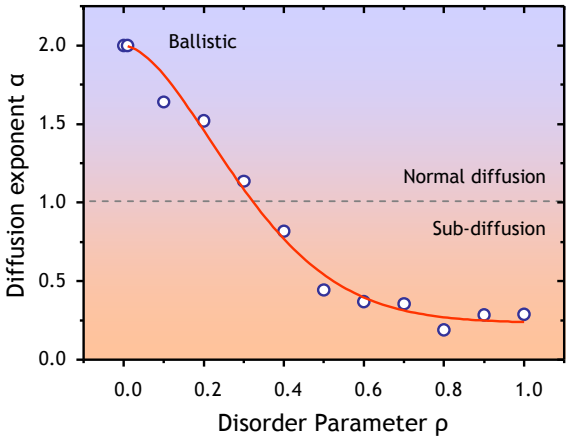

Figure 5.5: The diffusion coefficient α as a function of the disorder parameter ρ. For small ρ's the system exhibits normal diffusion, whereas for larger ones ($\rho_c = 0.22$) it switches to sub-diffusion.

5.3 Discussion

In the present Chapter is discussed a simple model describing the dynamics of a wavepacket in an 2D lattice, in the presence of structural disorder and nonlinearity. In a numerical experiment, the 2D lattice can refer to the tips of an optic fiber network; the dynamics examined refer to the excitation of one fiber and recording the intensity of the surrounding ones.

In an ordered lattice with no nonlinearity, we observe, as expected, that the system exhibits ballistic behaviour. Non-linearity is introduced through the DNLS equation, which lead to self-trapping for values larger than $\chi_c = 7.5$. On the other hand, structural disorder is introduced to the system by mapping the 2D lattice to a network, and repositioning the nodes with a Monte-Carlo criterion and probability ρ. As structural disorder increases, we observe a transition with regard both the structural and dynamical properties of the system at about $\rho = 0.25$. The correlation length decreases rapidly ($\rho_l = 0.28$) and a passage is noted from normal diffusion to sub-diffusion ($\rho_c = 0.22$). From the network analysis this result is understood as a signature of the small-world regime: strongly connected local clusters are created, which are weakly connected among them, and therefore channels of preferential transport arise, leading to sub-diffusion.

Numerical results indicate that the combination of structural disorder with nonlinearity leads to almost complete localization of the wavepacket, for values bellow the self-trapping threshold ($\chi_c = 7.5$), which is in agree-

ment with previous investigations [67, 68]. It would be very illuminating to perform the experiments discussed here and actually see whether one can control diffusion through the lattice geometry (disorder) and laser intensity (nonlinearity), and probe experimentally the small-world regime. Additionally, it would be interesting to extend the same line of investigation to different complex network topologies, such as the apollonian networks, in which is known that one can observe quantum phase transitions of light [54–56].

Chapter 6

Active plasmonic systems

In this Chapter we present a well known light-matter interaction effect called surface plasmon polaritons (SPPs). SPPs are electromagnetic excitations propagating at a interface between a dielectric and a metal, evanescent confined in the perpendicular direction. At optical frequencies, the metal's free electrons can sustain, under certain conditions, oscillations; the SPPs can arise via the coupling of this electron oscillation with an electromagnetic field. Subsequently, the existence of plasmons is characteristic for the interaction of metals with light [75–79]. What makes the plasmons of current interest is their ability to confine light to nanoscale regions, i.e. much smaller that the wavelength of light, resulting to sub-wavelength optics.

In addition, many innovative concepts and applications of metal optics have been developed over the past few years. Two commonly used configurations for plasmon excitation are the Kretschmann - Raether and the Otto configurations. In the first, a thin metal film (40-70nm) is sandwiched between two dielectrics with different refractive indexes, with a incident EM wave hitting the denser dielectric. In the second, viz. Otto configuration, the denser dielectric and the metal sandwich the lighter medium. [75, 77–80]

In this Chapter we present the fundamentals of SPPs for a single flat interface. Taking as a starting point the wave equation derived by Maxwell's equations, we show that a dielectric-metal interface can support plasmon modes only excited by TM polarization EM wave. Additionally, we calculate the SPPs dispersion relation, the spatial profiles of the electric and magnetic fields as well as the propagation and penetration lengths. Furthermore, we discuss about the excitation of SPPs using the Kretschmann - Raether configuration and finally, we introduce active (gain) dielectrics, instead of passive dielectrics, and show analytically as well as numerically using COMSOL multiphysics software, how the dispersion relations is changed as well as the enhanced of the SPPs propagation length.

6.1 Surface plasmon polaritons

In order to investigate the physical properties of the SPPs, we apply the Maxwell equations to a flat interface between a metal (conductor) and a dielectric (insulator). As a starting point, we may use the time dependent wave equation for the electric field $\vec{E}$, derived by free charges and currents Maxwell equations, that is

$$\left[\nabla^2 - \frac{\varepsilon}{c^2}\frac{\partial^2}{\partial t^2}\right]\vec{E} = 0 \tag{6.1}$$

where we have assumed negligible variation of the dielectric permittivity profile $\varepsilon(\vec{r})$ over distances on the order of optical wavelength and c the light velocity in vacuum [75, 77].

We solve the equation (6.1) separately in regions of constant ε, viz. solve separately for metal and for dielectric, thereafter the obtained solutions have to been matched using appropriate boundary conditions [75]. Firstly, we assume a harmonic time dependence of the electric field, viz. $\vec{E}(\vec{r},t) = \vec{E}(\vec{r})e^{-i\omega t}$, as a result the equation (6.1) is modified to the Helmholtz equation (6.2)

$$\left[\nabla^2 + k_0^2\varepsilon\right]\vec{E}(\vec{r}) = 0 \tag{6.2}$$

where $k_0 = \omega/c$ is the wave vector of the EM propagating wave in vacuum.

We are working on a Cartesian orthocanonical system, where the interface between metal and dielectric is located at $z = 0$. In addition, we assume, for simplicity, an one dimensional problem, i.e. ε depends only on one spatial coordinate. Specifically, the waves propagate along the x-direction of the Cartesian system and show no variations in the perpendicular (in plane y-direction), as a result we have $\varepsilon = \varepsilon(z)$ [75]. The geometry that is described above, is illustrated in Fig.6.1

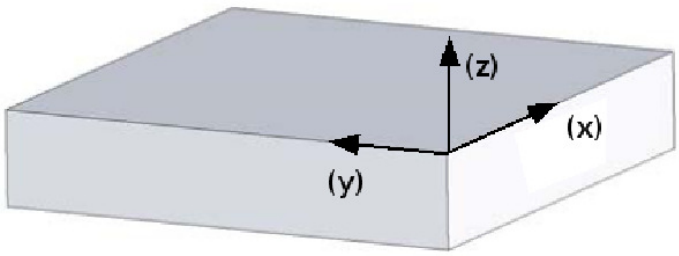

Figure 6.1: Definition of a planar waveguide geometry. The surface waves propagate along the x-direction in a Cartesian orthocanonical coordinate system.

Since we are interested only in surface waves, we apply our theory only to the interface, i.e. in the plane for $z = 0$. Subsequently, the propagating wave can be described as $\vec{E}(x, y, z) = \vec{E}(z)e^{i\beta x}$, where β is a complex parameter called *plasmon propagation constant* of travelling surface waves. Substituting this expression in the Helmholtz equation (6.2), yields to [75]

$$\frac{\partial^2 \vec{E}(z)}{\partial z^2} + \left(k_0^2\varepsilon - \beta^2\right)\vec{E}(z) = 0 \tag{6.3}$$

Naturally, a similar equation exists for the magnetic field $\vec{H}$ [75], namely

$$\frac{\partial^2 \vec{H}(z)}{\partial z^2} + \left(k_0^2\varepsilon - \beta^2\right)\vec{H}(z) = 0 \tag{6.4}$$

We are going to use the equations (6.3) and (6.4) for the general analysis of guided EM modes in waveguides. Since we are interested in spatial field profiles and dispersion relation of the propagating surface waves, we are going to use the curl Maxwell equations (1.42) and (1.43) together with the relation (1.45); In addition, we use also the following properties for the partial derivatives [75]

- Harmonic time dependence: $\frac{\partial}{\partial t} = -i\omega$
- Propagation along x-direction: $\frac{\partial}{\partial x} = i\beta$
- Homogeneity in y-direction: $\frac{\partial}{\partial y} = 0$

Subsequently, we obtain a close set of coupled differential equations for the components of the electric $\vec{E}$ and magnetic $\vec{H}$ fields, that is

$$\frac{\partial E_y}{\partial z} = -i\omega\mu_0 H_x \tag{6.5}$$

$$\frac{\partial E_x}{\partial z} - i\beta E_z = i\omega\mu_0 H_y \tag{6.6}$$

$$i\beta E_y = i\omega\mu_0 H_z \tag{6.7}$$

$$\frac{\partial H_y}{\partial z} = i\omega\varepsilon_0\varepsilon E_x \tag{6.8}$$

$$\frac{\partial H_x}{\partial z} - i\beta H_z = -i\omega\varepsilon_0\varepsilon E_y \tag{6.9}$$

$$i\beta H_y = -i\omega\varepsilon_0\varepsilon E_z \tag{6.10}$$

where ε_0 and μ_0 are the vacuum permittivity and permeability respectively.

Having the governing equations (6.5)-(6.10) at our disposal, we proceed to investigate separately two different EM waves polarizations, viz. the transverse magnetic (TM) and transverse electric (TE) modes. Furthermore, for

our analysis we use the simplest geometry sustaining SPPs, that is, a single flat interface, as Fig.6.2) indicates, between a dielectric and a conductive material (metal) with complex (in general) permittivities ε_d and ε_m respectively. The dielectric is located in the upper half space ($z > 0$) and the real part of its permittivity ε_d is positive ($Re[\varepsilon_d] > 0$), on the other hand the metal is located in the below half space ($z < 0$) and its permittivity ε_m has negative real part, viz. $Re[\varepsilon_m] < 0$. As we mentioned, we are interested in surface waves, subsequently we want to find propagating waves solutions with evanescent decay behaviour in the perpendicular axis z. We are going to calculate wave solutions in dielectric and metal spaces separately, and afterwards we have to match the solutions at $z = 0$, since we are looking for surface waves at the interface. The matching boundaries conditions which are going to be used for matching the two solutions, are depended on the polarization of the incident EM waves, viz. TM or TE polarization.

Figure 6.2: Geometry of SPP propagation at a single interface between a metal and a dielectric.

6.1.1 Transverse electric (TE) polarization

First of all, we investigate TE mode EM waves. In this polarization, the propagating component of the electric field vanishes resulting to $\vec{E} = (0, E_y, 0)$, whereas for the magnetic field we have $\vec{H} = (H_x, 0, H_z)$. According this condition and after some calculations, the governing equations (6.5)-(6.10) are simplified to a coupled system of differential equation comprised by the following three equations

$$H_x = \frac{i}{\omega\mu_0}\frac{\partial E_y}{\partial z} \tag{6.11}$$

$$H_z = \frac{\beta}{\omega\mu_0}E_y \tag{6.12}$$

$$\frac{\partial^2 E_y}{\partial z^2} - (\beta^2 - k_0^2\varepsilon)E_y = 0 \tag{6.13}$$

Consider a flat interface between a dielectric and a metal, as illustrated in Fig.6.2, and surface waves travelling in x direction, viz. ($E(x, y, z) = E(z)e^{i\beta x}$); the equations (6.11) - (6.13) yield to the following solutions for the fields components in both half spaces ($z > 0$ and $z < 0$)

- Solutions in dielectric ($z > 0$ and $\varepsilon = \varepsilon_d$)

$$H_x = -A\frac{ik_d}{\omega\mu_0}e^{i\beta x}e^{-k_d z} \tag{6.14}$$

$$H_z = A\frac{\beta}{\omega\mu_0}e^{i\beta x}e^{-k_d z} \tag{6.15}$$

$$E_y = Ae^{i\beta x}e^{-k_d z} \tag{6.16}$$

- Solutions in metal ($z < 0$ and $\varepsilon = \varepsilon_m$)

$$H_x = B\frac{ik_m}{\omega\mu_0}e^{i\beta x}e^{k_m z} \tag{6.17}$$

$$H_z = B\frac{\beta}{\omega\mu_0}e^{i\beta x}e^{k_m z} \tag{6.18}$$

$$E_y = Be^{i\beta x}e^{k_m z} \tag{6.19}$$

where k_d, k_m the wavenumbers in dielectric and metal respectively given by the equations (6.20) and (6.21)

$$k_d^2 = \beta^2 - k_0^2\varepsilon_d \tag{6.20}$$

$$k_m^2 = \beta^2 - k_0^2\varepsilon_m \tag{6.21}$$

A and B are constants, which are going to be determined by applying the matching conditions, i.e. continuity of E_y and H_x at the interface ($z = 0$); subsequently, this requirement yields to the conditions

$$A = B \tag{6.22}$$

$$A(k_d + k_m) = 0 \tag{6.23}$$

According the constrain for evanescent surfaces waves, the real part of both wavenumbers k_d and k_m has to be positive, subsequently the condition (6.23) is satisfied only for $A = B = 0$. As a result, SPPs modes cannot be supported in TE polarization [75] since the equation (6.14)-(6.19) become zero.

6.1.2 Transverse magnetic (TM) polarization

We proceed with TM polarization EM waves, that is, the propagating component of the magnetic field vanishes i.e. $\vec{H} = (0, H_x, 0)$ and for the electric field we have $\vec{E} = (E_x, 0, E_z)$. Substituting this polarization condition to central equations (6.5)-(6.10) we obtain

$$E_x = -\frac{i}{\omega\varepsilon_0\varepsilon}\frac{\partial H_y}{\partial z} \tag{6.24}$$

$$E_z = -\frac{\beta}{\omega\varepsilon_0\varepsilon}H_y \tag{6.25}$$

$$\frac{\partial^2 H_y}{\partial z^2} - (\beta^2 - k_0^2\varepsilon)H_y = 0 \tag{6.26}$$

Consider again the flat interface between a dielectric and a metal as shown in Fig.6.2 and surface waves travelling in x direction ($E(x, y, z) = E(z)e^{i\beta x}$), the equations (6.24) - (6.26) yields to the following solutions for the fields components in both half spaces ($z > 0$ and $z < 0$)

- Solutions in dielectric ($z > 0$ and $\varepsilon = \varepsilon_d$)

$$E_x = A\frac{ik_d}{\omega\varepsilon_0\varepsilon}e^{i\beta x}e^{-k_d z} \tag{6.27}$$

$$E_z = A\frac{\beta}{\omega\varepsilon_0\varepsilon}e^{i\beta x}e^{-k_d z} \tag{6.28}$$

$$H_y = Ae^{i\beta x}e^{-k_d z} \tag{6.29}$$

- Solutions in metal ($z < 0$ and $\varepsilon = \varepsilon_m$)

$$E_x = -B\frac{ik_m}{\omega\varepsilon_0\varepsilon}e^{i\beta x}e^{k_m z} \tag{6.30}$$

$$E_z = -B\frac{\beta}{\omega\varepsilon_0\varepsilon}e^{i\beta x}e^{k_m z} \tag{6.31}$$

$$H_y = Be^{i\beta x}e^{k_m z} \tag{6.32}$$

where the wavenumbers k_d and k_m are given by the equations (6.20) and (6.21) respectively. The constants A and B will be determined by matching the solutions at the interface ($z = 0$) with the appropriate boundary conditions, viz. continuity of the magnetic component H_y and continuity of the electric flux density $D = \varepsilon_i E_z$, where $i = d, m$ for dielectric and metal respectively. Substituting these matching condition in the solutions (6.27)-(6.32) we obtain the relation

$$\frac{k_d}{k_m} = -\frac{\varepsilon_m}{\varepsilon_d} \tag{6.33}$$

In order to keep the evanescent behaviour in z direction, the real part of wavenumbers k_d and k_m has to be positive, that yields to the condition

$$\beta^2 > k_0^2 \varepsilon_i \qquad (\text{i} = \text{d, m}) \tag{6.34}$$

In addition, the condition of equation (6.33) states that SPPs exist only at interfaces between materials with opposite signs of real part of their permittivity, for instance between an insulator (dielectric) and a conductor (metal).

We proceed with the calculation of dispersion relation for SPPs propagating at the interface between the two half spaces of Fig.6.2. Combining the equations (6.20) and (6.21) with the condition (6.33) we obtain the dispersion relation for the SPP wavenumber β, that is [75, 77, 79]

$$\beta = k_0 \sqrt{\frac{\varepsilon_d \varepsilon_m}{\varepsilon_d + \varepsilon_m}} \tag{6.35}$$

where $k_0 = \omega/c$ the light wavenumber in vacuum. In addition, we can also define the SPPs effective refractive index n_{sp}

$$n_{sp} = \frac{\beta}{k_0} = \sqrt{\frac{\varepsilon_d \varepsilon_m}{\varepsilon_d + \varepsilon_m}} \tag{6.36}$$

as well as the SPPs wavelength λ_{sp}, that is

$$\lambda_{sp} = n_{sp} \lambda_0 = \lambda_0 \sqrt{\frac{\varepsilon_d \varepsilon_m}{\varepsilon_d + \varepsilon_m}} \tag{6.37}$$

Note that the expressions (6.35) - (6.37) hold either for real or for complex permittivities ε_d and ε_m, where the imaginary part in the permittivity accounts either for losses or gain of SPPs energy.

6.2 Characteristics of surface plasmon polaritons (SPPs)

The basic characteristics of SPPs are the dispersion relation β of equation (6.35), the propagation length L and the penetration length t_d; in this Section, we analyse and discuss those characteristics. Since we are dealing with metals, we need a permittivity function for them; we use the Drude-Sommerfeld theory (or Drude model) for metals [75, 79], according with we obtain the following frequency dependent permittivity function for metals

$$\varepsilon_m(\omega) = \varepsilon_h - \frac{\omega_p^2}{\omega^2 - i\omega\Gamma} \tag{6.38}$$

where ε_h is a dimensionless variable showing the relative permittivity at infinite frequency, ω_p is the plasma frequency corresponds to the electrostatic electrons oscillation frequency, Γ is measured in frequency units and denotes the collision frequency which accounts for metal losses and ω the angular frequency of the incident EM wave. The first three variables (ε_h, Γ, ω_p) are constants for a given metal. In the following analysis, we use silica glass as an insulator and silver as a conductor, with parameters given by the Table 6.1

Table 6.1: Values of parameters for disperdion relation diagram.

Parameter	Value
ε_d	1.69
Γ	$1.018 \cdot 10^{14}\ rad/sec$
ω_p	$1.367 \cdot 10^{16}\ rad/sec$
ε_h	9.84

Substituting the metal's permittivity given by the Drude model of equation (6.38) with the values of Table 6.1 in the dispersion relation (6.35), we obtain the dispersion relation diagram shown in Fig. 6.3, The dashed-dotted black line shows the dispersion relation in the dielectric (given by the well known relation $k = \omega/c$), the solid blue curve denotes the real part of the plasmon dispersion relation β, whereas the broken red line indicated the imaginary part of the β. The real part β determines the SPPs effective index as well as the SPP wavelength (as they are given by the equations (6.36) and (6.37) respectively), while the imaginary part β accounts for the damping of the SPPs energy as they propagate along the interface. Finally, the green circles shows the characteristic plasmon frequency ω_{sp} which is given by the equation (6.39). Furthermore, in the Fig.6.3 all the wavenumbers are normalized to $k_p \equiv \omega_p/c$ and the frequency to the plasma frequency ω_p.

There are three interesting regimes of frequency ω in the dispersion relation curve of Fig.6.3. First of all, the most interesting regime is when β takes its maximum value, which is called *characteristic surface plasmon frequency* ω_{sp}. This characteristic frequency ω_{sp} can be calculated by demanding $\beta \to \infty$ and assuming a lossless Drude metal, i.e. $\Gamma = 0$, resulting to $\mathrm{Im}\left[\varepsilon_m\right] = 0$. In this sense and substituting the ω by ω_{sp}, the dispersion relation of equation (6.35) yields to the ω_{sp} equation (6.39).

$$\omega_{sp} = \frac{w_p}{\sqrt{\varepsilon_h + \varepsilon_d}} \tag{6.39}$$

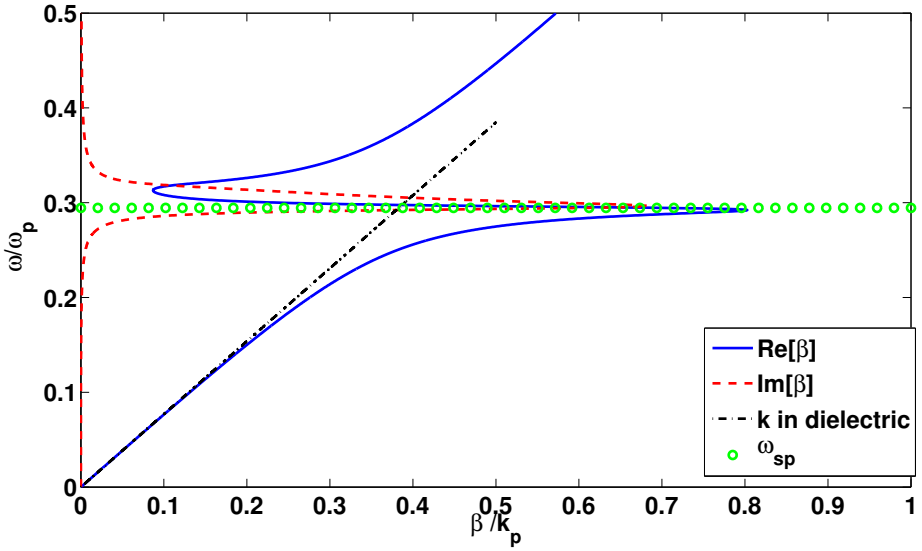

Figure 6.3: Dispersion relation (6.35) of SPPs at the interface between a Drude metal and a dielectric. The blue solid line denotes the real part of the dispersion relation whereas the broken red line shows the imaginary part of the dispersion relation. The dashed-dotted black line indicates the light dispersion relation in the dielectric and finally the green circles is for the surface plasmon frequency ω_{sp}

The other interesting regime is for sufficient small frequency, i.e. $\omega < 0.2\omega_p$, where the SPP constant β is close to light wavenumber k_0; the surface waves of this regime are known as Sommerfeld-Zenneck waves. Finally, at high frequencies the metal is transparent to the EM radiation, subsequently SPP modes cannot be supported at these frequencies.

As mentioned earlier, the most interesting regime is when ω of the EM approaches the ω_{sp}; in what it makes this regime interesting is that the SPPs propagation constant goes to infinitive ($\beta \to \infty$) and the group velocity goes to zero ($v_g = \partial\omega/\partial\beta \to 0$), that reveals the electrostatic behaviour of this mode and it is called *surface plasmon mode*.

Due to ohmic losses in the metal, characterized by the imaginary part of the the metal permittivity $\varepsilon_m(\omega)$ (for $\Gamma \neq 0$), the energy carried by an SPP decays exponentially as the SPP propagates along the planar dielectric-metal interface. The $1/e$ decay length, called *energy propagation length* L and it is determined by the imaginary part of the SPP wavenumber β as the equation (6.40) describes

$$L = \frac{1}{2\mathrm{Im}[\beta]} \tag{6.40}$$

Naturally, there is a similar expression for the propagation length the electric field L_F, read as

$$L_F = \frac{1}{\mathrm{Im}[\beta]} \tag{6.41}$$

In the visible regime a typically propagation length of the SPPs intensity L is about $10\mu m$ to $100\mu m$.

Finally, we would like to know how deeply the SPPs EM field penetrates to the dielectric or to the metal; thus we define the *field penetration length* t_i in the dielectric (i = d) or in metal (i = m), which is given by the equation

$$t_i = \frac{1}{k_0}\mathrm{Re}\left[\sqrt{\frac{\varepsilon_d + \varepsilon_m}{-\varepsilon_i^2}}\right] \qquad \text{(for i = d, m)} \tag{6.42}$$

6.3 Excitation of surface plasmon polaritons (SPPs) at planar interfaces

We have already examined about the conditions that are needed in order to have SPP modes, but we have not discusses anything of the excitation of such modes. In this Section, we investigate the excitation of SPPs in a planar interface between a dielectric and a metal. We describe an excitation method and thereafter we simulate, using COMSOL multiphysics software, the excitation as well as the propagation of SPPs. In addition, we calculate the dispersion relation with COMSOL and compare it with the analytical findings obtained by equation (6.35) and shown in Fig.6.3.

There are two commonly used configurations, namely Kretschmann-Raether and Otto configurations shown in Fig.6.4a and in Fig.6.4b respectively. In the first (6.4a), a thin metal film ($40 - 70nm$) is sandwiched between two dielectrics with the incident EM wave hitting initially the optical denser medium. In the Otto configuration (6.4b), the denser dielectric and the metal sandwich the lighter medium, with the incident EM wave hitting also the denser dielectric first [75, 78–81].

In this study, we use the Kretscmann-Raether configuration of Fig.6.5, that is, a metal of thickness d and permittivity ε_2 is sandwiched between two dielectric layers with permittivity ε_1 and ε_3 respectively, with the precondition $\varepsilon_1 > \varepsilon_3$. In addition, a plane EM wave source with TM polarization has been located in the first medium; the wave vector of the incident TM wave is k_1 and the refracted wave in the next two layers are k_2 and k_3 respectively. The permittivity of the metal is frequency dependent and given by the Drude model of equation (6.38). In our analysis we use silver and two different kinds of silica glass; Table 6.2 denotes the parameters used.

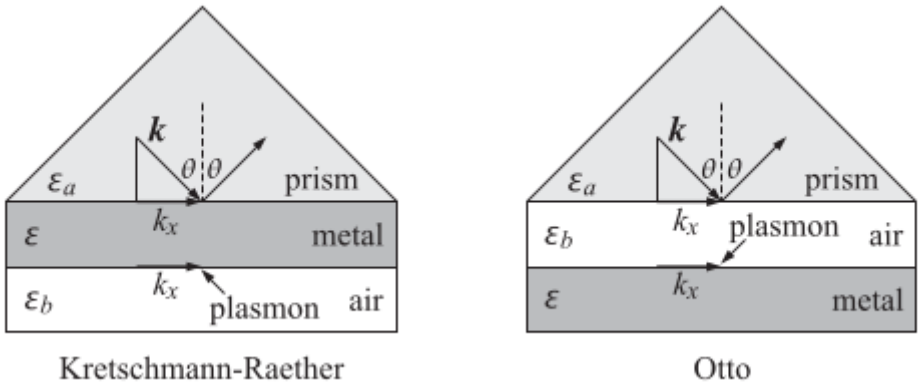

Figure 6.4: Excitation of surface plasmons (SPPs) using the ATR method, in the (a) Kretscmann-Raether configuration (b) Otto configuration.

Table 6.2: Values of parameters for SPPs excitation.

Parameter	Value
ε_1	2.25
ε_3	1.69
d	$50nm$
Γ	$1.018 \cdot 10^{14}\ rad/sec$
ω_p	$1.367 \cdot 10^{16}\ rad/sec$
ε_h	9.84

In Kretscmann-Raether as well as in Otto configurations, the method that is used for exciting SPPs is called *attenuated total reflectance* (ATR) method. When an EM wave is propagating in a dielectric and is made incident on the metal film, a part of the light is reflected back into the dielectric whereas the other a part is propagating in the metal, with phase velocity parallel to the interface, in the form of an inhomogeneous EM wave [75, 79]. This inhomogeneous EM wave decays exponentially in the direction perpendicular to the dielectric-metal interface and is therefore an evanescent wave. If the metal film is sufficiently thin (less than $100nm$ for the light in visible and near infrared part of EM spectrum), the evanescent wave penetrates through the metal and couples with a surface plasmon at the outer boundary of the metal film. This is the most famous method for SPPs excitation called ATR method.

The interaction between a light wave and a surface plasmon in the ATR

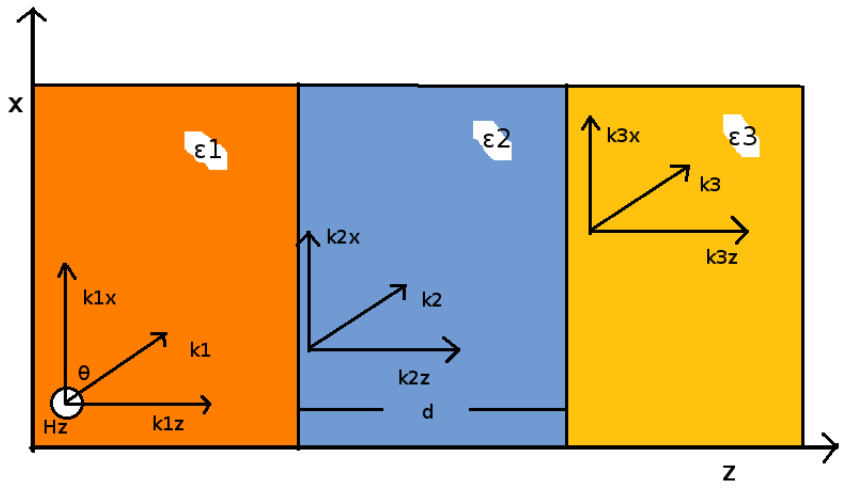

Figure 6.5: A waveguide (layer structure) based on Kretscmann-Raether configuration and used for surface plasmon excitation

method can be investigated using the Fresnel multilayer reflection theory [75, 78, 79, 81]. Consider a layer with Kretscmann-Raether configuration, as illustrated in Fig. 6.5, with $\varepsilon_1 > \varepsilon_3$, which is illuminated by a TM EM wave with impingement angle θ and wavenumber k_0. In the below we are going to calculate the reflectivity coefficient R. In these terms, we are interested in the minimum of R, that is, the most part of energy of the incident EM wave penetrates through the metal and therefore excites the SPPs modes at the outer side of the metal film.

First of all, we have to discuss a few things about the components of k vector. The perpendicular in interface component k_{iz}, where i shows the media ($i = 1, 2, 3$), is given by

$$k_{iz} = \sqrt{k_0^2 \varepsilon_i - k_x^2} \tag{6.43}$$

where k_x the $k-$component along the interface, k_0 the wave number of the incident EM wave and ε_i the permittivity of the i media. In addition, the two components of k_0 vector can be analysed in terms of incident angle θ, namely

$$k_{1z} = k_0 n_1 \cos(\theta) \tag{6.44}$$

$$k_{1x} = k_0 n_1 \sin(\theta) \tag{6.45}$$

where $n_1 = \sqrt{\varepsilon_1}$ the refractive index in the first dielectric.

Because of the continuity of the electric field, as Snell law states, the transverse in propagation component of the k vector, i.e. k_{ix} are preserved across the media, thereby

$$k_x = k_{1x} = k_{2x} = k_{3x} = k_0 n_1 \sin(\theta) \tag{6.46}$$

where we used the relation of the equation (6.45).

According now the Fresnel theory [78,79,81], the total reflection response A of the structure is given by

$$A = \frac{\rho_1 + \rho_2 \exp(-2ik_{2z}d)}{1 + \rho_1\rho_2 \exp(-2ik_{2z}d)} \tag{6.47}$$

where ρ_1 and ρ_2 are the TM reflection coefficients at the two interfaces and given by

$$\rho_1 = \frac{\varepsilon_1 k_{2z} - \varepsilon_2 k_{1z}}{\varepsilon_1 k_{2z} + \varepsilon_2 k_{1z}}, \qquad \rho_2 = \frac{\varepsilon_2 k_{3z} - \varepsilon_3 k_{2z}}{\varepsilon_2 k_{3z} + \varepsilon_3 k_{2z}} \tag{6.48}$$

Finally, the reflectivity R (power reflection coefficient) of the structure is given by the square of the absolute value of the reflection response A of the equation (6.47), that is

$$R = |A|^2 \tag{6.49}$$

Furthermore, we proceed with numerical simulations using COMSOL multiphysics software, for the excitation of SPPs at the planar interface of Fig.6.5. In our analysis we use silver and two different types of silica glass; Table 6.2 shows the values used; the angular frequency of the incident monochromatic EM wave, which is used for SPP excitation, is $\omega = 0.22\omega_p$. First of all, we are looking for the optimal incident angle corresponds to the minimum of the reflection response of the incident wave [75, 78–83]. Fig.6.6 indicates with solid blue line the theoretical prediction of the reflection response based on equations (6.47)(6.49) as function of incident angle, whereas the red circles are COMSOL's results. At the resonance angle of $\theta = 66.74^o$ the maximum amplitude of SPPs is formed.

In Fig.6.7 we show the magnetic field distribution (xz plane) at resonance. We have imposed Floquet periodic boundary conditions on both up and down boundaries for a better representation of the plasmon [81]. The major diagram is a color scaled image of the magnetic field while the top right insert is the corresponding 3D plot and the bottom right insert diagram is the characteristic profile of the magnetic field distribution along the z-axis, across the materials [81].

We proceed with numerical calculation of the SPPs dispersion relation. Using the same materials and the same geometry, we are sweeping the angular frequency in terms of plasmon frequency ω_p, viz. $\omega = 0.05\omega_p$ to $0.35\omega_p$ and

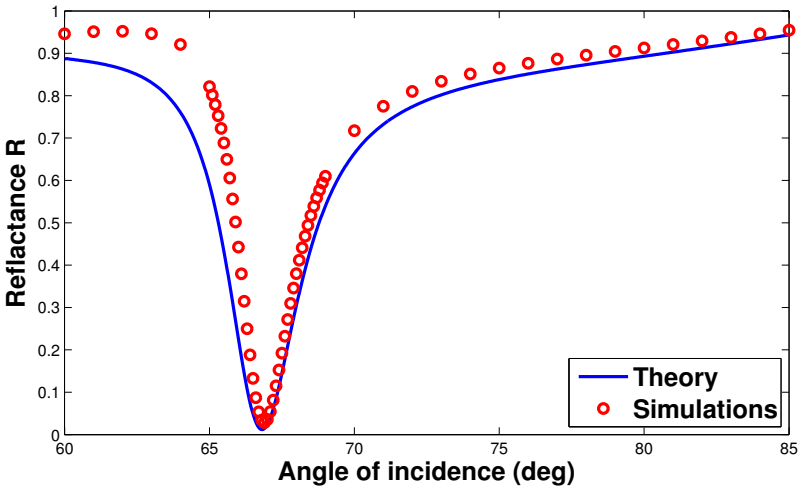

Figure 6.6: Angle dependence for the Kretschmann-Raether configuration: Analytical calculations (blue line) and COMSOL simulation (red circles). The resonance angle is at $\theta = 66.74^o$ and corresponds to the angle for which the total reflection response is minimum yielding to maximum amplitude of SPPs.

compute with COMSOL the plasmon propagation constant β. In Fig.6.8 we plot the dispersion relation (real and imaginary part respectively) for the materials (both metal and dielectrics). Points are results obtained by COMSOL simulations, solid lines are theoretical plots of equation (6.35), while dashed lines are the light dispersion relation ($\omega = kc/n$) in the two dielectrics with refractive index $n = \sqrt{\varepsilon}$.

6.4 Active dielectrics in plasmonic systems

In this Section, we investigate SPPs properties, namely the SPP dispersion relation and propagation length in the presence of active (gain) dielectrics. First of all, active materials are called the materials that have complex permittivities, i.e. $\varepsilon_d = \varepsilon_d' + i\varepsilon_d''$, where the the imaginary part ε_d'' accounts for gain [80, 82, 84–90]. In our analysis we replace the second (optical lighter) dielectric with an active dielectric and we define, for convenience, the permittivity of this gain material by means of refractive index, i.e. $\varepsilon_3 = (1.3 + i\kappa)^2$, where κ accounts for gain. Gain will counterbalance the ohmic loss of the metal in the SPP propagation, subsequently the sign of the imaginary part of permittivity, of an active material has to be opposite as a regard to the sign of the imaginary part of metal's permittivity (which

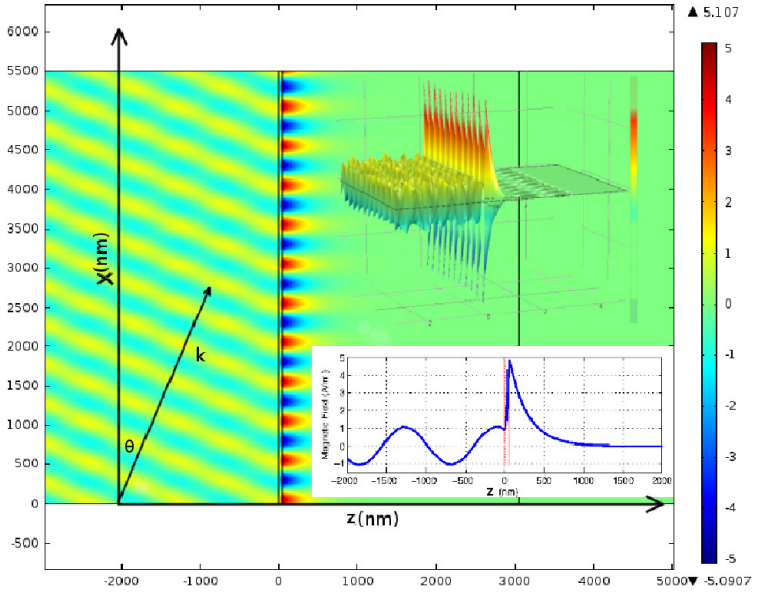

Figure 6.7: Magnetic field $H_z(x, z)$ at the resonance angle (COMSOL simulation). The major diagram is a color scaled image of the magnetic field while the top right insert is the corresponding 3D plot and the bottom right insert is the characteristic profile of the magnetic field distribution along the z-axis, across the materials.

accounts for loss). Table 6.3 shows the parameters used for the analytical as well as for the numerical calculations of SPPs properties in the presence of an active dielectric.

Firstly, we study the dispersion relation in the presence of an active dielectric. As mentioned, the dispersion relation of equation (6.35) holds also for complex permittivities ε_d and ε_m. In Fig.6.9 we present the real and the imaginary part of the SPPs dispersion relation β in the presence of a gain material with $\kappa = 0.007$; for comparison, the real and imaginary parts of β are shown, when a purely real ε_3 is used, i.e. $\kappa = 0$. The red solid curve and points are for the case where an active dielectric used and indicate the analytical results based on equation (6.35) and the COMSOL results respectively; the blue curve and points are for a pure real permittivity ε_3 and show again the analytical and numerical results respectively. The agreement between analytical results and COMSOL simulations confirm the correctness of our numerical simulations.

There are two interesting results shown in Fig.6.9. First of all, the Fig.6.9a shows that the introduction of an active dielectric shifts the curve of the real part of dispersion relation towards a greater wavenumber β resulting to SPP

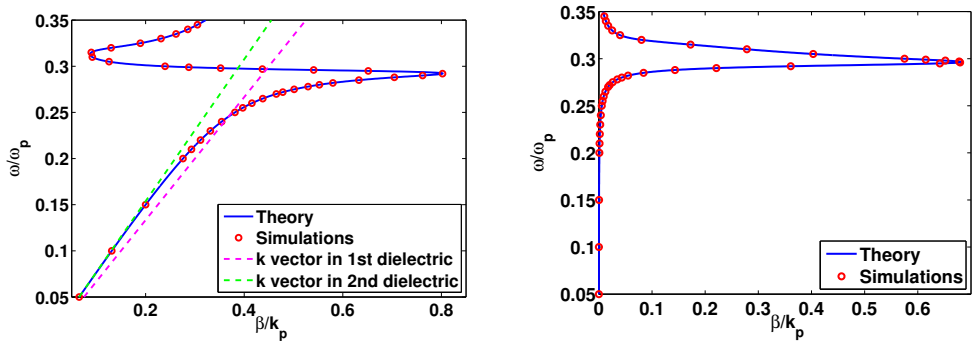

Figure 6.8: Dispersion relation. The left diagram (a) is the real part of the dispersion relation. The dashed purple line denotes the light dispersion relation (k vector) in the first dielectric whereas the dashed green line is the light dispersion relation for the second dielectric. The blue solid line is the real part of dispersion relation of SPPs based on equation (6.35) whereas the red circles show the COMSOL results. The right diagram (b) indicates the imaginary part of SPPs dispersion relation based on equation (6.35). The blue solid line is the imaginary part of dispersion relation of SPPs based on equation (6.35) whereas the red circles show the COMSOL results. In both diagrams (a-b) ω_p and $k_p = \omega_p/c$ are normalization constants.

with higher energy and intensity of EM field. Secondly, the Fig.6.9b indicates that the gain material shifts the imaginary part of dispersion relation towards a smaller imaginary part of β yielding to longer SPPs propagation length L, regarding to the equations (6.40)(6.41) [80, 84–86].

The previous results can be illustrated in the Fig.6.10, where we plot the intensity of magnetic field obtained by COMSOL simulations for a pure real permittivity ε_3 ($\kappa = 0$) and for two active dielectrics with different gain parameter, viz. $\kappa = 0.002$ and $\kappa = 0.007$. First of all, Fig.6.10 denotes the magnetic field across the materials showing that the maximum amplitude of the magnetic field is significantly greater as it has predicted by Fig.6.9a. Moreover, the Fig.6.10b is the the magnetic field across the interface; as it is expected (Fig.6.9b), the propagation length is enhanced by the introduction of the active dielectric.

Investigating deeper the dispersion relation (6.35) deeper, we can see that in the presence of complex dielectric permittivity, a root in the imaginary part of β is revealed, in contrast to the case where passive dielectrics are used, wherein the imaginary part of β is always non-zero. Subsequently, the propagation length given by the equation (6.40) becomes infinity since $\mathrm{Im}[\beta] = 0$, resulting to SPPs propagation without losses. This is the most

Table 6.3: VALUES OF PARAMETERS FOR SPPS EXCITATION IN THE PRESENCE OF ACTIVE DIELECTRIC.

Parameter	Value
ε_1	2.25
ε_2	$-15.13 - 0.93i$
ε_3	$(1.3 + i\kappa)^2$
κ	Varies from 0 to 0.0099
d	$50nm$
θ	66.74^o

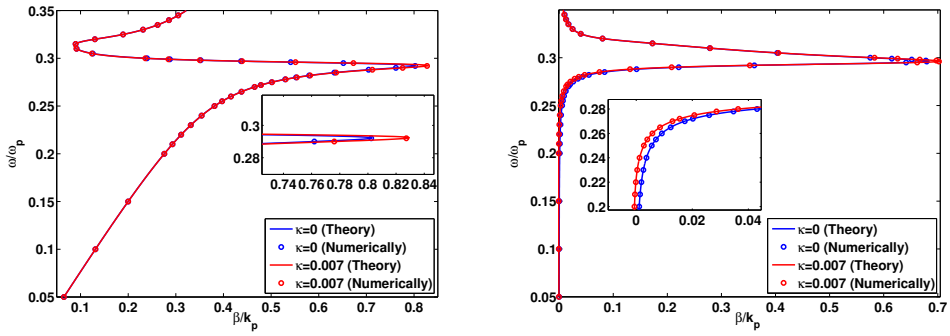

Figure 6.9: Dispersion relation with the presence of active dielectric. The points are the COMSOL simulations while the lines are analytical calculations based on equation (6.35). The Left image shows the real part of β whereas the right image the imaginary part. The red line and points are for gain materials with $\kappa = 0.007$ whereas the blue line and points are for a non-active dielectric i.e. $\kappa = 0$.

interesting result of this Section, since a lossless SPPs propagation cannot be achieved without the presence of active materials. Furthermore, this loss-gain counterbalance offers additional perspectives for the existence of Parity-Time symmetry (PT) plasmonic systems.

Furthermore, we proceed with a numerical experiment using COMSOL, in order to measure the SPP propagation length L, for different values of gain κ, to quantify the dependence of L as function of the gain parameter κ. In Fig.6.11 we show, on semilog scaling, the COMSOL results (points) as well as the fits (solid lines) of the magnetic field intensity along the interface, for a few values of gain. The fits estimate the slopes that correspond to the propagation length; COMSOL findings for various gains are represented in Table 6.4. As a result, as the gain κ increases, the SPPs propagate longer

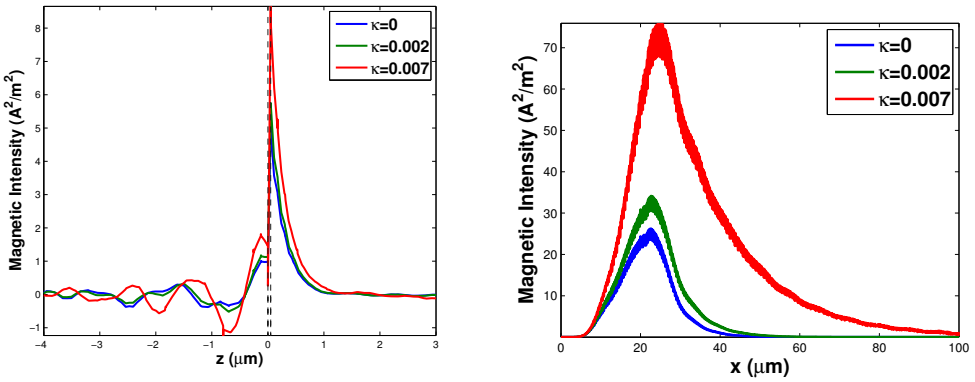

Figure 6.10: Intensity of the magnetic fields with and without presence of gain dielectric. (Left) Magnetic field across the materials for dielectric with no gain $\kappa = 0$ (blue line) same as in Fig.6.7 and for gain $\kappa = 0.002$ (green line) and $\kappa = 0.007$ (red line). Dashed line indicate the metal boundaries. (Right) Magnetic field on the interface for dielectric with no gain (blue line; bottom), and for gain $\kappa = 0.002$ (green line; middle) and $\kappa = 0.007$ (red line; top).

along the interface. For instance, gain of 0.6% (imaginary part over real part of refraction index) facilitates plasmon propagation by a factor of three. At the limit when the imaginary part of the propagation constant tends to zero (ohmic losses are counterbalanced by the gain), plasmons propagate without losses and propagation length goes to infinity (the fit to an exponential curve is not appropriate). This critical gain, obtained numerically with COMSOL, gives a plasmon propagating at constant amplitude.

Table 6.4: Propagation length obtained by COMSOL simulations.

Gain κ	Propagation length (μm)	Gain κ	Propagation length (μm)
0	5.7	0.009	53.9
0.002	6.9	0.0092	69.7
0.004	8.6	0.0094	99.3
0.005	10.0	0.0095	125.3
0.006	12.3	0.0096	169.5
0.007	16.3	0.0097	261.2
0.008	25.1	0.0098	564.7
0.0085	34.2	0.0099	∞, constant amplitude

Finally, we plot in Fig.6.12 the propagation length L as a function of

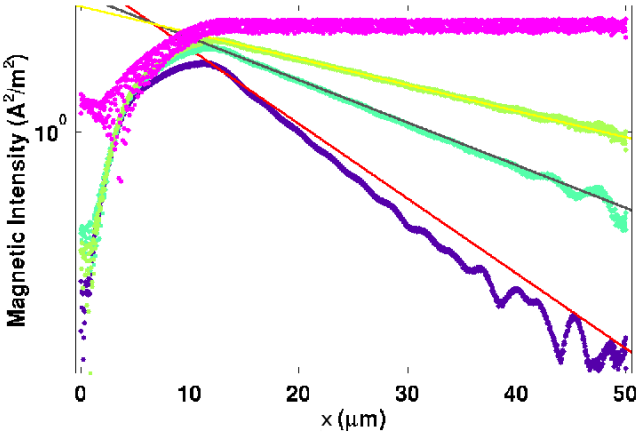

Figure 6.11: Plasmon propagation length for different gain values κ: The blue solid line denotes the theoretical prediction based on equations (6.35)(6.40) whereas the green points are the COMSOL simulations obtained by the Table 6.4.

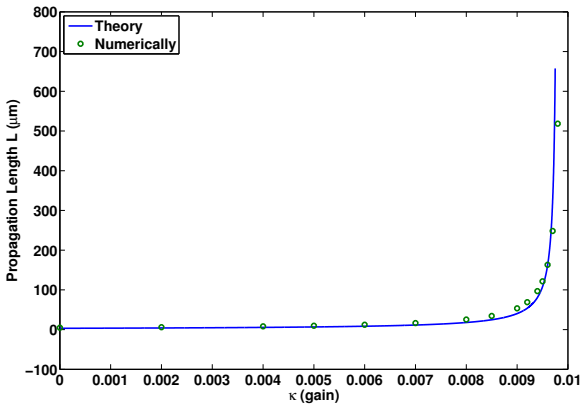

Figure 6.12: Plasmon propagation length for different gain values κ: The blue solid line denotes the theoretical prediction based on equations (6.35)(6.40) whereas the green points are the COMSOL simulations obtained by the Table 6.4.

gain parameter κ; the theoretical values obtain by the equations (6.35) and (6.40) and they are plotted by solid line, whereas the numerical values obtained by the Table 6.4 and they are shown by points. Obviously, there is a critical gain in which the propagation length tends to be infinitive resulting SPPs propagation without losses. This is the most interesting result of this Chapter.

Chapter 7

Conclusion and Outlook

In this Thesis, several topics regarding the EM waves propagation and light-matter interactions, have been discussed. In this closing Chapter, I present all interesting findings and I propose several promising continuations along the research lines followed in this Thesis.

I have developed four methods for the description of light propagation via two dimensional GRIN MMs (presented in Chapter 1). The first three methods are bounded by the geometrical optics limit and they are ray-tracing methods, i.e. the wave behaviour of light are neglected and the optical laws have been formulated in geometrical terms; as a result the EM waves are treated as rays. These geometrical optics methods yield analytical ray tracing equations for given function of refractive indexes; I have computed analytically the ray tracing equation of motion for light propagation through an LL as well as via an LH lens. The latter method that has been developed is a numerical method called FDTD, which solves the Maxwell time dependent equations, resulting to the time evolution of EM field through a media with given functions of permittivity and permeability. The finding obtained by the geometric optics methods are in agreement with those obtained by the FDTD method, thus verifying the rightness of the methods. It will be important to generalize these methods in three dimensional space, in order to solve more realistic problems for light propagation.

Having developed the mathematical tools for the description of EM waves propagation via GRIN MMs, I have proceeded, in Chapter 2, with investigation of networks of such GRIN lenses. Specifically, light propagation through specific configurations of LLs have been investigated, showing that EM waveguides (LLW) can be formed by GRIN lenses. As an example of LLWs, a beam splitter consisted of LLs has been presented.

The advantage of LLW compared to ordinary fibers is that the properties of GRIN networks are derived by the properties of the unit lens which com-

prises the networks. This is a meta-material approach, since we can perform the desired macroscopic properties of a GRIN network by analysing the properties of each lens, which is the "atomic" unit of the network. As a result, it will be very interesting to use LLW instead of usual fibers, since LLWs give more control to light propagation. In addition, integrated photonic circuits may be constructed using such GRIN networks.

In addition to ordered lattices, random networks of GRIN lenses have also investigated. LLs and LHs have been arranged randomly comprising a disordered network. Afterwards, the propagation of EM waves has been investigated resulting to the onset of extreme events, such as branching flow and optical rogue waves (RWs). Cases with different strength of lenses have been studied; where the strength is given by the maximum difference of the refractive index of lenses Δn, compared to the background index, and it is also related to the standard deviation σ of the lenses. In Chapter 3, I have studied the weak limit, i.e. $\Delta n < 10\%$. Specifically, I have shown that in EM waves propagation through a weak random network, which is consisted of weak LLs in random positions, caustics formation can arise. An analytical theory based on FPE has been presented, giving analytical results for the statistical law which rules the position of the first caustic in such process. This law is given by means of standard deviation of the optical potential and holds for several wave sources, such as point and plane wave sources.

Future work may focus on the generalization of the caustic theory in order to include the strong scattering limit, i.e. high standard deviation of the random potential, viz. $\sigma > 10\%$. Moreover, it will be interesting to see how in the presence of nonlinearity, i.e. the Kerr effect, affects the caustics formation as well as the location of the first caustic. In addition, there is an endogenous difference between the theory and the numerical experiments. In theory we assume a continuous delta-correlated random potential, however our disordered networks are strongly correlated because there is free space (with constant and known optical potential) between the lenses. An idea for further investigation is to use a dichotomous noise instead of the white noise; in such process, we may use Levy walk approach instead of Brownian walk.

Furthermore, in Chapter 4 the strong scattering limit, i.e. $\Delta n \sim 30\%$, has been investigated, showing that optical rogue waves can arise in the absence of nonlinearity. In this Thesis, it has been proposed that the mechanism, which is responsible for the onset of such extreme events, depends on the strong scattering properties of the medium as well as of the level of disorder. In addition, I have shown that the introduction of weak nonlinearity does not affect neither the position nor the statistics of linear RWs, revealing that the dominant role belongs to the linear nature of the the phenomenon.

It will be important to study the similarities and the differences between

linear and nonlinear RWs. Furthermore, it will be interesting to find a method in order to recognise linear from nonlinear RWs. In addition, since the observed RWs are linear, there are several mathematical approaches for investigation; for instance it will be interesting to analyse the eigenvalues of the optical potential, where the RWs have been observed; we may see the sign of RWs in the distribution of eigenvalues. Another idea is to approach the system as a many body problem; therefore, in this sense, we may find a strange or a limit cycle attractor which would be responsible for the existence of such extreme events. Finally, as a future application, a random network may be constructed in order to give a RW in a predefined position; this will be important because such a network may be used for fabrication of hyper focus lens.

In addition to GRIN lenses, I have studied in Chapter 5 light EM wavepackets propagation through disordered optical coupled fiber lattices. A simple model based on DNLS has been used for studying such propagation; the aim of this investigation was to determine the effects of randomness and of nonlinearity in the diffusive properties of such processes. We have found that randomness and nonlinearity change the process from ballistic diffusion to sub-diffusion regime. Further, the combination of both disordered and nonlinearity yields to a much lower diffusion exponent.

For the random arrangement of the fibers, I have used a delta correlation function, i.e. uncorrelated position of fibers, and I have also used a square lattice in which the fibers have been arranged. It will be interesting to investigate how the diffusion properties will be changed if a different correlation function, for instance exponential or power law correlation will be used and if different boundaries of lattice will be applied, like circular, triangular or honeycomb lattices. In my view, the diffusion exponent will be change considerably, because it strongly depends on the topological properties of the network. In addition, since the theory that has been developed in Chapter 5 is general, it will also be interesting to apply the presented model in other physical and non-physical system (such as financial systems).

Finally, a well known light-matter interaction mode, called surface plasmon polaritons (SPPs), has been investigated in Chapter 6. The basic theory for the description and for the understanding of such quasi particles has been developed. Moreover, I have presented a method for the excitation of SPPs, based on the ATR technique. Furthermore, active (or gain) dielectrics (dielectrics with complex permittivity) have been introduced and it has been investigated how these active materials affect the properties of SPPs (such as the SPPs dispersion relation and the propagation length). The main result of this analysis is that there is a critical value of gain, where the ohmic losses of metal are counterbalanced by gain, resulting to infinite SPPs propagation

(propagation without losses).

There are several promising ideas regarding plasmons, due to the fact that SPPs are relatively new in the field of applied physics. First, it will be interesting to investigate the PT symmetry in plasmonic systems in the area where the loss has been counterbalanced by gain. Secondly, an analysis of two or more interactive SPPs in the presence of active materials have not been done yet (to my knowledge); it will be interesting to see if new properties will arise in such a case. Finally, it has been shown that plasmonics GRIN meta-materials can be formed [91–93]. That gives the opportunity to apply the ideas about GRIN lenses, which have been discussed in this Thesis, in plasmonic systems. For instance, plasmonic LL has been formed in Ref. [92, 93], as a result LLW may be constructed in order to guide SPPs giving much more control in SPPs propagation. In addition, if we are able to guide SPPs, integrated plasmonic circuits may be formed as well as combinations of plasmonic and photonic circuits giving much more advantageous optical systems. Apart from plasmon LLW, it will be interesting to study SPPs propagation in random media, such as those discussed in Chapters 3 and 4. SPPs caustics as well as plasmon RWs may be found, opening a new very promising "world" in plasmon physics.

Appendix A

Hamiltonian ray tracing method in quasi two dimensional approach

We present the Hamiltonian ray tracing method for the quasi two dimensional (2D) approach. Starting with the optical Lagrangian $\mathcal{L}$, which is calculated in Section 1.1 and given by the equation (1.6), we proceed with the calculation of the corresponding Hamiltonian. Finally we solve the Hamilton's equations to obtain a ray tracing equation of motion for al travelling beam via a media with refractive index given by an arbitrary, radial dependent, function $n(r)$.

Assume a Lagrangian $\mathcal{L}$ by means of generalized coordinates q_i, generalized velocities $\dot{q}_i$ and time t; the standard way to calculate the corresponding Hamiltonian $\mathcal{H}$, in terms of generalized coordinates q_i, conjugate momenta p_i and time t, is to apply the Legendre transform of equation (A.1) [7, 8], to the Lagrangian $\mathcal{L}$, that is

$$\mathcal{H} = \sum_{i}^{N} \dot{q}_i p_i - \mathcal{L} \tag{A.1}$$

Where N denotes the dimension of the problem (or the degrees of freedom) and the dot indicated derivative with respect to time t. The conjugate momenta are calculated by differentiating the Lagrangian with respect to the generalized velocities $\dot{q}_i$ [7, 8], thus

$$p_i(q_i, \dot{q}_i, t) = \frac{\partial \mathcal{L}}{\partial \dot{q}_i} \tag{A.2}$$

The velocities $\dot{q}_i$ are expressed in momenta p_i by inverting the expression (A.2); thereafter the velocities are substituted in Legendre transformation

(A.1) by momenta, resulting to a Hamiltonian in terms of generalized coordinates and momenta q_i and p_i respectively.

The quasi 2D approach gives the opportunity to reduce the dimensions (or the degree of freedom) of the problem, since in this approach one of the spatial coordinates plays the role of time. In Polar coordinates the quasi 2D approach states that the role of time t belongs to the radial coordinate r, subsequently, the only dependent coordinate is the angular coordinate ϕ. As a result, we have an one dimensional mathematical problem, i.e. $N = 1$, with Lagrangian and Hamiltonian having the forms $\mathcal{L}(\phi, \dot{\phi}, r)$ and $\mathcal{H}(\phi, p_\phi, r)$ respectively, where the dot indicates differentiation with respect to r. The conjugate momenta is given by the formula (A.2) for the Lagrangian (1.6), that is

$$p_\phi = \frac{\partial \mathcal{L}}{\partial \dot{\phi}} = \frac{n r^2 \dot{\phi}}{\sqrt{1 + r^2 \dot{\phi}^2}} \tag{A.3}$$

where n is the refractive index with radial dependence, i.e. $n = n(r)$. Inverting the expression (A.3), we obtain for the $\dot{\phi}$

$$\dot{\phi} = \frac{p_\phi}{r\sqrt{n^2 r^2 - p_\phi^2}} \tag{A.4}$$

The last step for obtaining the desired Hamiltonian is to apply the Legendre transformation of equation (A.1) with $N = 1$ to the Lagrangian of equation (1.6) and using the equation (A.4). As a result, we obtain the optical Hamiltonian for the quasi two dimensional approximation, thus

$$\mathcal{H} = -\frac{\sqrt{n^2 r^2 - p^2}}{r} \tag{A.5}$$

Since the Hamiltonian (A.5) is cyclic in ϕ, the conjugate momenta p_ϕ is constant. Subsequently, we can proceed our calculation by solving the differential equation (A.4) by replacing the term $\dot{\phi} = d\phi/dr$ and solving for $d\phi$; we obtain the same first integral of motion as the integral (1.9) of Section 1.1. Finally, we proceed with the same calculations as the Section 1.1 to obtain the ray tracing solution (1.16).

Appendix B

Discretization by means of the finite difference in time domain method

In this section, we briefly discuss and develop an FDTD algorithm. As it mentioned in Section 1.4, FDTD is a numerical approach used for solving the time depended Maxwell equations (1.42) (1.43). Since in this Thesis we are using only TM mode propagating EM waves, we are going to develop an FDTD code for solving Maxwell equations only for TM polarization.

First of all, we have to discrete the equations (1.48) (1.49) (1.50) used for partial derivatives the central-difference approximation, which is given by formula (1.53). In addition, we use a rectangular two dimensional lattice described by the orthocanonical coordinates x, y; moreover, we denote any arbitrary grid point (i, j) of our configuration space as

$$(i, j) = (i\Delta x, j\Delta y) \tag{B.1}$$

Similarly, for any arbitrary function of space and time, we have

$$F(i\Delta x, j\Delta y, n\Delta t) = F^n(i, j) \tag{B.2}$$

where Δx, Δy and Δt the size of the two spatial and time unit cells respectively. Using now the notations (B.1) and (B.2) together with the central-difference approximation (1.53), we obtain for the electric and magnetic com-

ponents, E_z, H_x, H_y, the following discretized equations.

$$H_x^{n+1}(i,j+1) = H_x^n(i,j+1) + \frac{\Delta t}{\mu \Delta x}\left(E_z^n(i,j+1) - E_z^n(i,j)\right) \tag{B.3}$$

$$H_y^{n+1}(i+1,j) = H_y^n(i+1,j) + \frac{\Delta t}{\mu \Delta y}\left(E_z^n(i+1,j) - E_z^n(i,j)\right) \tag{B.4}$$

$$\begin{aligned} E_z^{n+1}(i,j) = E_z^n(i,j) + \frac{\Delta t}{\varepsilon \Delta y}\big(H_y^n(i+1,j) - H_y^n(i,j) + \\ + H_x^n(i,j) - H_x^n(i,j+1)\big) \end{aligned} \tag{B.5}$$

where the permittivity and permeability are also two dimensional functions, viz. $\varepsilon(i,j)$ and $\mu(i,j)$ respectively.

The equation (B.3)-(B.5) are the basic equations of this Appendix and they are going to be solved in time domain. The FDTD method states that for the calculation of each component in a time step $n+1$, the component from the previous time step n are used, naturally we call this process "update equations". We repeat this step (the update equations step) for any time is needed until the steady state is reached.

First of all, in order to develop an FDTD code, we have to set an EM source. In our study we use a monochromatic plane wave source (B.6) with amplitude E_0, wavelength λ and angular frequency $\omega = 2\pi c/\lambda$, where c the velocity of the EM wave. The source is located on the first sites (at $i = 1$ for all j), subsequently the EM waves propagate from left to right (Fig.B.1).

$$E(1,j) = E_0 \sin(\omega\ n\Delta t) \tag{B.6}$$

Having set the EM source, we proceed with the calculations of the equations (B.3), (B.4) and (B.5). Afterwards, we have to apply boundary conditions (BC). We use periodic boundary conditions (PBC) at the up and down edges (transverse sides) and absorbing boundary conditions (ABC) at the end; these are illustrated in Fig.B.1. The PBC is a good choice because with this way the energy is conserved, on the other hand the ABC at the end edge is also a good choice because with this way we simulate an infinity propagation space. Subsequently, the main body of an FDTD algorithm consists of three parts for every time step, (a) EM wave source implementation (b) calculations of Maxwell discrete equations (c) implementation of BC.

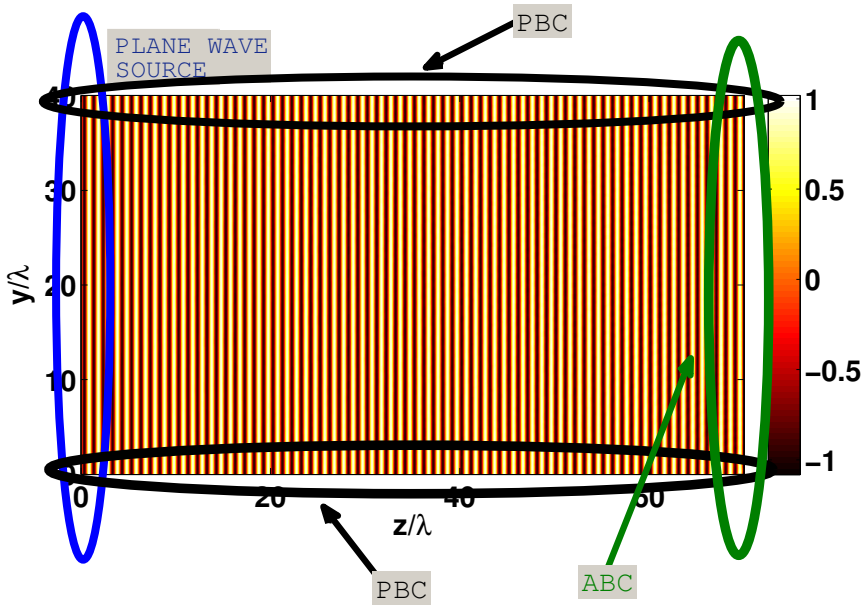

Figure B.1: A snapshot of the z component of electric field (E_z) is represented. The results are obtained by FDTD simulation for a monochromatic EM wave propagation in vacuum. A plane EM wave source has been located in the begging (blue curve on the left). Periodic boundaries conditions (PBC) have been applied at the up and down edges (black curve), since absorbing boundary conditions (ABC) has applied at the end (right side).

In the below, a brief plan of an FDTD code is represented.

SCHEMATIC ALGORITHM:

- Define and set up parameters
  - Grid sizes N_x, N_y
  - Define normalized units for wavelength λ and light velocity c; therefore we define the period T and the angular frequency ω of the EM wave source
    $> T = \frac{\lambda}{c}$; $\omega = \frac{2\pi c}{\lambda}$;
  - The unit cells Δx and Δy are defined according the first stability criterion that is discussed in Section 1.4
    $> \Delta x = \frac{\lambda}{20}$; $\Delta y = \frac{\lambda}{20}$;

  - Define the permittivity and permeability functions $\varepsilon(i,j)$ and $\mu(i,j)$ respectively.
  - Define the time step Δt according Courant stability criterion as it is discussed in Section 1.4 (equation (1.54))
    $> c_{max} = \max\left(c\left(\epsilon\mu\right)^{-\frac{1}{2}}\right);$
    $> \Delta t = \frac{1}{2c_{max}}\sqrt{(\Delta x)^2 + (\Delta y)^2}$

- Main body. In this part a time loop, with a time counter n, is running until the system reaches to steady state
  - Set the EM plane wave source, in the begin of lattice, i.e. for $i = 1$ and for all j; where i and j are the spatial counters for the propagation x and transverse y direction respectively
    $> E(1,j) = E_0 \sin(\omega\ n\Delta t);$
  - Calculation and update of EM components as they are given by the discretized equations (B.3), (B.4) and (B.5)
  - Implementation of boundary conditions, PBC for the up ($j = 1$) and down ($j = N_y$) edges and ABC for the end sites ($i = N_x$).

- Calculation of the steady state of EM component intensities
  - Run again the main body for a single or more periods T. The intensity is given by the time average of the square of each component
    $> I_{H_x} = \frac{1}{T}\sum_0^T |H_x(i,j)|^2$
    $> I_{H_y} = \frac{1}{T}\sum_0^T |H_y(i,j)|^2$
    $> I_{E_z} = \frac{1}{T}\sum_0^T |E_z(i,j)|^2$

Appendix C

Parabolic equation and the corresponding Fokker Plank equation

We present the derivation of the parabolic equation 3.31, which is a well known approximation for the description of wave fields, using the paraxial approximation in Helmholtz wave equation (1.31). Afterwards, we show that this parabolic equation yields to a FPE for the wave phase front, equivalent to FPE equation (3.19), by using the assumption that the EM waves propagate through a media with random fluctuated permittivity ε(or refractive index n), as a result the parabolic equation yields to the same statistical law for the caustic formation as is was described in Chapter 3.

Since our analysis is limited in two dimensions, we begin with a two dimensional Helmholtz wave equation (1.31) and write the bulk medium wavenumber k_0 in terms of bulk refractive index n_0 and wavenumber k, viz. $k_0 = k/n_0$, that is

$$\left[\nabla^2 + \left(\frac{nk}{n_0}\right)^2\right] u(x,y) = 0 \tag{C.1}$$

where $u(x,y)$ is any component of electric $\vec{E}(x,y)$ or magnetic $\vec{B}(x,y)$ field and the 2D Laplacian operator $\nabla^2 = \frac{\partial^2}{\partial x^2} + \frac{\partial^2}{\partial y^2}$.

Assuming that x is the propagation axis, the component u can be written as

$$u(x,y) = \psi(x,y)e^{ikx} \tag{C.2}$$

where $\psi(x,y)$ is a scalar function describes the amplitude of the propagated EM wave. Substituting the notation (C.2) to the Helmholtz equation (C.1),

we obtain after some calculations [1–5, 9]

$$\left[\frac{\partial^2}{\partial x^2} + 2ik\frac{\partial}{\partial x} + \frac{\partial^2}{\partial y^2} + k^2\left(\frac{n^2}{n_0^2} - 1\right)\right]\psi(x,y) = 0 \tag{C.3}$$

If we solve the equation (C.3), we then have the full solution to the scalar wave equation (C.1). Unfortunately, the equation (C.3) is challenging to be solved, consequently we proceed with the paraxial approximation which is a well known approximation in waves propagation. The paraxial approximation states that the amplitude of the fields varies only gradually along the propagation axis x. Mathematically, this approximation reads

$$\left|2ik\frac{\partial\psi}{\partial x}\right| >> \left|\frac{\partial^2\psi}{\partial x^2}\right| \tag{C.4}$$

Subsequently the equation (C.3) becomes [1–3, 9]

$$\left[2ik\frac{\partial}{\partial x} + \frac{\partial^2}{\partial y^2} + k^2\left(\frac{n^2}{n_0^2} - 1\right)\right]\psi(x,y) = 0 \tag{C.5}$$

The equation (C.5) is called *paraxial wave equation*. The term paraxial is used because all of the EM wave must travel nearly parallel to the x axis in order for the beam to have a sufficiently slow x dependence. The first term in equation appC:eq:paraxialWave shows the evolution of the scalar wave ψ; Furthermore, the middle term of the equation (C.5) is called diffraction term whereas the last one is called scattering term.

We proceed with another approximation. We keep only the fluctuating part of the refraction index, namely the term $(nk/n_0)^2$ and assume, for convenience, that the bulk medium is the vacuum, i.e. $n_0 = 1$. Subsequently the paraxial equation (C.5) becomes [26]

$$\left[2ik\frac{\partial}{\partial x} + \frac{\partial^2}{\partial y^2} + k^2\varepsilon(x,y)\right]\psi(x,y) = 0 \tag{C.6}$$

where we used the permittivity function ε instead of the refractive index n, via the relation $n^2 = \varepsilon$.

Let's introduce a wave field of the form [25, 26]

$$\psi(x,y) = A(x,y)e^{iS(x,y)} \tag{C.7}$$

where A is a real function describes the wave amplitude, while S is also a real function describes the curve of the wave front and denotes the fluctuation of the wave phase with respect to wave phase of the incident wave ($\sim e^{ikx}$)

[25, 26]. Substituting the notation (C.7) in the paraxial equation (C.6) and after some algebra we obtain the PDE

$$A'' + k^2\varepsilon A - A(S')^2 - 2kA\dot{S} + i\left(2A'S' + 2k\dot{A} + AS''\right) = 0 \tag{C.8}$$

where dots indicate differentiation with respect to x ($\dot{\alpha} = \partial\alpha/\partial x$), whereas the prime is for the differentiation with respect to y ($\alpha' = \partial\alpha/\partial y$)

In geometrical optics limit we have $k \to \infty$ as well as $S \to \infty$, subsequently the quotient S/k can be assumed constant. In addition, we are going to make another standard approximation taken from the quantum mechanics, that is, we divide the equation (C.8) with the term k^2, as a result the first term of equation (C.8), viz. A''/k^2, can be neglected since $k \to \infty$. After this approach, we separate the real from the imaginary parts of equation (C.8) obtaining a system of PDEs for the wave amplitude A and phase S [25, 26], that is

$$2k\dot{S} + (S')^2 = k^2\varepsilon \tag{C.9}$$

$$2AA'S' + 2k\dot{A}A + A^2S'' = 0 \tag{C.10}$$

Define now, for convenience, the wave intensity $I(x, y) \equiv A^2(x, y)$, the equations (C.9) and (C.10) can be written in the following more compact form

$$\frac{1}{k}\frac{\partial S}{\partial x} + \frac{1}{2k^2}\left(\frac{\partial S}{\partial y}\right)^2 = \frac{\varepsilon}{2} \tag{C.11}$$

$$k\frac{\partial I}{\partial x} + \frac{\partial}{\partial y}\left(I\frac{\partial S}{\partial y}\right) = 0 \tag{C.12}$$

In this point we may define two useful quantities. First of all, the equation (C.11) is of the form of a HJE, where the phase curve S plays the role of the classical action, as a result the conjugate momenta of the system can be defined as [7, 8, 25, 26]

$$p = \frac{1}{k}\frac{\partial S}{\partial y} \tag{C.13}$$

In addition to the conjugate momenta, we can define a function u, which describes a curvature of the phase front $S(x, y) = \text{const}$ (equivalent to the curvature of classical action), that is

$$u(x, y) = \frac{\partial p}{\partial y} = \frac{1}{k}\frac{\partial^2 S}{\partial y^2} \tag{C.14}$$

The curvature u is a useful quantity for investigating caustics or in general focus points, because its singularities, i.e. $u \to \infty$, reveals focus points or

caustics, where all the intensity (or energy) of system has been focused. In order to obtain a differential equation for the curvature u, we differentiate twice the equation (C.11) with respect to y and take account the relations (C.13) and (C.14). Subsequently, we obtain

$$\left[\frac{\partial}{\partial x} + p\frac{\partial}{\partial y}\right] u + u^2 = \frac{1}{2}\frac{\partial^2}{\partial y^2}\varepsilon(x, y) \tag{C.15}$$

The operator in the bracket of equation (C.15) is the convective or material derivative, which switch the differential equation from partial to ordinary [13, 31], since

$$\frac{d}{dx} = \left[\frac{\partial}{\partial x} + p\frac{\partial}{\partial y}\right] \tag{C.16}$$

As a result the PDE (C.15) turns to an ODE of the form

$$\frac{d}{dx}u + u^2 = \frac{1}{2}\frac{\partial^2}{\partial y^2}\varepsilon(x, y) \tag{C.17}$$

Using now the optical potential V, as it is defined in Section 1.2 by the equation (1.25), the equation (C.17) becomes

$$\frac{d}{dx}u + u^2 + \frac{\partial^2}{\partial y^2}V(x, y) = 0 \tag{C.18}$$

which is the same ODE with the equation (3.7); assuming now that the potential (or the fluctuations of the refractive index) acts as a random white noise in the propagated waves, we obtain the same FPE as the equation (3.19) which is derived in Chapter 3. Following the same analysis as the Section 3.1, we obtain the same scaling law that rules location of the first caustic in a media with random fluctuated permittivity.

Appendix D

Statistics of generalized Luneburg lenses networks

We present an analytical approximate method for the calculation of the standard deviation σ of a random network consists of LL lenses. We use the optical potential of equation (1.25) for the generalized LL refractive index function (3.34). We calculate analytically the standard deviation by means of LL strength parameter α as well as of filling factor f; the last is given by the following definition

$$f = \frac{2\pi R}{N \times M} L \tag{D.1}$$

where R the radius of each lens, (N, M) the size of a rectangular lattice and L the number of lenses. The values of f are between zero ($f = 0$ for a lattice without lenses) and one ($f = 1$ for a full filled lattice).

Firstly, in for our assumption, we introduce two potentials; V_L for the generalized LL of equation (3.34) and V_B for vacuum (bulk media). Using the equation (1.25) we obtain

$$V_L = -\frac{1}{2}\left(1 + \alpha\left(1 - \frac{r^2}{R^2}\right)\right) \tag{D.2}$$

$$V_B = -\frac{1}{2} \qquad . \tag{D.3}$$

Thereafter, we define approximately, an expression for the mean value of a random LL potential , that is

$$\langle V \rangle = f \langle V_L \rangle + (1 - f) \langle V_B \rangle \tag{D.4}$$

where $\langle V_L \rangle$ the mean value of a single LL potential V_L and $\langle V_B \rangle$ the mean value of the bulk potential with refractive index $n_0 = 1$ (for vacuum), which

are given by the following equations

$$\langle V_L \rangle = \frac{1}{\pi R^2} \int_0^{2\pi} d\theta \int_0^R r V_L dr = -\frac{1}{4}(2+\alpha) \tag{D.5}$$

$$\langle V_B \rangle = -\frac{1}{2} \quad . \tag{D.6}$$

Using the formula (D.4) with the findings that obtained by equations (D.5) and (D.6), we obtain for the mean value of the potential

$$\langle V \rangle = -\frac{1}{4}(\alpha f + 2) \tag{D.7}$$

We proceed to calculation of the standard deviation σ (or variance σ^2) using the general relation

$$\sigma^2 = \int_0^{2\pi} d\theta \int_0^R r \left(V^2 - \langle V \rangle^2 \right) dr \tag{D.8}$$

which is simplified by using the approximation (D.4)

$$\sigma^2 = f \left(V_L^2 - \langle V \rangle^2 \right) + (1-f) \left(V_B^2 - \langle V \rangle^2 \right) \tag{D.9}$$

Finally we obtain the standard deviation for a LL random network with filling factor f and LL strength parameter α

$$\sigma^2 = \frac{\alpha^2}{16}(1-f) f \tag{D.10}$$

$$\sigma = \frac{\alpha}{4}\sqrt{(1-f) f} \tag{D.11}$$

Subsequently, we show that the standard deviation of a random LL network is proportional to the strength parameter α. In addition, we will obtain the same result (the equation (D.11) if we use the LH refractive index of equation (4.1) instead of the LL.

Appendix E

Acronyms

ABS	:	Absorbing Boundary Conditions
ATR	:	Attenuated Total Reflection
BC	:	Boundary Conditions
BFPE	:	Backward Fokker Plank Equation
DNLS	:	Discrete Nonlinear Schrödinger equation
EM	:	ElectroMagnetic
FDTD	:	Finite Difference in Time Domain
FPE	:	Fokker Plank Equation
GRIN	:	Gradient Refractive Index
HJE	:	Hamilton-Jakobi Equation
LH	:	Luneburg Hole lens
LL	:	Luneburg Lens
LLW	:	Luneburg Lens Waveguides
LM	:	Lagrangian Manifold
MMs	:	Meta Materials
MSD	:	Mean Square Displacement
ODE	:	Ordinary Differential Equations
OSDE	:	Ordinary Stochastic Differential Equation
PT	:	Parity Time symmetry
PBC	:	Periodic Boundary Conditions
PDE	:	Partial Differential Equations
RW	:	Rogue Wave
SPP	:	Surface Plasmon Polariton
SWH	:	Significant Wave Height
TE	:	Transverse Electric Polarization
TM	:	Transverse Magnetic Polarization

Bibliography

[1] Born, M., Wolf, E.: Principles of optics. Oxford Pergamon, (1975)

[2] Kline M., Kay, I.W.: Electromagnetic theory and geometric optics. Interscience, New York (1965)

[3] Lakshimnarayanan, V., Ghatak, A.K., Thyagarajan, K.: Lagrangian Optics. Kluwer Academic Publishers (2002)

[4] Luneburg, R. K.: Mathematical Theory of Optics. Berkeley, CA: University of California press (1964)

[5] Stavroudis, O.N.: The Mathematics of Geometrical and Physical Optics: The k-function and its Ramifications. Weinheim: Wiley-VCH, Weinheim (2006)

[6] Mattheakis, M.M., Tsironis, G.P., Kovanis, V.: Luneburg lens waveguide networks. J. Opt. **14**, 114006 (2012)

[7] Goldstein H,, Poole C., Safko J.: Classical Mechanics. San Francisco, CA: Addison Wesley (2002)

[8] P. Hamill: A students's guide to Lagrangians and Hamiltonians, Cambridge University Press (2014)

[9] Orefice, A., Giovanelli, R., Ditto, D.: Complete Hamiltonian Description of Wave-Like Features in Classical and Quantum Physics. Foundations of Physics **39** (3), 256-272 (2009)

[10] K. Yee: Numerical solution of initial boundary value problems involving Maxwell's equations in isotropic media. IEEE Transactions on Antennas and Propagation **14** (3): 302-307 (1966)

[11] A. Taflove: Application of the finite-difference time-domain method to sinusoidal steady state electromagnetic penetration problem". IEEE Transactions on Electromagnetic Compatibility **22** (3): 191-202 (1980)

[12] Metzger, J.J., Fleischmann, R., Geisel, T.: Universal statistics of branched flow. Phys. Rev. Lett. **105**, 020601 (2010)

[13] Metzger, J. J.: Branched Flow and Caustics in Two-Dimensional Random Potentials and Magnetic Fields. Doctoral Thesis, Persistent Address: `http://hdl.handle.net/11858/00-1735-0000-0006-B4D6-8` (2010)

[14] Topinka, M.A., LeRoy, B.J., Westervelt, R.M., Shaw, S.E.J., Fleischmann, R., Heller, E.J., Maranowskik, K.D., Gossardk, A.C.: Coherent branched flow in a two-dimensional electron gas. Nature (London) **410**, 183 (2001)

[15] Ying, L.H., Zhuang, Z., Heller, E.J., Kaplan, L.: Linear and nonlinear rogue wave statistics in the presence of random currents. Nonlinearity **24**, R67-R87 (2011)

[16] Schwartz, T., Bartal, G., Fishman, S., Segev, M.: Transport and Anderson localization in disordered two-dimensional photonic lattices. Nat.Lett. **446**, 52-55 (2007)

[17] Segev, M., Silberberg, Y., Christodoulides, D.N.: Anderson localization of light. Nature Photonics **7**, 197-204 (2013)

[18] Perakis F., Mattheakis M., Tsironis G. P.: Small-world networks of optical fiber lattices. J. Opt. **16**, 102003 (2014)

[19] Blanc-Benon, Ph., Juve, D., Comte-Bellot, G.: Occurrence of Caustics for High-Frequency Acoustic Waves Propagating Through Turbulent Fields. Theoret. Comput. Fluid Dynamics **2**, 271-278 (1991)

[20] Wolfson, M. Tappert, F.: Study of horizontal multipaths and ray chaos due to ocean mesoscale structure. J. Acoust. Soc. Am. **107**, 154 (2000)

[21] Wolfson, M., Tomsovic, S.: On the stability of long-range sound propagation through a structured ocean. J. Acoust. Soc. Am. **109**, 2693 (2001)

[22] Barkhofen, S., Metzger, J.J., Fleischmann, R., Kuhl, U., Stockmann, H.J.: Experimental Observation of a Fundamental Length Scale of Waves in Random Media. Phys.Rev.Lett. **111**, 183902 (2013)

[23] Hohmann, R., Kuhl, U., Stockmann, H.J., Kaplan, L., Heller, E.J.: Freak waves in linear regime: A microwave study. Phys. Rev. Lett. **104**, 093901 (2010)

[24] Montina, A., Bortolozzo, U., Residori, S., Arecchi, F. T.: Non-Gaussian Statistics and Extreme Waves in a Nonlinear Optical Cavity. Phys. Rev. Lett. **103**, 173901 (2009)

[25] Klyatskin, V.I.: Caustics in random media. Waves in Random Media **3**, 93-100 (1993)

[26] V.I. Klyatskin: Stochastic equations through the eye of the physicist, ELSEVIER (2005)

[27] Mattheakis, M., Pitsios, I.J., Tsironis, G.P., Tzortzakis, S.: Linear and nonlinear photonic rogue waves in complex transparent media. (working paper)

[28] Ni, X., Wang, W.X., Lai, Y.C.: Origin of branched wave structures in optical media and long-tail algebraic intensity distribution. EPL (Europhysics Letters), **96** (4), 44002 (2011)

[29] Solli, D.R., Ropers, C., Koonath, P., Jalali, B.: Optical rogue waves. Nature (London) **450**, 1054-1057 (2007)

[30] Kaplan, L.: Statistics of Branched Flow in a Weak Correlated Random Potential. Phys. Rev. Lett. **89**, 18 (2002)

[31] Ockendon, H., Ockendon, J. R.: Waves and Compressible Flow, Springer Publication (2004)

[32] Gardiner, C.W.: Handbook of stochastic methods for physics, chemistry and the natural sciences. 2nd edn. Springer Publication (1985)

[33] Risken, H.: The Fokker Plank equation: Methods of solution and applications. 2nd edn. Springer Publication (1989)

[34] Polyanin, A.D., Zaitsev, V.: Handbook of exact solutions for ordinary differential equations. CRC Press (2002)

[35] Andrews, L.C., Phillips, R.L., Hopen, C.Y., Al-Habash, M.A.: Theory of optical scintillation, JOSA A **16**, 1417-1429 (1999)

[36] Heller, E.J., Kaplan, L., Dahlen, A.: Refraction of a Gaussian seeway. J. Geophysics **113**, C09023 (2008)

[37] Akhmediev, N., Dudley, J.M., Solli, D.R., Turitsyn, S.K.: Recent progress in investigation optical rogue waves. J. Opt. **15**, 060201 (2013)

[38] Bacha, M., Boukhalfa, S., Tribeche, M.: Ion-acoustic rogue waves in a plasma with a q-nonextensive electron velocity distribution. Astrophysics & Space Science **341**, 2 pp 591-595 (2012)

[39] Wang, Y.Y., Lib, J.T., Daia, C.Q., Chenc, X.F., Zhangd, J.F: Solitary waves and rogue waves in a plasma with nonthermal electrons featuring Tsallis distribution. Phys. Lett. A **377**, 34-35 pp. 2097-2104 (2013)

[40] Yan, Z.: Financial rogue waves. Commum. Theor. Phys. **54**, 947-949 (2010)

[41] Maluckov, A., Hadžievski, Lj., Lazarides, N., Tsironis, G.P: Extreme events in discrete nonlinear lattices. Phys. Rev E **79**, 025601 (2009)

[42] Maluckov, A., Hadžievski, Lj., Lazarides, N., Tsironis, G.P: Extreme events in two-dimensional disordered nonlinear lattices. Phys. Rev. D **252**, pp 59-64 (2013)

[43] Ehrt D., Kittel T., Will M., Nolte S., Tünnermann A., : Femtosecond-laser-writing in various glasses. Journal of Non-Crystalline Solids **345-346**, 332-337 (2004)

[44] Liu W., Petit S., Becker A., Aközbek N., Bowden C.M., Chin S.L.: Intensity clamping of a femtosecond laser pulse in condensed matter. Opt. Commun. **202**, 189-197 (2002)

[45] Birkholz S. Nibbering E.T.J.: Spatiotemporal Rogue Events in Optical Multiple Filamentation. Phys. Rev. Lett. **111**, 243903 (2013)

[46] Strogatz S.H.: Exploring complex networks. *Nature* **410** 268-276 (2001)

[47] Vendruscolo M., Dokholyan N.V., Paci E., Karplus M.: Small-world view of the amino acids that play a key role in protein folding. *Phys. Rev. E* **65** 061910 (2002)

[48] Newman M.E.J: The Structure and Function of Complex Networks, *SIAM Review* **45** (2003)

[49] Francesco R., Amedeo C.: The Protein Folding Network, *Journal of Molecular Biology* **342** 299-306 (2004)

[50] Pomerance A., Ott E., Girvan M., Losert W.: The effect of network topology on the stability of discrete state models of genetic control *W. PNAS* **106** 8209-8214 (2009)

[51] Kempes C.P., West G.B., Crowell K., Girvan M.: Predicting Maximum Tree Heights and Other Traits from Allometric Scaling and Resource Limitations, *PLOS ONE* **6** e20551 (2011)

[52] Watts D.J., Strogatz S.H.: Collective dynamics of 'small-world' networks, *Nature* **393** 440-442 (1998)

[53] Liu Y.Y, Slotine J.J., Barabasi A.L.: Controllability of complex networks, *Nature* **473** 167-173 (2011)

[54] Halu A., Garnerone S., Vezzani A., Bianconi G.: Phase transition of light in complex networks, *Phys. Rev. E* **87**, 022104 (2013)

[55] Halu A., Ferretti L., Vezzani A., Bianconi G.: Phase diagram of the Bose-Hubbard model on complex networks, *Europhysics Letters* **99**, 18001 (2012)

[56] Bianconi G.:, Superconductor-insulator transition in annealed complex networks, *Phys. Rev. E* **85**, 061113 (2012)

[57] Lahini Y., Pugatch R., Pozzi F., Sorel M., Morandotti R., Davidson N., Silberberg Y.: Observation of a Localization Transition in Quasiperiodic Photonic Lattices, *Phys. Rev. Lett.* **103** 013901 (2009)

[58] Naether U., Rojas-Rojas S., Martinez A.J., Stützer S., Tünnermann A., Nolte S., Molina M.I., Vicencio R.A., Szameit A.: Enhanced distribution of a wave-packet in lattices with disorder and nonlinearity, *Opt. Express* **21** 927-934 (2013)

[59] Vardeny Z.V., Nahata A., Agrawal A.: Optics of photonic quasicrystals, *Nat Photon* **7** 177-187 (2013)

[60] Hennig D., Tsironis G.P.: Wave transmission in nonlinear lattices, *Physics Reports* **307** 333-432 (1999)

[61] Li S., Manmana S.R., Rey A.M., Hipolito R., Reinhard A., Riou J.F., Zundel L.A., Weiss D.S.: Self-trapping dynamics in a two-dimensional optical lattice, *Phys. Rev. A* **88** 023419 (2013)

[62] Picozzi A.: Solitons, Self-trapping of speckled light beams, *Nat. Phot.* **2** 334-335 (2008)

[63] Gao H., Tian L., Zhang B., Barbastathis G.: Iterative nonlinear beam propagation using Hamiltonian ray tracing and Wigner distribution function, *Opt. Lett.* **35** 4148-4150 (2010)

[64] Molina M., Tsironis G.P.: Dynamics of self-trapping in the discrete nonlinear Schrödinger equation, *Physica D: Nonlinear Phenomena* **65** 267-273 (1993)

[65] Molina M., Tsironis G.P.: Applications of self-trapping in optically coupled devices *Physica D: Nonlinear Phenomena* **68** 135-137 (1993)

[66] Molina M.I., Tsironis G.P., Disorder in the discrete nonlinear Schrödinger equation, *International Journal of Modern Physics B* **9** 1899-1932 (1995)

[67] Perakis F., Tsironis G.P.: Discrete nonlinear Schrödinger equation dynamics in complex networks, *Phys. Lett. A* **375** 676-679 (2011)

[68] Tsironis G.P.: Exact dynamics for fully connected nonlinear networks, *Phys. Lett. A* **375** 1304-1308 (2011)

[69] Ni X., Wang W., Lai Y.: *Europhys. Lett.* **96** 44002 (2011)

[70] Marte M.A.M., Stenholm S.: Paraxial light and atom optics: The optical Schrödinger equation and beyond, *Phys. Rev. A* **56** 2940-2953 (1997)

[71] Barrat A., Barthelemy M., Pastor-Satorras R., Vespignani A.: The Architecture of Complex Weighted Networks, *PNAS* **101** 3747-3752 (2004)

[72] Callaway D.S., Newman M.E.J., Strogatz S.H., Watts D.J.: Network Robustness and Fragility: Percolation on Random Graphs, *Phys. Rev. Lett.* **85** 5468 (2000)

[73] Zhao J.H., Zhou H.J., Liu Y.Y.: Inducing effect on the percolation transition in complex networks *Nat. Commun.* **4** 2412 (2013)

[74] Eilbeck J.C., Lomdahl P.S., Scott A.C.: The discrete self-trapping equation, *Physica D: Nonlinear Phenomena* **16** 318-338 (1985)

[75] Maier S.A: Plasmonics, fundamentals and applications. Springer Science + Business Media LCC, New York (2007)

[76] Economou E.N.: Surface plasmons in thin films, Phys.Rev. **182** No.2 (1969)

[77] Novotny L.: Unedited chapters from the textbook Novotny L. and Hecht B., Principles of Nano-Optics. Cambridge University Press, Cambridge, (2006)

[78] Orfanidis S.J.: Electromagnetic Waves and Antennas. (online book), `http://www.ece.rutgers.edu/~orfanidi/ewa/`

[79] Homola, J. (Volume Editor): Surface Plasmon Resonance Based Sensors. Berlin: Springer Verlag (2006)

[80] Athanasopoulos C., Mattheakis M., Tsironis G.P.: Enhanced surface plasmon polariton propagation induced by active dielectrics. Excerpt from the proceedings of the 2014 COMSOL Conference in Cambridge (2014)

[81] Yushanov S.P., Gritter L.T., Crompton J.S., Koppenhoefer K.C.: Surface Plasmon Resonance, Excerpt from the proceedings of the 2012 COMSOL Conference in Boston (2012)

[82] Noginov M.A., Podolskiy V.A., Zhu G., Mayy M., Bahoura M., Adegoke J.A., Ritzo B.A., Reynolds K.: Compensation of loss by optical gain in propagating surface plasmons. SPIE Proceedings vol.**6642**, edited by S. Kawata, Vladimir M. Shalaev, Din-Ping Tsai, SPIE digital library, San Diego, CA, USA (2007)

[83] Noginov M.A., Zhu G., Mayy M., Ritzo B.A., Noginova N., Podolskiy V.A.: Stimulated emission of surface plasmon polaritons. Phys. Rev. Lett. **101**, 22, 226806, (2008)

[84] Suarez I., Rodriguez-Canto P., Abargues R., Martinez-Pastor J., Fitrakis E.P., Tomkos I.: Surface plasmon-polariton amplifiers. Presented at ICTON 2012, Warwick, UK (invited) (2012)

[85] Fitrakis E.P., Kamalakis T., Sphicopoulos T.: Slow light in insulator-metal-insulator plasmonic waveguides. josa B, **30**, 2159-2164 (2011)

[86] Avrutsky I.: Surface plasmons at nanoscale relief gratings between a metal and a dielectric medium with optical gain. prb **70**, 155416 (2004)

[87] Berini P., De Leon I.: Surface plasmon-polariton amplifiers and lasers. Nature Photonics, **6**, (2012)

[88] Nezhad M.P., Tetz K., Fainman Y.: Gain assisted propagation of surface plasmon polaritons on planar metallic waveguides. Optics Express, **12** (17) , (2004)

[89] De Leon I., Berini P.: Amplification of long-range surface plasmons by a dipolar gain medium. Nature Photonics **28**, (2010)

[90] Yu Z., Veronis G., Brongersma M.L., Fan S." Gain-induced switching in metal-dielectric-metal plasmonic waveguides. SPIE Proceedings **6896**, C.M. Greiner and C.A. Waechter (ed), SPIE digital library, San Jose, CA, USA (2008)

[91] Huidobro P.A., Nesterov M.L., Martin-Moreno L., Garcia-Vidal F.J.: Transformation optics for plasmonics, Nano Lett. **10**. 1985-1990 (2010)

[92] Liu Y., Zentgraf T., Bartal G. and Zhang X.: Transformation plasmon optics. Nano Lett. **10** 1991-7 (2010)

[93] Zentgraf T., Liu Y, Mikkelsen M. H, Valentine J., Zhang X.: Plasmonic Luneburg and eaton lenses. Nature Nanotechnol. **6** 151-5 (2011)


European Union
European Social Fund

Co- financed by Greece and the European Union